Preparation of photothermal nanomaterials for water treatment

Go Inoue

THÈSE DE DOCTORAT

Présentée à l'Université de Lille

Ecole Doctorale Sciences de l'Ingénierie et des Systèmes

par Go INOUE

Preparation of photothermal nanomaterials for water treatment

Préparation de nanomatériaux photothermiques pour la purification d'eau

Soutenue le 6 janvier 2023 devant le jury composé de

Prof. Yamin LEPRINCE-WANG	Rapportrice	Université Gustave Eiffel
Prof. Souad AMMAR	Rapportrice	Université Paris Cité
Prof. Henri HAPPY	Examinateur (Président du jury)	Université de Lille
Prof. Sorin MELINTE	Examinateur	Université catholique de Louvain
Dr. Rabah BOUKHERROUB	Directeur de thèse	IEMN, CNRS
Prof. Sabine SZUNERITS	Co-directrice de thèse	Université de Lille

Abstract

For our daily lives, freshwater is a vital resource. However, due to demographic changes, unequal access to water sources, climate change, and lack of infrastructure, safe drinking water is far from being accessible to all. Therefore, water represents one of the strategic issues of the 21st century.

Existing technologies, such as reverse osmosis and multi-stage flash distillation, are not so expensive techniques, but they require intensive maintenance, large amounts of energy input, and large-scale production plants, which are negative factors for economically-less developed regions.

Solar-driven interfacial evaporation is one of the most studied technologies in recent years, as it has the potential to solve the shortage and accessibility to clean water in an environmentally sustainable way. This technology uses sunlight to evaporate contaminated water using a photothermal evaporator. A lot of research has been done so far to find efficient photothermal materials and optimal structures for evaporators. However, there are still many obstacles to the widespread use of this technology. First of all, the raw materials for the preparation of the evaporator must be very accessible and inexpensive. In addition, the preparation should not consume much energy and should not be complex.

In this research, three evaporators were prepared by using highly-accessible raw materials and easy synthesis processes and their vapour generation, desalination and bacterial eradication capacities were assessed. After a general introduction (chapter 1) and materials and methods (chapter 2), the 3rd and 4th chapters were dedicated to the preparation, characterization and interfacial water evaporation assessment of green moss-poly(*N*-phenylglycine) and green moss-petroleum coke, respectively. Green moss (GM) is a very accessible biomass that exists almost everywhere. Poly(*N*-phenylglycine), PNPG, is a polymer with a similar structure to polyaniline with good photothermal properties, and it is applied for photothermal eradication of tumours and bacteria. On the other hand, petroleum coke (PetCoke) is a by-product of oil refining, and often stored in large quantities as a waste product. Due to the similarity of its structure to graphitic-based materials, it exhibited good photothermal behavior.

In the 5th chapter, a hybrid evaporator consisting of cigarette filter and PetCoke wastes was prepared. A comparison between a flat 2D and a 3D evaporator with a surface composed of orderly patterned protrusions of 2.1 cm was carried out to assess the influence of the evaporator configuration on the evaporation performance.

All the prepared evaporators featured enhanced evaporation rates and were successfully applied for producing safe drinking water from real seawater and water contaminated with bacteria (*E. coli*).

Résumé

Pour notre vie quotidienne, l'eau douce est une ressource vitale. Cependant, en raison des changements démographiques, de l'inégalité d'accès aux sources d'eau, du changement climatique et du manque d'infrastructures, l'eau potable est loin d'être accessible à tous. L'eau représente donc l'un des enjeux stratégiques du XXI^{ème} siècle.

Les technologies existantes, telles que l'osmose inverse et la distillation flash à plusieurs étages, ne sont pas des techniques très coûteuses, mais elles nécessitent une maintenance intensive, un apport énergétique important et des moyens de production assez élevés, ce qui constitue un frein pour leur utilisation dans des régions économiquement peu développées.

L'évaporation interfaciale solaire est l'une des technologies les plus étudiées ces dernières années, car elle a le potentiel de résoudre le problème de la pénurie et de l'accessibilité de l'eau propre d'une manière écologiquement durable. Cette technologie exploite la lumière solaire pour évaporer l'eau contaminée à l'aide d'un évaporateur photothermique. De nombreuses recherches ont été menées jusqu'à présent pour trouver des matériaux photothermiques efficaces et des structures optimales pour les évaporateurs. Cependant, il existe encore de nombreux obstacles quant à l'utilisation généralisée de cette technologie. Tout d'abord, les matières premières pour la préparation de l'évaporateur doivent être très accessibles et peu coûteuses. De plus, la préparation doit être simple et ne doit pas consommer beaucoup d'énergie.

Dans ce travail de thèse, trois évaporateurs ont été préparés en utilisant des matières premières très accessibles et des procédés de synthèse faciles ; leurs capacités de production de vapeur, de dessalement et d'éradication bactérienne ont été évaluées. Le manuscrit comprend cinq chapitres. Après une introduction générale (chapitre 1) et les matériaux et méthodes (chapitre 2), les chapitres 3 et 4 ont été consacrés à la préparation, la caractérisation et l'évaluation des propriétés d'évaporation interfaciale de la mousse verte-poly(N-phénylglycine) et de la mousse verte-coke de pétrole, respectivement. La mousse verte (MG) est une biomasse très accessible qui existe presque partout à travers le globe. La poly(N-phénylglycine), PNPG, est un polymère dont la structure est similaire à celle de la polyaniline et qui possède de bonnes propriétés photothermiques. Il est utilisé pour l'éradication photothermique des tumeurs et des bactéries. D'autre part, le coke de pétrole (PetCoke) est un sous-produit du raffinage du pétrole, souvent stocké en grandes quantités comme déchet. En raison de la similarité de sa structure avec les matériaux à base de graphite, il présente un bon comportement photothermique.

Dans le chapitre 5, un évaporateur hybride composé de filtres de cigarettes et de déchets de PetCoke a été préparé. Une comparaison entre un évaporateur plan 2D et un évaporateur 3D avec une surface composée de protubérances à motifs ordonnés de 2,1 cm a été réalisée pour évaluer l'influence de la configuration de l'évaporateur sur les performances d'évaporation.

Tous les évaporateurs préparés présentaient des taux d'évaporation élevés et ont été utilisés avec succès pour produire de l'eau potable à partir d'eau de mer et d'eau contaminée par des bactéries (*E. coli*).

Table of contents

Chapter 1: General introduction

1.1. The water problem is a major issue of our century

The water problem is a major challenge of our century. 96.5% (1.34×10^9 km^3) of the existing water on the planet (1.39×10^9 km^3) is in the form of sea water. Even among freshwater, 68.7% of the freshwater exists as ice that persists at the poles and on mountainous regions [1]. This means that the freshwater resource available to us is very scarce.

On the other hand, human activity is constantly increasing. The world population was 2.5 billion in 1950, 7.7 billion in 2019, and this number will reach 9.7 billion in 2050 [2]. A larger population requires a greater demand for food, because food supply inevitably requires water. As a result, water withdrawal increased three-fold between 1950 and 2010 [3].

There is a considerable difference in the magnitude of the water problem depending on the geographical and demographic situation. For example, in high-latitude countries with stagnating populations, water stress has not changed much in recent years (**Figure 1.1a**). On the other hand, in some countries with a desert climate, the situation is rapidly worsening due to rapid population growth (**Figure 1.1b**).

Most of the countries that suffer from severe water stress are located at low latitude, such as North Africa, Middle East, South Asia, Central Asia, Iberian Peninsula and Mexico. In addition to these countries, some highly populated regions such as North-East China and South Korea also experience significant water stress [4] [5].

In economically less developed countries, the agricultural sector requires the overwhelming majority of freshwater consumption (**Figure 1.1c,d**). This fact implies two things: first, demographic change will accelerate water stress as demand for freshwater in the agricultural sector will inevitably increase. Secondly, these countries are at high risk of famine due to climate change.

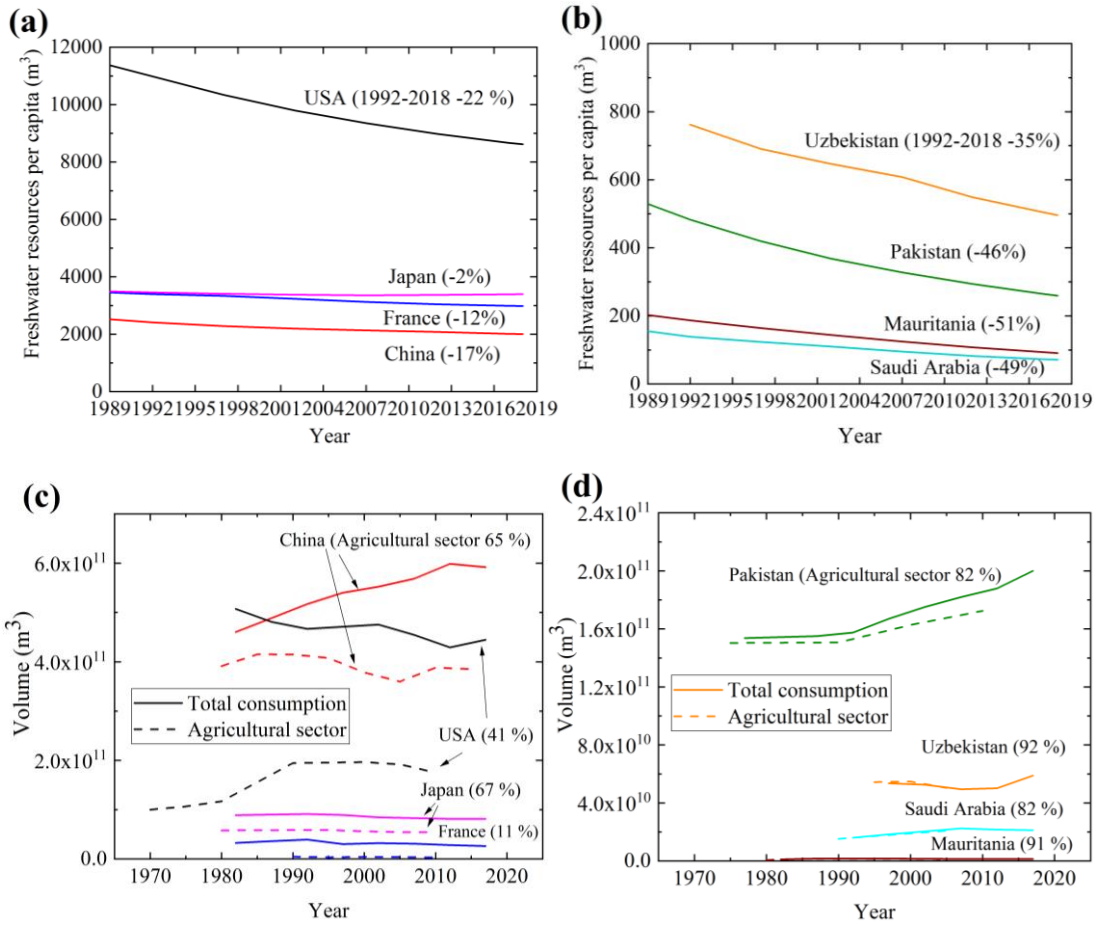

Figure 1.1. Available freshwater resources per capita in several countries (**a, b**). Total annual freshwater consumption and proportion in the agricultural sector (in parentheses) (**c, d**) [6].

In addition to demographic change, climate change is amplifying water stress. The effect of global warming on precipitation change is not so simple to predict and generalise, but it is possible that the trend of precipitation change will be increasingly extreme and the rapid melting of mountain glaciers will cause water deficit (**Figure 1.2**) [7] [8], and some regions may be at greater risk from climate change.

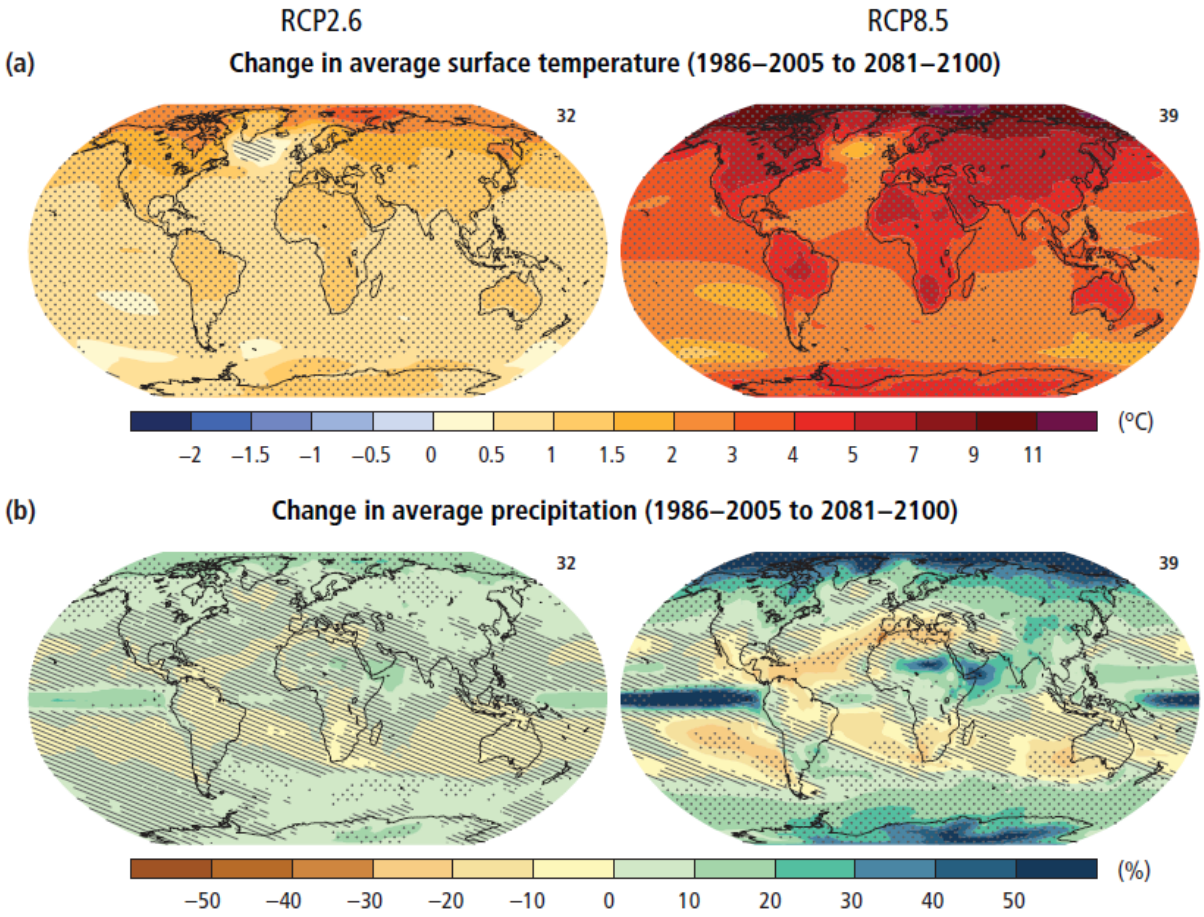

Figure SPM.7 | Change in average surface temperature **(a)** and change in average precipitation **(b)** based on multi-model mean projections for 2081–2100 relative to 1986–2005 under the RCP2.6 (left) and RCP8.5 (right) scenarios. The number of models used to calculate the multi-model mean is indicated in the upper right corner of each panel. Stippling (i.e., dots) shows regions where the projected change is large compared to natural internal variability and where at least 90% of models agree on the sign of change. Hatching (i.e., diagonal lines) shows regions where the projected change is less than one standard deviation of the natural internal variability. *{2.2, Figure 2.2}*

Figure 1.2. Impact of climate change on temperature and precipitation under different scenarios [7].

In addition, pollution is also a serious problem. Due to the lack of industrial, agricultural, and domestic wastewater treatment facilities, a large population in some regions faces pollution from organic molecules (dyes, pesticides, antibiotics…), heavy metals [9], and bacteria, notably *Escherichia coli (E. coli*) [10].

Water stress is not a problem of the future; it is a present threat of our era. Water is an undeniably essential resource for human life. Water-rich territories are therefore considered interesting from the point of view of geopolitical strategy, and this can be a great risk causing conflict between different groups and undermining the stability of a region. For example, in Central Asia, after the break-up of the USSR in 1991, the issue of water distribution still exists

as an explosive diplomatic problem between water-rich upstream countries (Kyrgyzstan and Tajikistan) and water-poor downstream countries with large populations (notably Uzbekistan) [11].

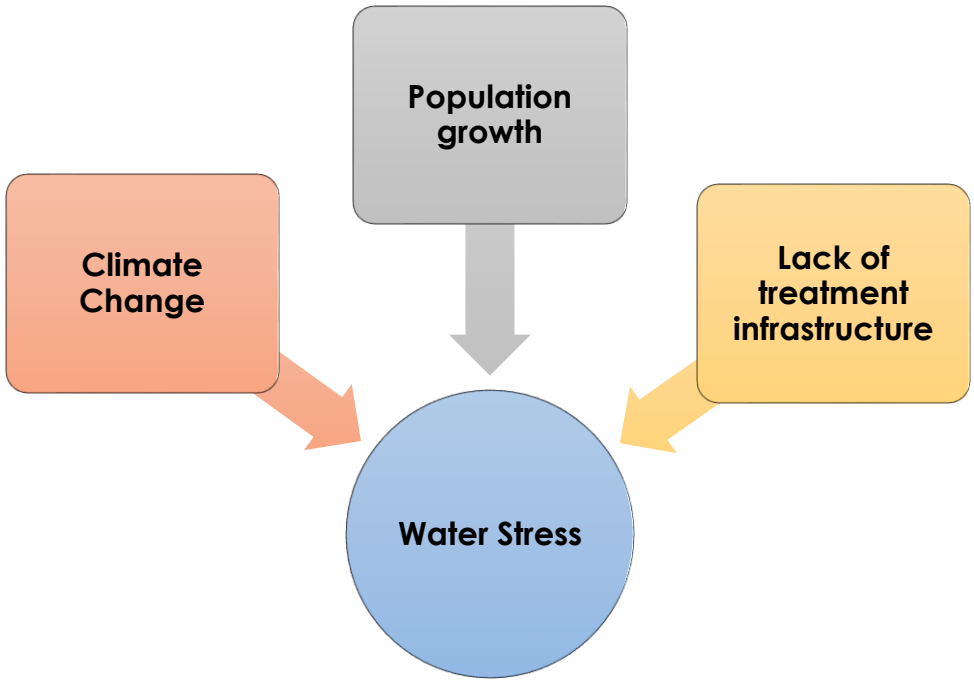

Figure 1.3. Water stress factors.

1.2. Conventional techniques for seawater desalination

As mentioned above, seawater represents a high proportion of the water on Earth. For human life, however, water containing much less salt is needed.

Salinity refers to the concentration of dissolved salt (NaCl, $MgCl_2$, $MgSO_4$, etc.) in water. The salinity of seawater is 35 g kg^{-1} compared to less than 1 g kg^{-1} in fresh water.

Direct consumption of seawater would cause dehydration of the human body. Irrigation with seawater will surely damage the land and plants. For these reasons, freshwater is a resource we need. It is therefore a reasonable strategy to transform seawater into freshwater in order to reconcile the high demand for freshwater and the accessibility and the abundance of seawater.

In this context, some techniques for desalination have been developed. Reverse osmosis is one of the best known means of desalination. This technique consists of applying pressure on the salt water in contact with a semi-permeable membrane to reject the salt and retrieve the fresh water after passing through the membrane. This membrane does not allow the elements dissolved in the liquid to pass through beyond the membrane (**Figure 1.4**).

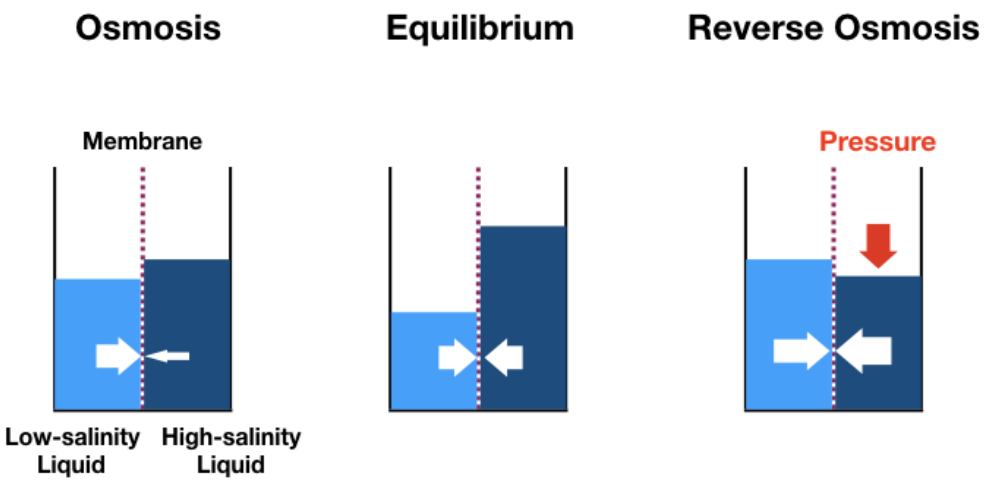

Figure 1.4. Reverse osmosis mechanism.

In the 1950s, as California faced water stress, seawater conversion was a priority topic. In 1949, Hassler at UCLA in California published a report "The sea as a source of fresh water" on steam transfer through cellophane sheets [12]. In 1954, a prototype of reverse osmosis equipment for seawater desalination was materialised in their laboratory [13]. Then, the Loeb-Sourirajan membrane, which achieved an interesting efficiency was developed in 1960, and around 1961, a patent was filed for this membrane [14].

Nowadays, reverse osmosis accounts for 69% of the world's desalination, and this means that this technology is the most widespread among desalination technologies due to its economic efficiency [15]. However, the major problems are membrane biofouling and filter clogging of the system due to microscopic algae growth [16]. This is unfavourable for safe water production and stable plant operation.

Multi-stage flash distillation (MSF) is the second most used technique (18%). This simpler process than reverse osmosis involves evaporating seawater and condensing the collected vapour with fresh water in several compartments (**Figure 1.5**). Each compartment contains a heat exchanger and a condensate collector, and the installation of several compartments of different temperatures helps to improve the yield of condensed water.

This technology is not demanding on the quality of the seawater, and the quality of the product by multi-stage flash distillation is excellent (with salinity normally less than 5 ppm). However, this method requires a lot of energy to adjust the temperatures. For this reason, especially the Gulf countries (Saudi Arabia, United Arab Emirates, Kuwait, and Qatar), benefiting from the abundance of cheap fossil fuels, are using this process to meet their growing water needs (**Figure 1.6**). This method is the least energy efficient (multi-stage flash distillation: 13.5-25.5 kWh m^{-3}, reverse osmosis: 3-3.5 kWh m^{-3} [17]).

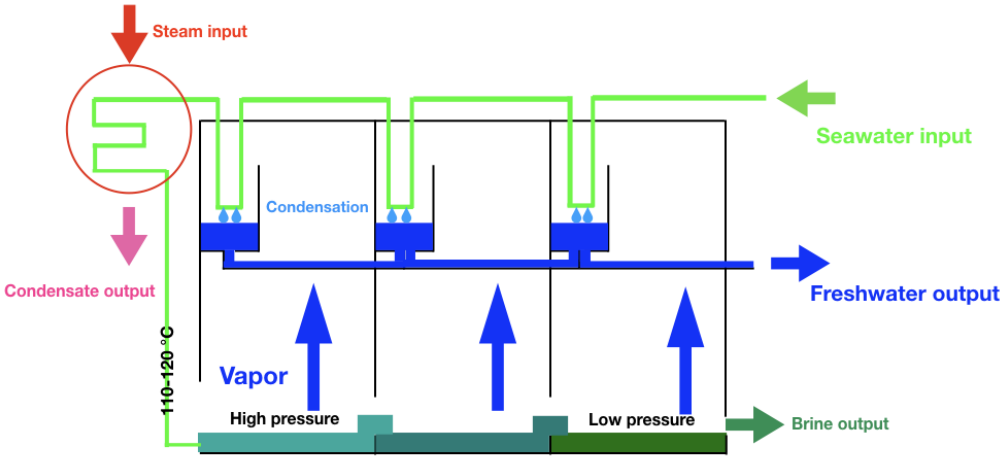

Figure 1.5. Multi-stage flash distillation mechanism

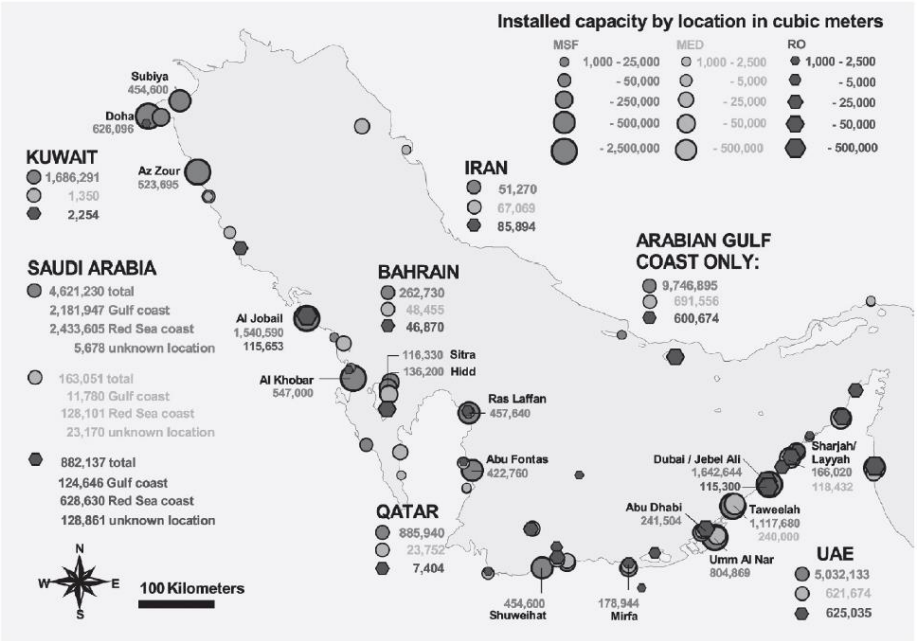

Figure 1.6. Desalination in the Gulf countries [18].

Despite the remarkable development on desalination technologies in the 20th century, the water problem is far from being solved; the above-mentioned processes require a large amount of energy, large plants, regular maintenance, etc. These requirements hinder the installation of desalination plants in economically-depressed regions with poor infrastructure. In order to solve the water stress in remote areas, an alternative process needs to be developed that is technically easier, independent of the socio-economic situation, and environmentally-friendly.

1.3. Solar energy

The sun is a star whose energy we benefit from every day. The sun emits 3.8×10^{23} kW, of which 1.8×10^{14} kW will be intercepted by the Earth. The Earth's surface receives 1.08×10^{14} kW after the radiation passes the atmosphere around the Earth. In other words, the sun sends us 7500 times more than the world's energy needs [19].

As already mentioned in sub-chapter 1.1., many of the regions suffering from severe water stress are located near the Tropic of Cancer. The idea of harnessing inexhaustible solar energy is totally reasonable if we want to find a solution to supply this population with fresh water in a sustainable way. Fortunately, a comparison of the two maps (**Figures 1.7** and **1.8**) shows that the regions under threat of freshwater supply have a lot of potential for solar energy exploitation.

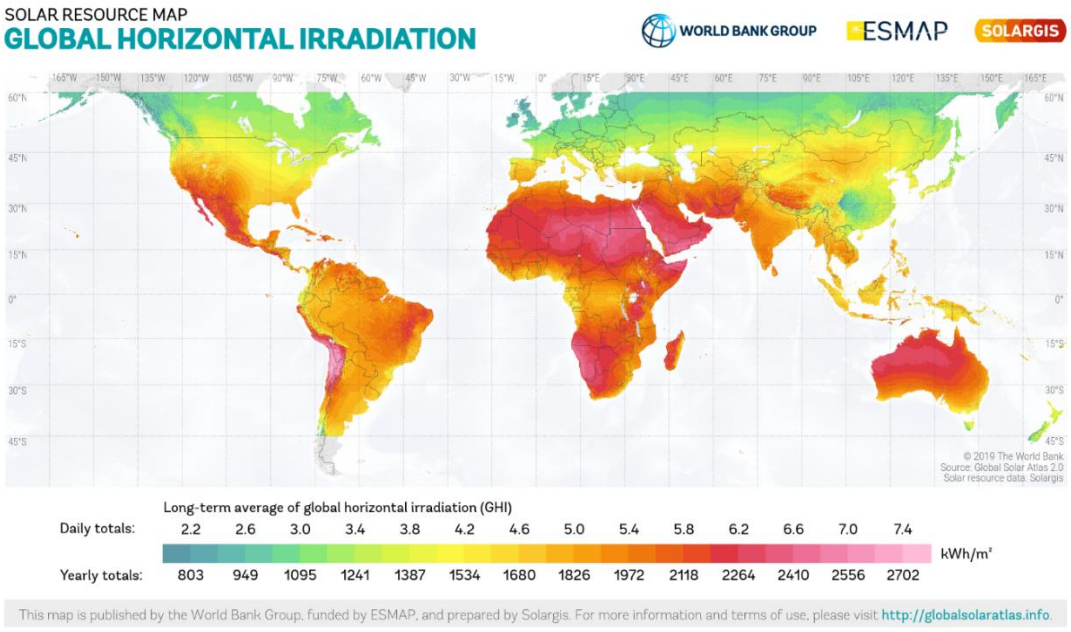

Figure 1.7. World map of sunlight irradiance per year [20].

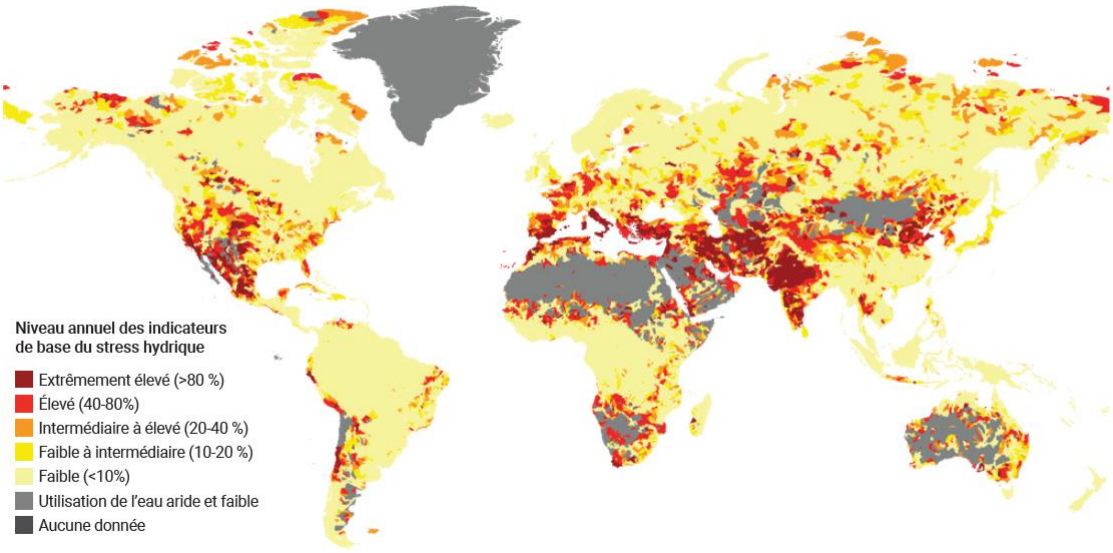

Figure 1.8. Global map of water stress levels [8].

The spectrum of sunlight we use is not identical to that emitted by the sun, because some of the irradiation is absorbed by the atmosphere (O_3, O_2, CO_2) and water (H_2O) (**Figure 1.9**). Of the total wavelength of AM 1.5, the ultraviolet part accounts for 5% of the total energy, the visible light (λ = 380-780 nm) is 43%, and the infrared (λ = 780-3000 nm) is 52%.

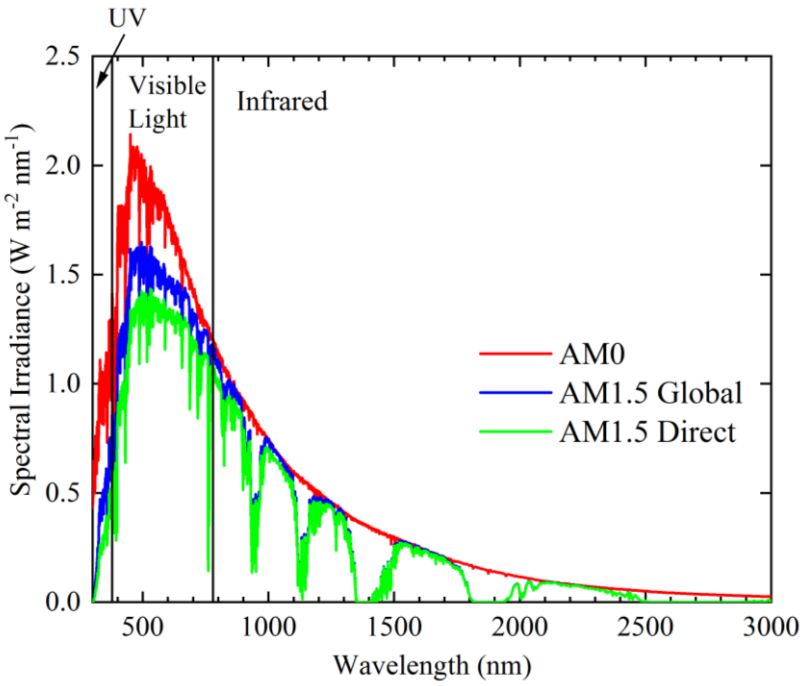

Figure 1.9. Comparison between AM0 and AM1.5 [21].

AM (Air Mass) 0 means an extra-terrestrial spectrum that does not undergo any absorption by the atmosphere. If the sun is at the zenith relative to the observer, the radiation undergoes the minimum of absorption by the atmosphere before reaching the observer. This point corresponds to the equator at the equinoxes. At the summer solstice, this corresponds to latitude 23.5°N, and at the winter solstice, on the other hand, to latitude 23.5°S. In this case, this observer will see the radiation from AM1. The observer who is 48.2° away from the zenith will observe radiation impacted by the atmosphere 1.5 times more than AM1, and this radiation can therefore be defined as AM1.5 (**Figure 1.10**). In this work, AM1.5 is used in accordance with other previous research reports.

AM0 is the extra-terrestrial spectrum, whose total energy amounts to 1353 W m^{-2}. After the "ideal" atmospheric absorption (except for scattering by the cloud, for example), the energy of AM1.5 decreases to 963.8 W m^{-2}. In the experimental field, however, 1 sun is frequently used as a unit of power of radiation to simplify the calculation, and this is equivalent to 1000 W m^{-2}.

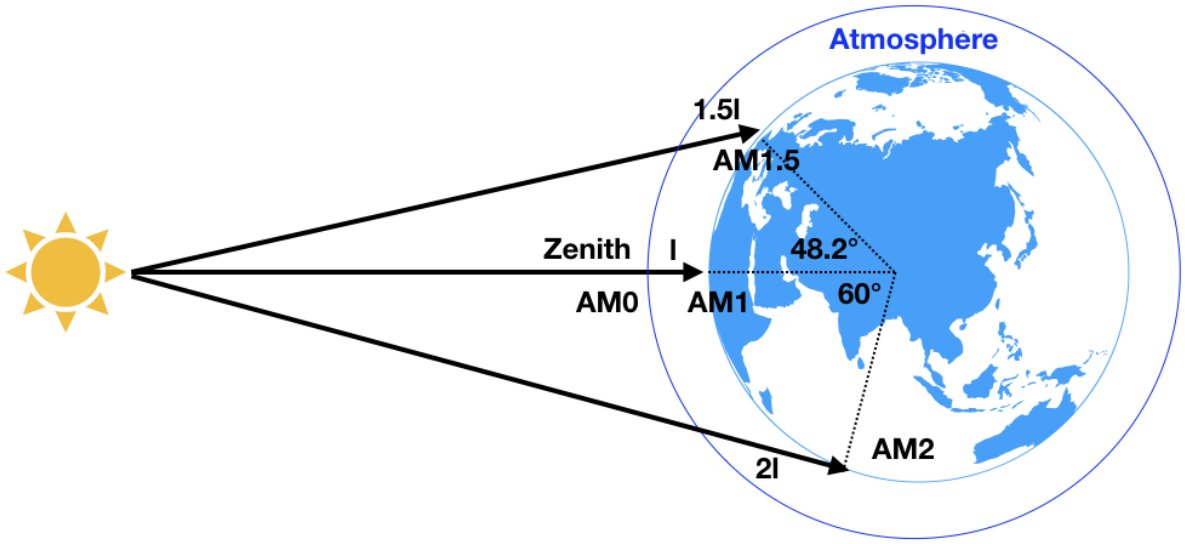

Figure 1.10. The notions of AM0, AM1, and AM1.5.

1.4. Appearance of solar interfacial evaporation

Solar-driven interfacial evaporation is a technique that is attracting increasing interest among researchers trying to find solutions to the water problems of our century. This technique involves the efficient evaporation of salty or contaminated water using photothermal materials.

Photothermal materials are, as the name suggests, materials that are able to convert incident light into heat. By harnessing this heat and water, these materials are able to generate water vapour as well. When this vapour is condensed by a suitable device, condensed water, normally freshwater, can be obtained.

Originally, photothermal materials were sought after especially in the biomedical field. Photothermal therapy is an alternative treatment to detect and ablate cancer cells using photothermal materials. For this technology, photothermal materials capable of converting infrared radiation (λ = 700-1100 nm) to heat is at the centre of interest. In this field, several researches existed even before the appearance of solar interfacial evaporation [22] [23]. However, solar interfacial evaporation has only been a research topic in the 2010s.

To the best of my knowledge, the study by Zeng in 2011 was the first report concerning the generation of vapour by solar interfacial evaporation. In this work, Fe_3O_4/C particles were incorporated into poly(furfuryl alcohol) (PFA). They had some success in increasing the evaporation rate by 2.3 times [24].

Then, Neumann *et al.* in 2012 showed that the conversion efficiency of carbon and gold nanoparticles dispersed in water was roughly 24% [25]. At that stage, the conversion efficiency was not very high due to the loss of heat to the bulk water. At that time, despite the report by Zeng in 2011, interfacial evaporation as a means of minimising heat loss was not a sufficiently widespread idea.

In 2014, Deng's team reported on a plasmonic film, loaded by gold nanoparticles [26]. They succeeded in confining the heat generated to the film, as a result, less heat escaped to the bulk water and most of the heat was efficiently used for water evaporation. In 2015, they improved the evaporator by introducing a paper support between the gold film and bulk water, and the conversion efficiency reached 77.8% with this device [27].

Since this success, the focus of photothermal evaporation has shifted to solar interfacial evaporation.

1.5. Photothermal mechanism

Photothermal materials are, as one might guess, materials that are able to convert incident radiation (incident photons) to heat within the materials. There are three mechanisms for this

conversion; (I) Plasmonic nanoparticles, (II) Generation of electron-hole pairs and relaxation, and (III) HOMO-LUMO excitation and relaxation.

1.5.1. Plasmonic nanoparticles

Plasmonic metals (typically noble metals such as Au, Ag) exhibit Localised Surface Plasmon Resonance (LSPR). As an example, the presence of an absorption band is observed in the wavelength range of 500 to 550 nm for gold nanoparticles. This resonance occurs when the frequency of the incident photons is identical to that of the electrons on the surface of a metal. As a result, there will be a collective oscillation of free electrons on the particles. A plasmon is defined as a quantum of collective oscillation of free electrons in a metal.

Plasmons can relax either by radiative or non-radiative processes in a competitive manner. By radiative processes, they are converted to radiation of light. By non-radiative processes, the "hot" electrons (in this context, excited electrons whose life time is of the order of a few tens of femto-seconds) lose their energy during the collision with the atoms. In this phase, the kinetic energy of the electrons is transformed into heat, and thus this process increases the temperature of the sample.

Table 1.1 summarizes some pertinent examples of research using plasmonic metals. In addition to the evaporation rate and conversion efficiency, the structure of the evaporator is also provided in this table. The "support" means a material that serves to support the sample physically, and at the same time, isolate the sample thermally. The "water supply" means through which material the water can move from the bulk water to the interface. These elements are also important for the functioning of this method and will be discussed in subchapter 1.7.

Table 1.1. Examples of photothermal materials with plasmonic nanoparticles.

Material	Support (Thermal Insulation)/Water supply	Evaporation rate E_1 (kg m^{-2} h^{-1})	Conversion efficiency η (%)	Reference
Ag-PPy (Polypyrrole)	EPE (Polyethylene)/Material	1.55	92.6	28
Nanostructured Ag	Paper/Paper (porous)	1.38	95.2	29
Nanostructured Au	Al_2O_3/Al_2O_3 (porous)	≈ 5.5 (4 sun)	> 90 (4 sun)	30
Nanostructured Au	Aerogel/Aerogel (Polyvinyl alcohol, PVA)	2.7	79.3	31
Ag Nanoparticles-Diatomite (Porous and light rock)	Paper + Polystyrene foam/Diatomite	1.39	92.2	32
Pd-wood	Wood/Material	11.8	85 (10 sun)	33
Ag-PPy (Polypyrrole)	Polymer based on 1-vinyl-3-ethylimidazolium bromide and N,N′-Methylenebis(acrylamide)/Polymer	1.37	88.7	34

1.5.2. Generation of electron-hole pairs and relaxation

This mechanism can be observed normally in a semiconductor. A semiconductor is able to produce electron-hole pairs when it receives irradiation whose energy exceeds the gap between the two bands, the valence and the conduction bands.

There are two types of relaxation of excited electrons, radiative and non-radiative relaxation. In radiative relaxation, photons are released when electrons move from a higher energy state to a lower energy state (recombination). In contrast, non-radiative relaxation refers to a situation where phonons are produced in exchange for the decrease in energy of the electrons. The

increase in vibrational energy within the crystal lattice can be observed as an increase of temperature. **Table 1.2** summarizes some examples of photothermal materials based on semiconductors.

Table 1.2. Examples of photothermal materials based on semiconductor materials.

Material	Support (Thermal Insulation)/Water supply	Evaporation rate E_1 (kg m^{-2} h^{-1})	Conversion efficiency η (%)	Reference
Cotton-CuS-Agarose Aerogel	Insulating foam /Cotton rod	1.63	94.9	35
MoS_2 Aerogel (chitosan, glutenaldehyde)	-/Material	1.27	88.0	36
Hydroxyapatite nanowires-NiO -Paper	Polystyrene/Airlaid paper	1.38	83.5	37
Ti_2O_3 Nanoparticle	Cellulose/Cellulose	1.32	92.1	38
CuS-Carbon Nanotube Gauze	Polystyrene/Scotch paper	1.58	95.0	39
Ti^{3+}-TiO_2-Cellulose	Polyethylene/Cellulose	1.20	77.1	40
CuO-CN-Fibre membrane	Polyethylene/Material	1.14	72	41

1.5.3. HOMO-LUMO excitation and relaxation

Carbon-based materials and polymers also exhibit photothermal properties. π electrons, weakly bound to carbon atoms, can be easily excited to the π* orbital with relatively low energy. Typically, in π-π conjugated systems, or π-σ hyper-conjugated systems, the electrons are easily excited (π → π* (antibonding)), and as a result, strong absorption is observed in the near

infrared region. In this phenomenon, electrons move from the lower energy state (HOMO, Highest Occupied Molecular Orbital) to the higher energy state (LUMO, Lowest Unoccupied Molecular Orbital). During the relaxation of electrons, analogously to the case of semiconductors, the energy of the electrons is converted to heat by means of changing the vibration mode.

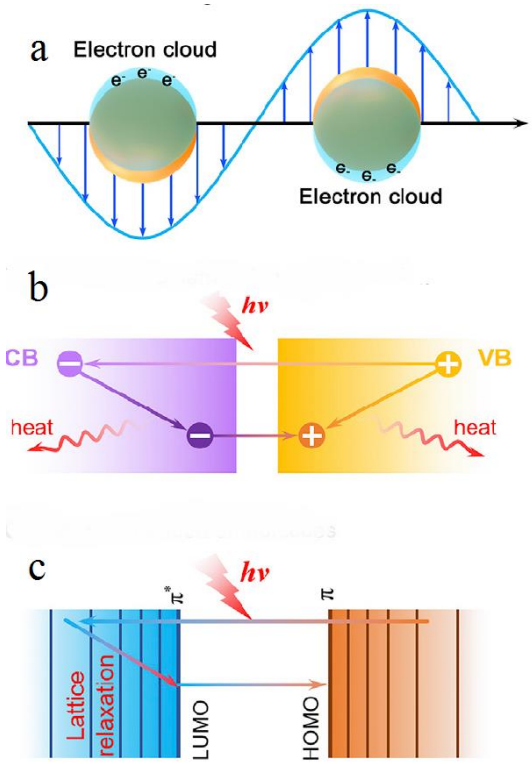

Figure 1.11. (**a**) LSPR, (**b**) Generation of electron-hole pairs in a semiconductor, (**c**) HOMO-LUMO excitation-relaxation [42].

Several types of polymers such as polypyrrole, polydopamine and polyaniline were investigated (**Table 1.3** and **Figure 1.12**). A conjugated system refers to a compound consisting of atoms linked by delocalised π-bonds. In these polymers, several conjugated bonds align, and, as a result, the difference between bonding and non-bonding orbitals becomes closer as a function of the length of the conjugated bonds. In general, the energy gap between the two orbitals is small when the conjugated bonds are long (**Figure 1.13**).

Absorption is synonymous of a transition of electrons between different molecular orbitals. If the energy gap between the two orbitals is small, even absorption of low-energy light occurs.

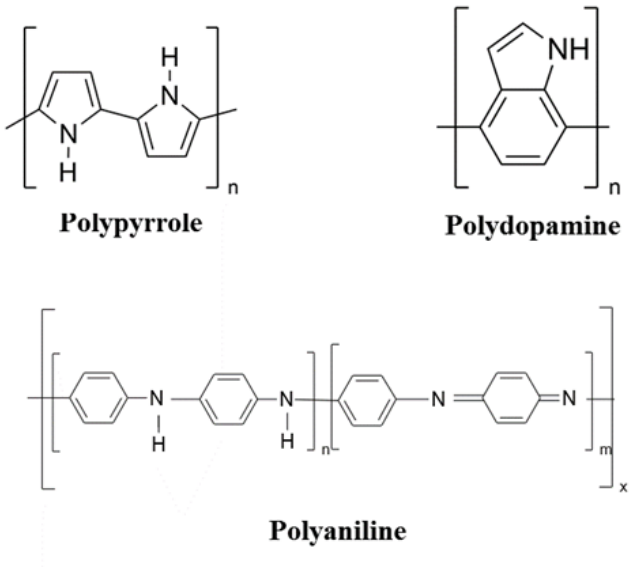

Figure 1.12. Polymers for photothermal conversion.

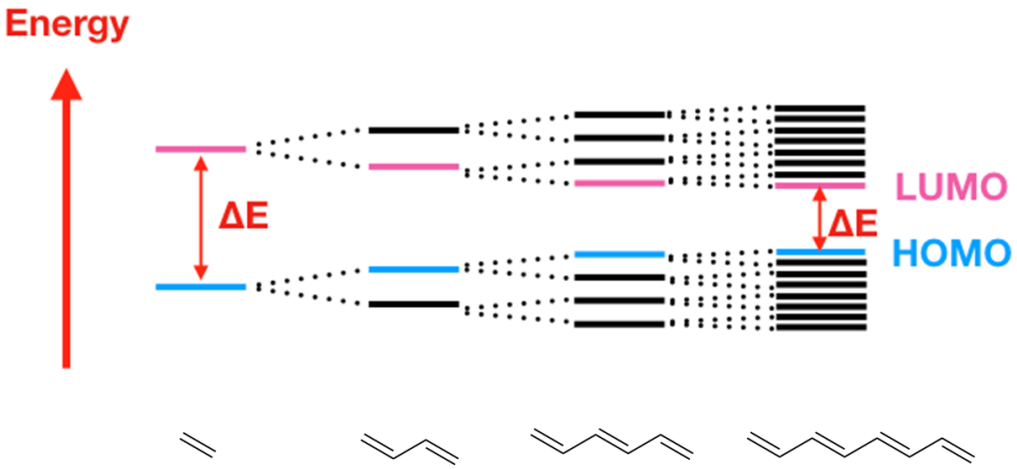

Figure 1.13. The energy gap between LUMO and HOMO.

Table 1.3. Examples of polymer-based photothermal materials. ((*): Biomass-based material for water supply)

Material	Support (Thermal insulation) / Water supply	Evaporation rate E_1 (kg m^{-2} h^{-1})	Conversion efficiency η (%)	Reference
Polyaniline-Nanocellulose-Polyvinyl Alcohol	Polystyrene/ Nanocellulose-Polyvinyl Alcohol	1.4	88	43
Polydopamine-Cellulose Aerogel	Rubber/Material	1.36	86	44
Sodium polystyrene sulfonate-Polyvinyl alcohol Hydrogel	Insulating foam/ Material	3.86	92.4	45
Polypyrrole-polydopamine-polyethyleneimine-Melamine foam	Polystyrene/Cotton and Paper	1.38	93.04	46
Polypyrrole-Corn straw	Insulating foam/Material	1.85	96.8	47 (*)
Polydopamine-Nickel foam	Polystyrene/Cotton	1.39	87.8	48
Polyester (Black)	-/Material	0.57	48.3	49

In addition to polymers, several carbon-based materials have been sought due to the abundance of raw materials, biodegradability and excellent light absorption in the near infrared (**Table 1.4**). For instance, the most studied material is reduced graphene oxide (rGO) with a complex

structure shown in **Figure 1.14**. There are highly developed intrinsic π-conjugations in this material, which confer strong near-infrared absorption to rGO.

In addition to industrially manufactured carbon materials, biomass materials are also being sought after in the field of photothermal evaporation. These materials exhibit several advantages. Firstly, in most cases, the raw materials are extremely accessible. This is an economically favourable factor. Secondly, the raw material only requires to be carbonised in order to be used as a photothermal material, and this makes it advantageous for industrial processes and reduce the cost of manufacture. After use, it is easy to discard the material as it is biodegradable.

As far as the biomass material is concerned, there are two types of evaporators. In the first case, the biomass material serves only as a passage for water. In this case, the absorption of light and the generation of heat and vapour take place in another material. This is marked by (*) in **Table 1.4**.

In the other case, the generation of heat and vapour occurs in carbonised biomass. This is marked as (**) in **Table 1.4**. In most of these cases, the structure of the device is extremely simple as the evaporator also serves as a water supply path.

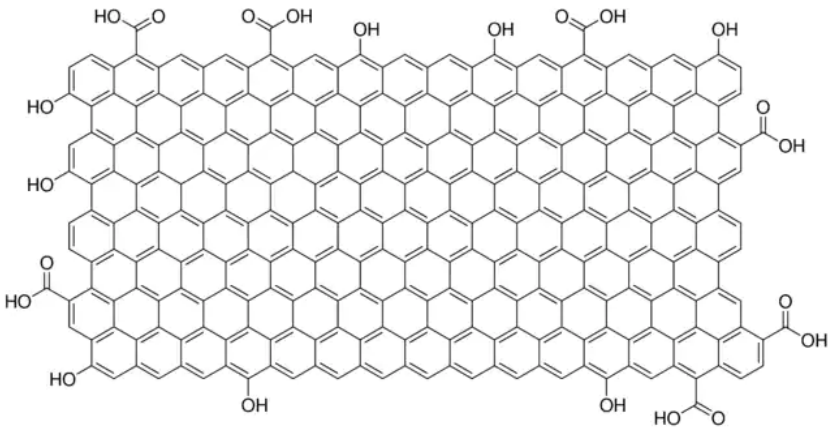

Figure 1.14. Structure of the reduced graphene oxide (rGO).

Table 1.4. Examples of carbon-based photothermal materials. ((*) Biomass-based material for water supply; (**) Biomass-based material for heat generation)

Material	Support (Thermal insulation) / Water supply	Evaporation rate E_1 (kg m^{-2} h^{-1})	Conversion efficiency η (%)	Reference
rGO-Paper	Silisium-based insulating layer/Material (Paper)	1.778	80.6	50
Graphene fibre-Cellulose	Polystyrene/Material (Cellulose(Paper))	1.40	87.9	51
Diatomite-Carbon Nanotube-Agar	Material/Material	1.67	91	52
Carbon dots-Amidon Aerogel (Carbonized)	Polystyrene/Cotton	2.29	93.5	53
Carbonized white radish	Polystyrene/Gauze	1.57	85.9	54(**)
Carbonized sunflower	-/Material	1.51	100.4	55(**)
Carbonized lotus leaf-Paper	Polystyrene/Material (Paper)	1.30	77.5	56(**)
Carbonized walnut shells	(Unknown, presumably put directly on the water)	1.22	81.4	57(**)
Corncob-Carbon Black (3D)	Polystyrene/Material (Corncob)	1.425	(Unknown)	58(*)
Carbonized mushroom	Polystyrene/Material	1.475	78	59 (**)

1.6. Physical factors and evaporation

Good photothermal materials for an evaporator are supposed to have certain physical properties discussed below as well as chemical characteristics presented in sub-chapter 1.5.

1.6.1. Pore structure

One of the important elements for the evaporator is the pore structure.

Firstly, rough surfaces and abundant pores can reduce the vertical reflection of light and promote the absorption of incident light by internal multiple reflection [60].

Secondly, the porous structure is beneficial for water transport and vapour escape. The best-known example is aerogel. For the preparation of aerogels, freeze-drying is often used. The solvent, often water, is removed from the aerogel precursor during this process, and generates pores. Parameters such as the direction of freezing, freezing rate and freezing temperature influence the structure and size of the internal pores. Low-tortuosity pores are desirable for salt rejection, because of the shorter distance between the interface and the bulk water [61].

In nano-sized porous structures, which are smaller than the mean free path of air, thermal insulation is increased by the abundance of porosity [62].

1.6.2. Surface morphology

The texture of the evaporator surface can alter the path of incident light as well as convection near the surface. For hydrophobic surfaces, the surface roughness affects the hydrophobicity to some extent.

Efficient light absorption is a crucial element for evaporation, and the ultimate goal of morphology control is to minimise the outward reflection of incident light [63].

Some research has been inspired by the fascinating structures of animals/biomass. In general, the “crumpled” surface morphology is favourable for light absorption and has a synergistic effect on improving roughness and increasing surface area [64].

1.6.3. Wettability

Water is an essential material for interfacial evaporation. The wettability of the evaporator is, therefore, a factor we need to consider. Hydrophilic materials are beneficial for the transport of water to the surface. However, in general, the transport of water into the pores inevitably increases the thermal conductivity. In other words, it decreases heat localisation.

On the other hand, hydrophobic structures are not able to transfer water, and thus do not contribute to evaporation.

There are three ways to optimise the wettability of an evaporator.

The most conventional method is to assemble the photothermal material with insulation and water transport components to provide water transport and heat management at the same time.

The second method is the structure often referred to as the "Janus structure". The Janus structure refers to a material where the upper part is hydrophobic and capable of absorbing incident light, while the lower part is hydrophilic. The advantage of this structure is that it is less affected by salt deposition during the desalination process, as the salt diffuses back into the water without blocking solar absorption. This also promotes heat containment. It will be mentioned in the following subchapter.

The third method consists of mixing of hydrophobic and hydrophilic structures. This is a type of construction derived from the classic Janus structure. For example, Zhu proved this concept by designing an evaporator consisting of hydrophobic and hydrophilic fibres in the lower and upper parts, respectively. The hydrophobic lower part can moderately pump water due to the capillary effect and thus the upper part can dispose of the appropriate amount of water [65]. As a result, their material achieved a high conversion efficiency (89.7%).

1.7. Evaporator design for solar interfacial evaporation

In addition to the photothermal property of the material, there are several factors that influence evaporation. In other words, it is not enough to prepare a good photothermal material to achieve a good evaporation rate. Minimisation of heat loss, water supply to the interface and evaporation are the three important factors for an evaporator design.

Minimising heat loss means confining heat generated by a photothermal material within the evaporator. Since evaporation only occurs at the phase interface, the heat escaping to the bulk water will not contribute much to evaporation.

The water supply is also necessary for efficient evaporation. If there is not sufficient water in contact with the material, the heat generated will be lost to the outside through thermal dissipation.

There are differences in evaporation between 2D and 3D structures. This difference is mainly due to an evaporation of 0 sun (without light). This factor is valid until the humidity in the evaporation chamber reaches 100%.

Taking these factors into account, several types of evaporator structures for solar interfacial evaporation have been proposed (**Figure 1.15**) [66]. The structure in **Figure 1.15a** consists of a hydrophobic material coated with a hydrophilic layer. The hydrophobic material serves as a thermal insulator due to its buoyancy and low thermal conductivity, and thus minimises the heat escape from the photothermal material. On the other hand, the hydrophilic layer acts as a passage for water to the photothermal material.

In **tables 1.1 – 1.4** in the previous subchapter 1.5, the structures of the evaporators are presented. The evaporators used in the largest number of investigations can be categorised by type (**Figure 1.15a**). Polystyrene and polyethylene are commonly applied as both physical support of the evaporator and heat insulation near the interface. On the other hand, water supply is guaranteed either by direct contact of the photothermal material with the bulk water at the periphery of the support or by means of other hydrophilic material such as paper, cotton and gauze.

Figure 1.15b is an evolved structure of structure (a), referred to as Janus structure. It is based on a porous material with low thermal conductivity. The lower part must be hydrophilic to ensure the passage of water, while the upper part is hydrophobic and able to absorb sunlight and generate heat. Thus, the heat will be used for evaporation in the upper part without any significant loss. The best example is that Wen *et al.* who demonstrated that poly(vinyl alcohol) partially treated with 1H,1H,2H,2H-perfluorooctyltrichlorosilane possessed this property and achieved an evaporation rate of 1.68 kg m^{-2} h^{-1} [67].

Figure 1.15c shows a 3D structure. The 3D structure has two advantages. First, as one can easily imagine, evaporation occurs from side face as well. This factor is favourable for shortening the time to humidity saturation. The other advantage is the localisation of the generated heat, and this structure allows to decrease the heat loss.

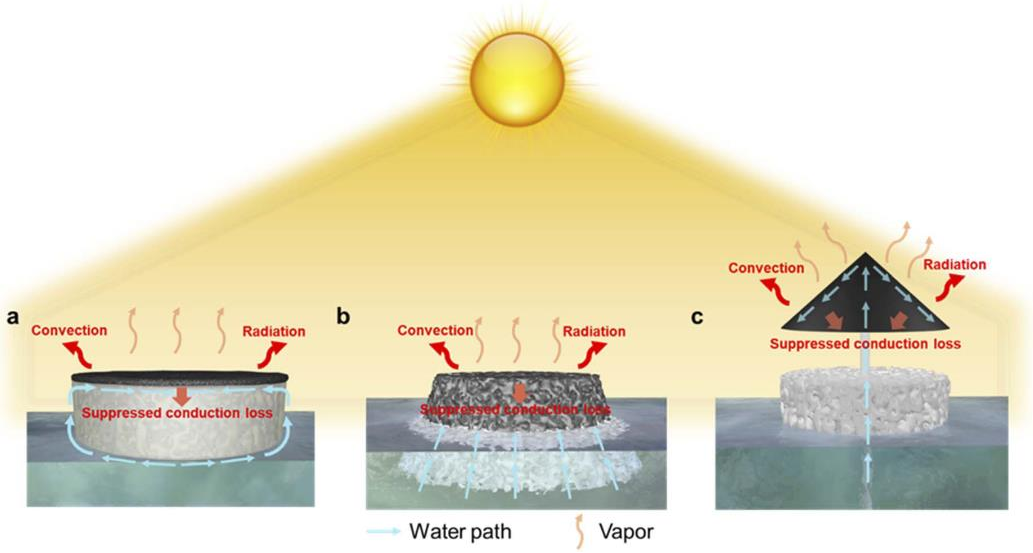

Figure 1.15. Evaporator structures for solar interfacial evaporation [60].

1.8. Evaporation evaluation

In addition to the photothermal device and material, the evaluation of evaporation is also an issue in this field. There are two values for evaporation, the evaporation rate and the conversion efficiency. The method of calculation is discussed below.

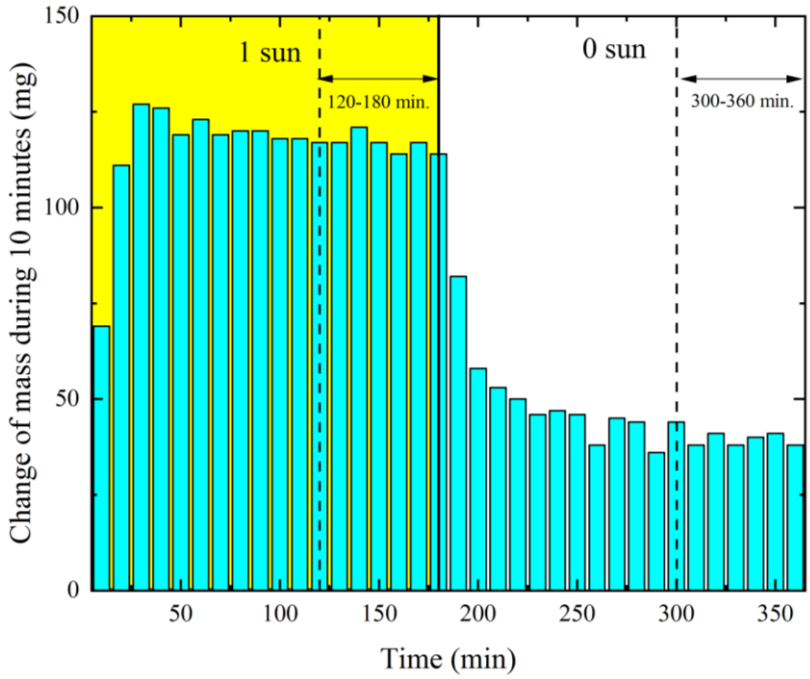

Figure 1.16. Example of the variation of the mass of the whole device (Green moss-PNPG, 05 April 2022).

First, the evaporation under 0 sun must be known. In each measurement, 3 h of irradiation of 1 sun were performed, and then the light was turned off, and the sample was left for 3 h under 0 sun. The mass changes during 120 and 180 min and during 300 and 360 min were adopted for the calculation of evaporation under 1 sun and 0 sun, respectively, in order to minimise the effect of the transient situation accompanied by heating (namely 0-60 min) and cooling (180-240 min) (**Figure 1.16**).

If the interface area s (m^2) is known, the evaporation under 0 sun, E_0 (kg m^{-2} h^{-1}), is estimated using the variation of the mass M_0 (kg) during 300 and 360 min (Eq. 1).

$$E_0 = \frac{M_0}{s} \qquad (1)$$

Then the evaporation under 1 sun, E_1 (kg m^{-2} h^{-1}) can be estimated. This can be calculated if the area of the incident light beam u (m^2) and the variation of the mass M_1 (kg) during 120 and 180 min are known (Eq. 2).

$$E_1 = \frac{M_1 - E_0(s-u)}{u} \qquad (2)$$

The evaporation rate is strongly dependent on weather conditions such as temperature, humidity, wind speed, atmospheric pressure. These factors have a significant impact on evaporation under 0 sun, and in some cases a simple comparison between evaporation rates under 1 sun can lead to a totally wrong conclusion. It is, therefore, important to look at performance using conversion efficiencies (water to vapour). This value means how many percent of the incident light energy is used for steam generation.

The conversion efficiency η is calculated using Eq.3:

$$\eta = \frac{(E_1 - E_0)\, h_{LV}}{Pin} \qquad (3)$$

Where P_{in} is the total energy input (1000 W m^{-2} × 3600 s h^{-1}) and h_{LV} (J kg^{-1}) is the enthalpy required for evaporation.

The enthalpy required for evaporation is composed of two factors, the sensible heat Q (J kg^{-1}) and the latent heat L_v (J kg^{-1}).

$$h_{LV} = Q + L_V \quad (4)$$

The sensible heat Q is the energy stored within the liquid as the temperature increases under the same phase. Since evaporation of water is assumed here (Eq. 5):

$$Q = 4.2 \times 10^3 \, (T_i - T_b) \quad (5)$$

Where T_i (K) corresponds to the interface temperature (Average temperature of the area undergoing irradiation) and T_b (K) is the initial temperature (Ambient temperature)

The sensible heat L_v corresponds to the energy used for the phase transition, i.e. from liquid (water) to gas (vapour) [62] (Eq. 6):

$$L_V = 1.91846 \times 10^6 \left[\frac{T_i}{T_i - 33{,}91}\right]^2 \quad (6)$$

In the case of this research, L_v is much larger than Q (40-60 times larger).

Thus, one can determine the evaporation under 1 sun E_1 (kg m^{-2} h^{-1}) and the conversion efficiency η. Although many publications consider E_1 to be an index of an evaporator's competence, it is more reliable to determine the conversion efficiency, because the evaporation rate is dependent on the condition of this measurement: temperature, atmospheric humidity, and wind speed. This is because the variations of evaporation under 0 sun depend on the weather condition. For example, in our laboratory, the air tends to be dry in winter and humid in summer because of the heating. The inconsistency of these conditions in research can be a reason for confusion when comparing evaporators using the E_1 evaporation rate.

In other words, an evaporation value in a practical operation is marked under 100% humidity after the humidity saturation, and this value is thus lower than a value under ambient humidity. The evaporation under 0 sun E_0 will disappear when the humidity is 100%.

On the other hand, thermodynamic data is taken into account when calculating the conversion efficiency η. This value means a proportion of the energy used for water evaporation in relation to the incident energy. This value is therefore independent of the meteorological situations of the measurement.

1.9. Objectives of this work

As already mentioned in subchapters 1.1 to 1.8, solar interfacial evaporation is a promising technology to alleviate the clean water shortage, which is undoubtedly one of the most serious problems of our century, in a highly environmentally-friendly way. If there is a certain amount

of sunlight with any form of water (salty, contaminated by metals or bacteria, etc.), a suitable evaporator and an easy device for condensation of the vapour, this process can be performed anywhere. Nevertheless, there are several factors that hinder the realisation of this technique.

Firstly, raw materials that are too expensive or not economically accessible should be avoided. As an example of reverse osmosis in Turkey [69], the total cost of operation and investment is at most about \$0.50 m^{-3}. If we want this technique to become commonplace, the cost of producing fresh water should be at the same level as traditional techniques. While the use of gold or silver nanoparticles is an efficient method for the preparation of high performance materials, this approach should be avoided for this reason.

Secondly, since this technology is intended to solve an environmental problem, it is not desirable to use a material that may produce another environmental hazard (secondary contamination). Thus, it is mandatory to avoid the use of materials whose raw materials require multiple manufacturing processes, or materials that necessitate multiple chemical modifications. From this point of view, the reuse of waste and the use of natural materials that exist in abundance are also preferred.

Finally, a material must achieve an interesting conversion efficiency in order to efficiently convert incident energy to condensed water. This requirement corresponds to the physico-chemical properties of a material and the configuration of an evaporator.

In this perspective, the objective of this research is to prepare efficient photothermal materials for vapour generation that are environmentally-friendly and cost-effective.

References

[1] Peter H. Gleick, Water in Crisis: A Guide to the World's Fresh Water Resources, Oxford University Press, New York. p13 (1993)

[2] United Nations, World Population Prospects, Volume I 2019 2-3. (Available at https://population.un.org/wpp/Publications/)

[3] Z. Stevanovic, Karst waters in potable water supply: a global scale overview, Environmental Earth Sciences 78 (2019) 662.

[4] L. Swatuk, M. McMorris, C. Leung, Y. Zu, Seeing "invisible water": challenging conceptions of water for agriculture, food and human security, Candian Journal of Development Studies 36 (2015) 24.

[5] UN World Water Development Report 2021 (Available at https://www.unwater.org/publications/un-world-water-development-report-2021/)

[6] Ritchie, H. & Roser, M. Water Use and Sanitation (Available at https://ourworldindata.org/water-use-stress) (2018).

[7] Intergovernmental Panel on Climate Change, Climate Change 2014 Synthesis Report (Available at https://www.ipcc.ch/report/ar5/syr/)

[8] Rapport mondial des Nations Unies sur la mise en valeur des ressources en eau 2020 (Available at https://www.unwater.org/publications/un-world-water-development-report-2020)

[9] K. Rehman, F. Fatima, I. Waheed, M.S.H. Akash, Prevalence of exposure of heavy metals and their impact onhealth consequences, Journal of Cellular Biochemistry 119 (2018) 157.

[10] R.A. Wahaab, MI. Badawy, Water Quality Assessment of the River Nile System: An Overview, Biomedical and Environmental Sciences 17 (2004) 87.

[11] R. Pradhan, Natural Resources and Violent Conflicts: Water and Energy in Kyrgyzstan, Journal of Asian and African Studies 57 (2022) 650.

[12] G.L. Hassler, The sea as a source of fresh water, UCLA Dept. of Engineering Research Summary 1949.

[13] J. Glater, The early history of reverse osmosis membrane development, Desalination 117 (1998) 297.

[14] S. Loeb and S. Sourirajan, UCLA Dept. of Engineering Report 60-60, July 1960.

[15] E. Jones, M. Qadir, MTH. van Vliet, V. Smakhtin, SM. Kang, The state of desalination and brine production: A global outlook, Science of the Total Environment 657 (2019) 1343.

[16] L.O. Villacorte, S.A.A. Tabatabai, N. Dhakal, G. Amy, J.C. Schippers, M.D. Kennedy, Algal blooms: an emerging threat to seawater reverse osmosis desalination, Desalination and Water Treatment 55 (2015) 2601.

[17] F. Najafi, M. Alsaffar, S.C. Schwerer, N. Brown, J. Ouedraogo, Environmental Impact Cost Analysis of Multi-Stage Flash, Multi-Effect Distillation, Mechanical Vapor Compression, and Reverse Osmosis Medium-Size Desalination Facilities, ASEE's 123rd annual Conference & Exposition (2016).

[18] S. Lattemann, T. Hopner, Environmental impact and impact assessment of seawater desalination, Desalination 220 (2008) 1.

[19] World Energy Council, World Energy Resources: 2013 Survey Chapter 8 (2013). (Available in https://www.worldenergy.org/publications/entry/world-energy-resources-2013-survey)

[20] GLOBAL SOLAR ATLAS (Available in https://globalsolaratlas.info/download, downloaded 7/May/2022)

[21] PVEducation, Standard Solar Spectra (Available at https://www.pveducation.org/pvcdrom/appendices/standard-solar-spectra)

[22] X. Huang, I.H. El-Sayed, W. Qian, M. A. El-Sayed, Cancer Cell Imaging and Photothermal Therapy in the Near-Infrared Region by Using Gold Nanorods, Journal American Chemical Society 128 (2006) 2115.

[23] S. Lal, S. E. Clare, N.J. Halas, Nanoshell-enabled photothermal cancer therapy: impending clinical impact, Accounts of Chemical Research 41 (2008) 1842.

[24] Y. Zeng, J.F. Yao, BA. Horri, K. Wang, Y.Z. Wu, D. Li, H.T. Wang, Solar evaporation enhancement using floating light-absorbing magnetic particles, Energy & Environmental Science 4 (2011) 4074.

[25] O. Neumann, A.S. Urban, J. Day, S. Lal, P. Nordlander, N.J. Halas, Solar Vapor Generation Enabled by Nanoparticles, ACS Nano 7 (2013) 42.

[26] Z. Wang, Y. Liu, P. Tao, Q. Shen, N. Yi, F. Zhang, Q. Liu, C. Song, D. Zhang, W. Shang, T. Deng, Bio-Inspired Evaporation Through Plasmonic Film of Nanoparticles at the Air–Water Interface, Small 10 (2014) 3234.

[27] Y. Liu, S. Yu, R. Feng, A. Bernard, Y. Liu, Y. Zhang, H. Duan, W. Shang, P. Tao, C. Song, T. Deng, A Bioinspired, Reusable, Paper-Based System for High-Performance Large-Scale Evaporation, Advanced Materials 27 (2015) 2768.

[28] Y. Xu, J. Ma, Y. Han, H. Xu, Y. Wang, D. Qi, W. Wang, A simple and universal strategy to deposit Ag/polypyrrole on various substrates for enhanced interfacial solar evaporation and antibacterial activity, Chemical Engineering Journal 384 (2020) 123379.

[29] J.X. Chen, J. Feng, Z.W. Li, P.P. Xu, X.J. Wang, W.W. Yin, M.Z. Wang, X.W. Ge, Y.D. Yin, Space-Confined Seeded Growth of Black Silver Nanostructures for Solar Steam Generation, Nano Letters 19 (2019) 400.

[30] L. Zhou, Y.L. Tan, D.X. Ji, B. Zhu, P. Zhang, J. Xu, Q.Q. Gan, Z.F. Yu, J. Zhu, Self-assembly of highly efficient, broadband plasmonic absorbers for solar steam generation, Science Advances 2 (2016) e1501227.

[31] Z.M. Huang, S.L. Li, X. Cui, Y.P. Wan, Y.F. Xiao, S. Tian, H. Wang, X.Z. Li, Q. Zhao, C.S. Lee, A broadband aggregation-independent plasmonic absorber for highly efficient solar steam generation, Journal of Materials Chemistry A 8 (2020) 10742.

[32] J. Fang, Q.L. Liu, W. Zhang, J.J. Gu, Y.S. Su, H.L. Su, C.P. Guo, D. Zhang, Ag/diatomite for highly efficient solar vapor generation under one-sun irradiation, Journal of Materials Chemistry A 5 (2017) 17817.

[33] M.W. Zhu, Y.J. Li, F.J. Chen, X.Y. Zhu, J.Q. Dai, Y.F. Li, Z. Yang, X.J. Yan, J.W. Song, Y.B. Wang, E. Hitz, W. Luo, M.H. Lu, B. Yang, L.B. Hu, Plasmonic Wood for High-Efficiency Solar Steam Generation, Advanced Energy Materials 8 (2018) 1701028.

[34] C.H. Xiao, W.D. Liang, Q.M.G. Hasi, L.H. Chen, J.X. He, F. Liu, C.J. Wang, H.X. Sun, Z.Q. Zhu, A. Li, Ag/polypyrrole co-modified poly(ionic liquid)s hydrogels as efficient solar generators for desalination, Materials Today Energy 16 (2020) 100417.

[35] X. Wu, M.E. Robson, J.L. Phelps, J.S. Tan, B. Shao, G. Owens, H.L. Xu, A flexible photothermal cotton-CuS nanocage-agarose aerogel towards portable solar steam generation, Nano Energy 56 (2019) 708.

[36] Q.M. Wang, Q.J. Guo, F.F. Jia, Y.M. Li, S.X. Song, Facile Preparation of Three-Dimensional MoS_2 Aerogels for Highly Efficient Solar Desalination, ACS Applied Materials & Interfaces 12 (2020) 32673.

[37] D.D. Qin, Y.J. Zhu, R.L. Yang, Z.C. Xiong, A salt-resistant Janus evaporator assembled from ultralong hydroxyapatite nanowires and nickel oxide for efficient and recyclable solar desalination, Nanoscale 12 (2020) 6717.

[38] J. Wang, Y.Y. Li, L. Deng, N.N. Wei, Y.K. Weng, S. Dong, D.P. Qi, J. Qiu, X.D. Chen, T. Wu, High-Performance Photothermal Conversion of Narrow-Bandgap Ti_2O_3 Nanoparticles, Advanced Materials 29 (2017) 1603730.

[39] H.X. Cao, S. Zhang, T. Jiang, D. Wang, Y.Y. Zhu, Z.T. Bian, Preparing photo-thermal conversion membrane with CuS-Multi walled carbon nanotube (MWCNT) composite for solar-driven interfacial evaporation, Materials Letters 317 (2022) 132145.

[40] P.J. Ying, M. Li, F.L. Yu, Y. Geng, L.Y. Zhang, J.J. He, Y.J. Zheng, R. Chen, Band Gap Engineering in an Efficient Solar-Driven Interfacial Evaporation System, ACS Applied Materials & Interfaces 12 (2020) 32880.

[41] S.Y. Zuo, D.S. Xia, Z.Y. Guan, F. Yang, S. Cheng, H.M. Xu, R.Z. Wan, D.Y. Li, M. Liu, Dual-functional CuO/CN for highly efficient solar evaporation and water purification, Separation and Purification Technology 254 (2021) 117611.

[42] N.S. Fuzil, N.H. Othman, N.H. Alias, F. Marpani, M.H.D. Othman, A.F. Ismail, W.J. Lau, K. Li, T.D. Kusworo, I. Ichinose, M.M.A. Shirazi, A review on photothermal material and its usage in the development of photothermal membrane for sustainable clean water production, Desalination 517 (2021) 115259.

[43] L. Yang, N. Li, C. Guo, J.T. He, S.X. Wang, L.F. Qiao, F.B. Li, L.M. Yu, M. Wang, X.F. Xu, Marine biomass-derived composite aerogels for efficient and durable solar-driven interfacial evaporation and desalination, Chemical Engineering Journal 417 (2021) 128051.

[44] Y. Zou, J.Y. Zhao, J.Y. Zhu, X.Y. Guo, P. Chen, G.G. Duan, X.H. Liu, Y.W. Li, A Mussel-Inspired Polydopamine-Filled Cellulose Aerogel for Solar-Enabled Water Remediation, ACS Applied Materials & Interfaces 13 (2021) 7617.

[45] X.Y. Zhou, Y.H. Guo, F. Zhao, W. Shi, G.H. Yu, Topology-Controlled Hydration of Polymer Network in Hydrogels for Solar-Driven Wastewater Treatment, Advanced Materials 32 (2020) 2007012.

[46] Z.C. Chen, Y.T. Luo, Q. Li, X.M. Chen, Microgroove-Structured PDA/PEI/PPy@PI-MS Photothermal Aerogel with a Multilevel Water Transport Network for Highly Salt-Rejecting Solar-Driven Interfacial Evaporation, ACS Applied Materials & Interfaces 13 (2021) 40531.

[47] J.Y. Li, X. Zhou, P. Mu, F. Wang, H.X. Sun, Z.Q. Zhu, J.W. Zhang, W.W. Li, A. Li, Ultralight Biomass Porous Foam with Aligned Hierarchical Channels as Salt-Resistant Solar Steam Generators, ACS Applied Materials & Interfaces 12 (2020) 798.

[48] I. Ibrahim, S.M. Hossain, D.H. Seo, A. McDonagh, T. Foster, H.K. Shon, L. Tijing, Insight into the role of polydopamine nanostructures on nickel foam-based photothermal materials for solar water evaporation, Separation and Purification Technology 293 (2022) 121054.

[49] J.H. He, T.R. Foysal, H.J. Yang, M. Islam, L.F. Li, W.B. Li, W.G. Cui, A facile and low-cost method to improve the efficiency of solar steam evaporation, Materials Letters 261 (2020) 126962.

[50] Z.Z. Wang, Q.X. Ye, X.B. Liang, J.L. Xu, C. Chang, C.Y. Song, W. Shang, J.B. Wu, P. Tao, T. Deng, Paper-based membranes on silicone floaters for efficient and fast solar-driven interfacial evaporation under one sun, Journal of Materials Chemistry A 5 (2017) 16359.

[51] Q.X. Zhou, H. Li, D.D. Li, B.B. Wang, H. Wang, J.B. Bai, S.H. Ma, G. Wang, A graphene assembled porous fiber-based Janus membrane for highly effective solar steam generation, Journal of Colloid and Interface Science 592 (2021) 77.

[52] J.L. Li, F. Yu, Y. Jiang, L.Y. Wang, X.J. Yang, X.S. Li, W. Lu, X.J. Sun, Photothermal Diatomite/Carbon Nanotube Combined Aerogel for High-Efficiency Solar Steam Generation and Wastewater Purification, Solar RRL 6 (2022) 2101011.

[53] X.S. Xu, Q. Chang, C.R. Xue, N. Li, H.Q. Wang, J.L. Yang, S.L. Hu, A carbonized carbon dot-modified starch aerogel for efficient solar-powered water evaporation, Journal of Materials Chemistry A 10 (2022) 11712.

[54] M.M. Zhu, J.L. Yu, C.L. Ma, C.Y. Zhang, D.X. Wu, H.T. Zhu, Carbonized daikon for high efficient solar steam generation, Solar Energy Materials and Solar Cells 191 (2019) 83.

[55] P. Sun, W. Zhang, I. Zada, Y.X. Zhang, J.J. Gu, Q.L. Liu, H.L. Su, D. Pantelic, B. Jelenkovic, D. Zhang, 3D-Structured Carbonized Sunflower Heads for Improved Energy Efficiency in Solar Steam Generation, ACS Applied Materials & Interfaces 12 (2020) 2171.

[56] M.X. Guo, J.B. Wu, F.H. Li, Q.Q. Guo, H.L. Fan, H.M. Zhao, A low-cost lotus leaf-based carbon film for solar-driven steam generation, New Carbon Materials 35 (2020) 436.

[57] Y.Z. Wang, X.Y. Luo, X.Y. Song, W. Guo, K. Yu, C.Y. Yang, F.Y. Qu, Turning waste into treasure: Carbonized walnut shell for solar-driven water evaporation, Materials Letters 307 (2022) 131057.

[58] H.L. Duan, T. Ling, Y.J. Yan, Y.D. Wang, Corncob-based evaporator for high-efficiency solar vapor generation, Journal of Photonics for Energy 12 (2022) 018001.

[59] N. Xu, X.Z. Hu, W.C. Xu, X.Q. Li, L. Zhou, S.N. Zhu, J. Zhu, Mushrooms as Efficient Solar Steam-Generation Devices, Advanced Materials 29 (2017) 1606762.

[60] Y. Shi, R.Y. Li, Y. Jin, S.F. Zhuo, L. Shi, J. Chang, S. Hong, K.C. Ng, P. Wang, A 3D Photothermal Structure toward Improved Energy Efficiency in Solar Steam Generation, Joule 2 (2018) 1171.

[61] X.Y. Dong, L.T. Cao, Y. Si, B. Ding, H.B. Deng, Cellular Structured CNTs@SiO_2 Nanofibrous Aerogels with Vertically Aligned Vessels for Salt-Resistant Solar Desalination, Advanced Materials 32 (2020) 1908269.

[62] H.J. Zhan, J.F. Chen, H.Y. Zhao, L. Jiao, J.W. Liu, S.H. Yu, Biomimetic Difunctional Carbon-Nanotube-Based Aerogels for Efficient Steam Generation, ACS Applied Nano Materials 3 (2020) 4690.

[63] Y.L. Chen, G.M. Zhao, L.P. Ren, H.J. Yang, X.F. Xiao, W.L. Xu, Blackbody-Inspired Array Structural Polypyrrole-Sunflower Disc with Extremely High Light Absorption for Efficient Photothermal Evaporation, ACS Applied Materials & Interfaces, 12 (2020) 46653.

[64] S. Kim, Z. Tahir, M.U. Rashid, J.I. Jang, Y.S. Kim, Highly Efficient Solar Vapor Generation via a Simple Morphological Alteration of TiO_2 Films Grown on a Glassy Carbon Foam, ACS Applied Materials & Interfaces 13 (2021) 50911.

[65] Y.Q. Zhu, G.L. Tian, Y.W. Liu, H.X. Li, P.C. Zhang, L. Zhan, R. Gao, C. Huang, Low-Cost, Unsinkable, and Highly Efficient Solar Evaporators Based on Coating MWCNTs on Nonwovens with Unidirectional Water-Transfer, Advanced Science News 8 (2021) 2101727.

[66] X.H. Han, S.Q. Ding, H.Y. Hu, S.R. Wang, Recent advances in structural regulation and optimization of high-performance solar-driven interfacial evaporation systems, Journal of Materials Chemistry A 10 (2022) 18509.

[67] B.Y. Wen, X.Y. Zhang, Y.H. Yan, Y.Q. Huang, S. Lin, Y.L. Zhu, Z.P. Wang, B.H. Zhou, S.H. Yang, J. Liu, Tailoring polypyrrole-based Janus aerogel for efficient and stable solar steam generation, Desalination 516 (2021) 115228.

[68] X. Zhao, X.J. Zha, L.S. Tang, J.H. Pu, K. Ke, R.Y. Bao, Z.Y. Liu, M.B. Yang, W. Yang, Self-assembled core-shell polydopamine@MXene with synergistic solar absorption capability for highly efficient solar-to-vapor generation, Nano Research 13 (2020) 255.

[69] D. Akgul, M. Cakmakci, N. Kayaalp, I. Koyuncu, Cost analysis of seawater desalination with reverse osmosis in Turkey, Desalination 220 (2008) 123.

Chapter 2: Materials and Methods

2.1. Materials

N-Phenylglycine (NPG, 97%) and ammonium persulfate (APS, 98%) were purchased from Merck (France). Sulfuric acid (H_2SO_4, 95%), ethanol (99.8%), hydrochloric acid (HCl, 37%) were obtained from Fisher Scientific (France).

The raw petroleum coke was supplied by Shandong Chambroad Petrochemical Company, P.R. China, with a sulfur content of 2~5% and a porous surface structure. Petroleum coke was preliminarily crushed and ground with mortar, and its particle size was < 1 mm. Then, a planetary ball mill was used for ball milling. The volume ratio between the abrasive and the ball mill bead was 1:1. The rotational speed was 350 rpm and the grinding time was 8 h. The abrasive in the ball mill vessel was stirred every 2 h to make it fully ground, so as to prevent its powder from adhering to the inner wall of the ball mill vessel. The ball-milled petroleum coke powder was sieved to maintain its particle size at < 20 μm. The sieved petroleum coke powder was washed by 15 wt.% hydrochloric acid (HCl) solution and ethanol sequentially. Finally, the powder was suction filtrated and dried.

The green moss was collected on the CNRS campus, 50 Avenue de Halley, Villeneuve-d'Ascq, France.

The filters (named **New Filter** in the 5th chapter) for analyses (SEM-EDX, ultraviolet/visible/near-infrared spectrometry, heat profile in dried state, water contact angle, FTIR, and TGA) were extracted from a non-used commercial product (Filter Kings, Philip Morris International). Cigarette butts for vapor generation and purification properties tests were collected at the CNRS campus, 50 Avenue de Halley, Villeneuve-d'Ascq, France.

Seawater for vapour generation and seawater distillation was taken from the North Sea (Ostend, Belgium). The bacteria used in this study were derived from an *E. coli* K12 MG 1655 strain (Gram negative).

2.2. Description of the characterization techniques

2.2.1. Scanning electron microscopy-Energy-dispersive X-ray spectroscopy (SEM-EDX)

Scanning electron microscopy (JEOL, JSM-7800F) was used to obtain information on the morphology of the samples.

This technique involves projecting an electron probe onto a sample to obtain an image of the surface. The atoms exposed to the radiation are excited and emit secondary electrons. The energy of these electrons is low. A clear image can be acquired by these secondary electrons (LED, Lower Electron Detector).

The other detector (BED-C, Backscattered Electron Detector) is used to detect backscattered electrons. These electrons are scattered by an atom in an almost elastic way. High energy electrons are therefore detected. Atoms with a large atomic number Z emit a lot of electrons, and are therefore seen in white on the image.

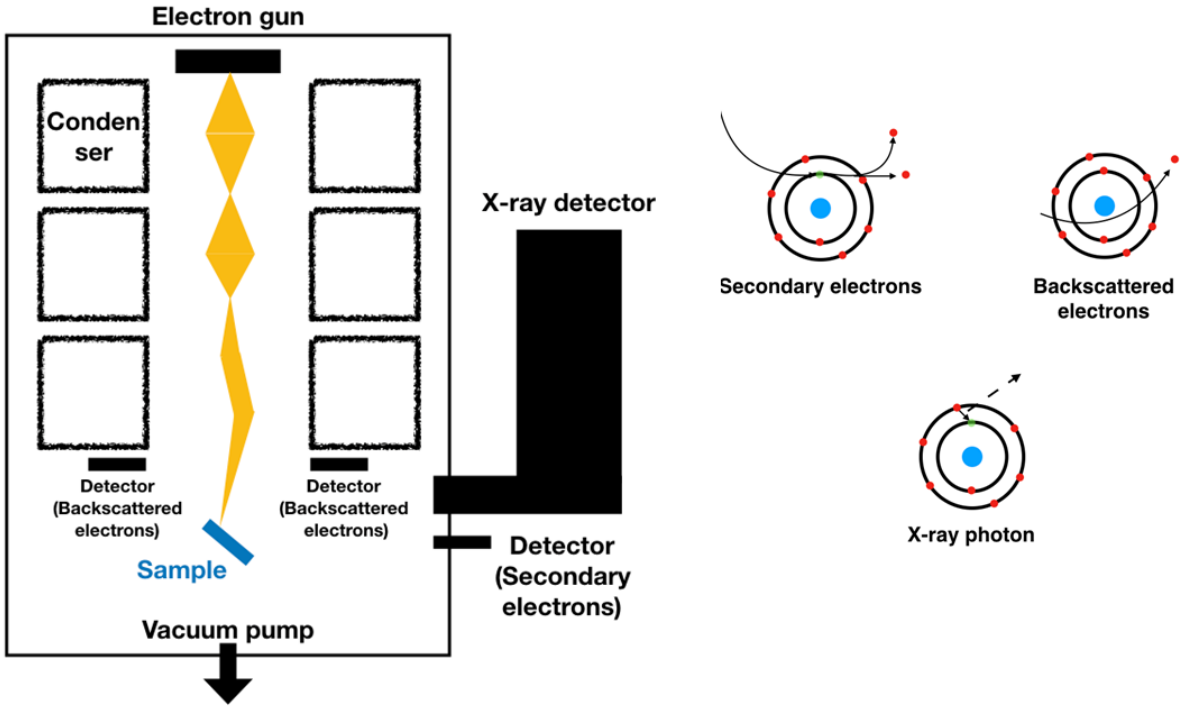

Figure 2.1. Principle of the SEM-EDX

Energy dispersive X-ray (EDX) spectroscopy is a practical technique for elemental analysis. When an atom interacts with a high-energy electron, an electron in an inner orbital is ejected. Relaxation occurs when an electron in an outer orbital moves towards this hole. This relaxation is accompanied by the emission of an X-ray photon. The energy of this X-ray photon is specific to each element.

The accelerating voltage was set at 2.0-5.0 kV for SEM and 15.0 kV for EDX.

2.2.2. Raman scattering analysis

Raman spectroscopy (LabRam HR Micro-Raman system (Horiba Jobin Yvon) equipped with a 473 nm diode laser) is a method for identifying the structure of molecules and particularly suited for the analysis of graphitic-based materials.

When a sample is irradiated by photons, several phenomena can be observed: part of light is reflected, another part passes through the sample, and other is scattered. A large part of the scattering is elastic scattering, i.e. scattering in which the photons do not lose energy. This phenomenon is called Rayleigh scattering (**Figure 2.2**).

A very small part of the scattering is inelastic (1 photon of 10 M photons). In this scattering, the photons exchange energy with the atoms to change their vibrational level. As a result, photons with altered energy can be observed. This is called Raman scattering.

Most of the time, the energy of the observed photons is lower than the energy of the incidence. In other words, a wavelength extension can be observed. This is called Stokes scattering. The opposite is anti-Stokes scattering, but it is the minority process.

The wavenumber shift between the incident wavenumber and the scattering wavenumber is commonly used to express the change in photon energy. When the vibration causes a change in the polarizability (momentary deformation of the electron cloud around a bond) of a molecule, the Raman shift can be observed. In combination with FTIR spectroscopy, the structure of molecules will be clearly identified.

In this work, the visible light is focused by a 100× objective. The scattered light is collected by this lens in backscattering, and scattered by a monochromator with a focal length of 1800 mm and detected by a CCD camera.

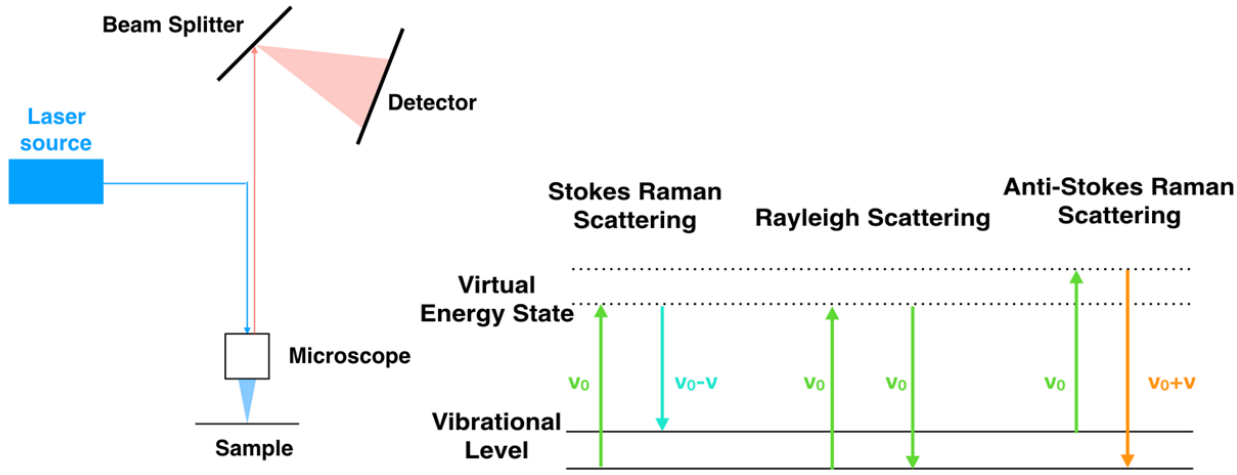

Figure 2.2. Principle of Raman scattering analysis.

2.2.3. X-ray diffraction (XRD)

X-ray diffraction (XRD) was carried out for the determination of the phases, existing in the materials investigated in this work, by Bruker D8 Advance A25 (equipped with a LynxEye XET detector).

This technique is generally used to study the phases of crystalline materials. It involves bombarding a sample with X-rays and measuring the intensity of the scattered X-rays at different angles. The X-rays diffracted by different atoms only interfere constructively with each other at certain angles specific to the crystal structure.

In **Figure 2.3**, the wave reflected from one diffracting plane travels less than that reflected from the next plane, and this difference can be calculated as $2d\sin\theta$, where θ is the angle between the reflected beam and the diffracting plane. Constructive interference only occurs when this path difference is an integer multiple of the wavelength (Eq. 7):

$$\text{Bragg's Law: } 2dsin\theta = n\lambda \quad (7)$$

The phases in a sample can be identified by comparing the database and the angle 2θ where strong diffractions are observed.

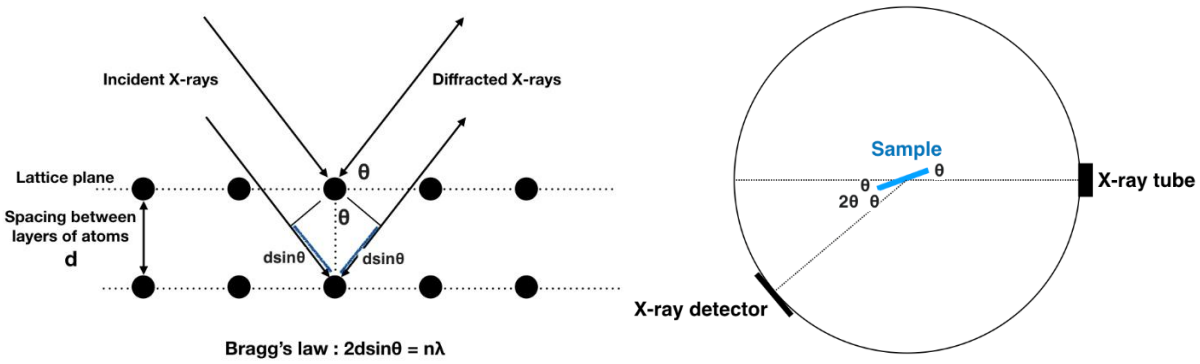

Figure 2.3. Left: Bragg's Law, Right: X-ray diffraction by a sample

2.2.4. UV-Vis/NIR spectrophotometry

To acquire reflectance spectra, a UV-Vis/NIR spectrometer (PerkinElmer, LAMBDA 950) was used. For the green moss, pellets (100 mg, ⌀ = 13 mm, Pressure: 600 MPa) were prepared. For the cigarette filters, 25 mg (12 mm × 6 mm × 2 mm) of the samples were placed directly into the measurement chamber.

"Universal Reflectance Accessory" was used to acquire the reflectance spectrum, and the angle of incidence was set at 45 degrees. The probed wavelength is 300-2000 nm in this work.

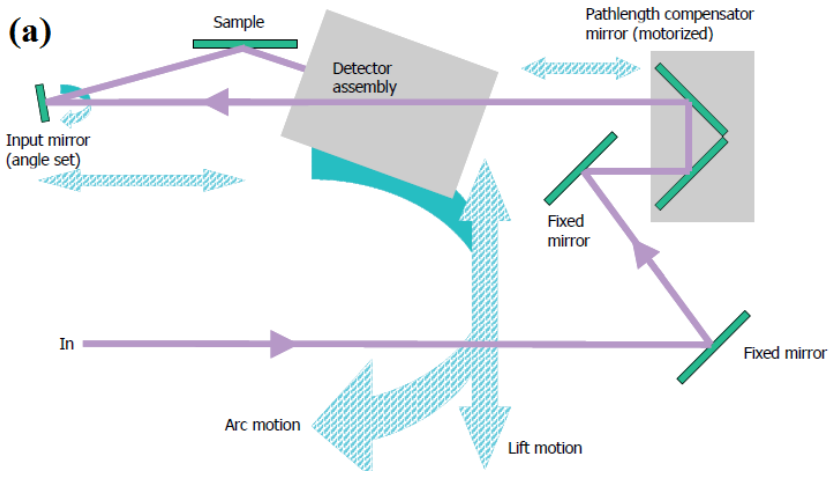

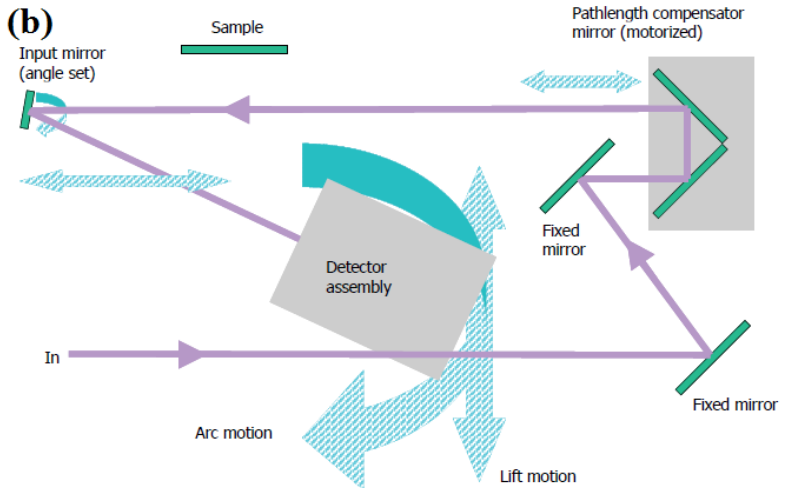

Figure 2.4. Diagram of the Universal Reflectance Accessory (a: Measurement, b: Calibration)

2.2.5. Contact angle measurements

The wetting properties of the samples were examined by measuring the contact angle of an 8 µL water droplet with a goniometer (Ossila, L2004A1) at 5 different locations on the sample (**Figure 2.5**).

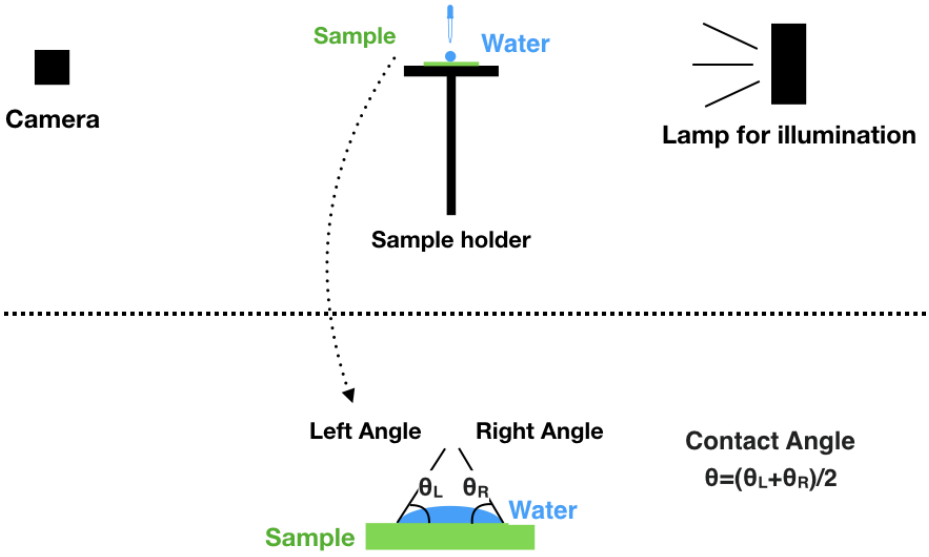

Figure 2.5. Measurement of the water contact angle.

The camera behind the sample captures images. The time interval between the images was 1.2 s (Chap. 3 and 4), and 0.1 s (Chap. 5). After capturing the pictures, a software automatically detects a water droplet on the sample and measures the left and right contact angles from the pictures.

The average contact angle was calculated for each photo using Eq. 8:

$$\theta = \frac{\theta_L + \theta_R}{2} \qquad (8)$$

Where θ_L is the left angle and θ_R is the right angle.

2.2.6. Fourier-transform infrared (FTIR) spectroscopy

Information on the chemical structure/composition of the samples was obtained by Fourier transform infrared spectroscopy (Thermo Fisher Scientific, Nicolet 8700).

This method involves irradiating a sample with infrared radiation and recording the absorption. The energy of the infrared radiation is relatively low, and this energy is used to change the vibrational modes of a molecule. When the frequency of the incident radiation is at the same frequency of an allowed vibration frequency and the vibration produces a change in the electric charge distribution (change in the electric dipole moment of the molecule), absorption will be observed at that frequency. There is a particular vibrational wavenumber for each bond, and it is therefore possible to identify groups by interpreting a transmission spectrum.

For this analysis, approximately 1-2 mg of solid sample was ground and mixed with 250 mg of KBr, and the mixture was pressed (approximately 600 MPa) to obtain a pellet. The wavelength range was 4000 to 650 cm^{-1}.

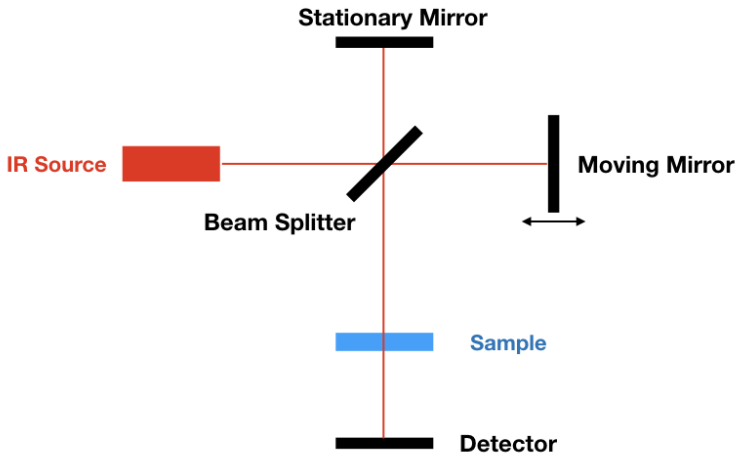

Figure 2.6. Instrument for FTIR analysis.

2.2.7. X-ray photoelectron spectroscopy (XPS)

To obtain information on elemental composition and chemical bonds, photoelectron spectrometry (XPS, Kratos Axis ULTRA DLD, with a monochromatised Al Kα source) was adopted.

In this technique, a sample is irradiated with X-rays to eject electrons. Once the sample receives X-ray energy, an electron can be ejected from the sample. The energy of this electron changes depending on the orbital to which the electron belonged (**Figure 2.7**).

By conservation of energy, the energy of an ejected electron can be expressed as follows (Eq. 9):

$$h\nu = E_K + E_B + \Phi \qquad (9)$$

Where $h\nu$ is the energy of an X-ray, Φ is the work function of an instrument, E_B is the binding energy of the orbital to which the ejected electron belongs, and E_K is the kinetic energy of a detected (ejected) electron. Φ, E_K, and $h\nu$ are known values, and the binding energy can therefore be easily calculated using Eq. 10:

$$E_K = h\nu - E_B - \Phi \quad (10)$$

This instrument is able to count electrons according to the kinetic energy of the electrons. This energy is sensitive to the orbital and the bond that an electron forms. Thus, information about the bond, the element, etc. can be collected.

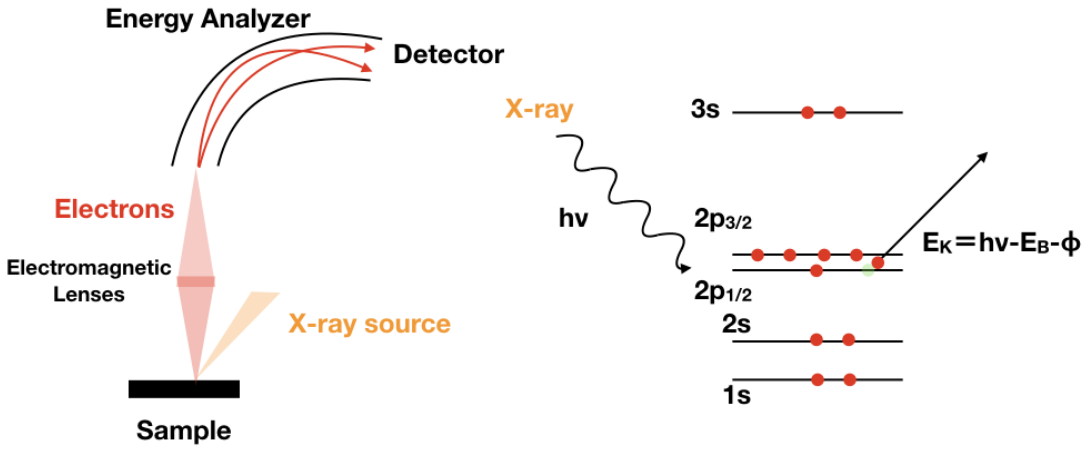

Figure 2.7. Instrument and principle of XPS analysis.

2.2.8. Thermogravimetric analysis (TGA)

Thermogravimetric analysis (TGA, Netzsch, TG 209 F3 Tarsus) was used to measure the variation of the mass of samples upon thermal heating.

With the TGA, the temperature of the furnace in which a sample is placed increases at a constant rate. The balance is also equipped to record the mass of the sample as a function of time (as a function of temperature). This provides information on the characteristics of materials at high temperatures.

The speed was set at 10 °C min^{-1} and the temperature was increased from room temperature to 910 °C. The measurements were carried out under nitrogen (N_2).

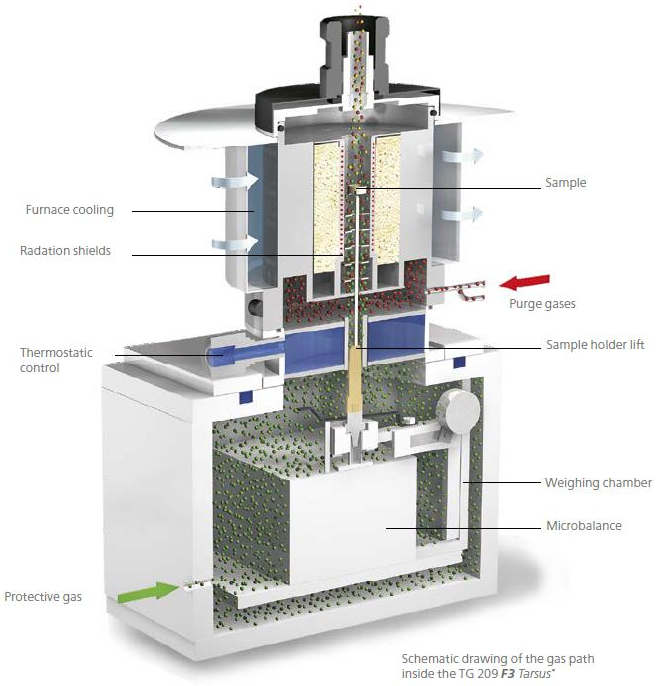

Figure 2.8. Structure of TG 209 F3 Tarsus.

2.3. Vapor generation

2.3.1. Instruments

The solar simulator (QuantumDesign, LSN150) was operated with the AM 1.5G filter for consistency with other research. As already mentioned, 1 sun (1000 W m^{-2}) is commonly used in the field of solar interfacial water evaporation as a unit of incident light power to facilitate

the calculations. The intensity of the incident light was calibrated to 1000 W m^{-2} using the photovoltaic panel which is previously calibrated between the output voltage and 1000 W m^{-2} of incident light (AM 1.5G) (**Figure 2.9**).

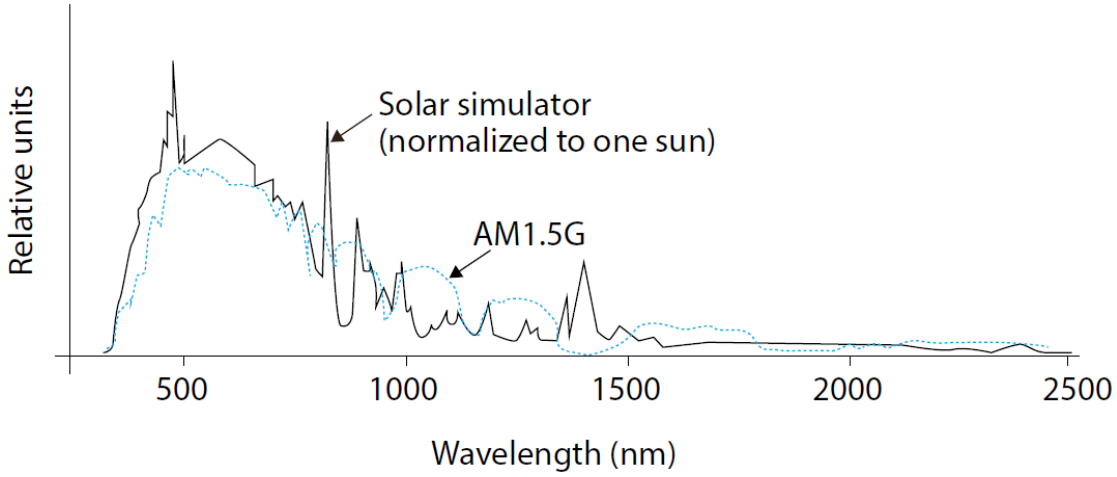

Figure 2.9. Spectrum of the light produced by the simulator.

A 0.001 g precision balance (Denver Instrument, SI-203) was used to measure the total mass of the device (beaker and evaporator). The mass was recorded manually every 10 minutes.

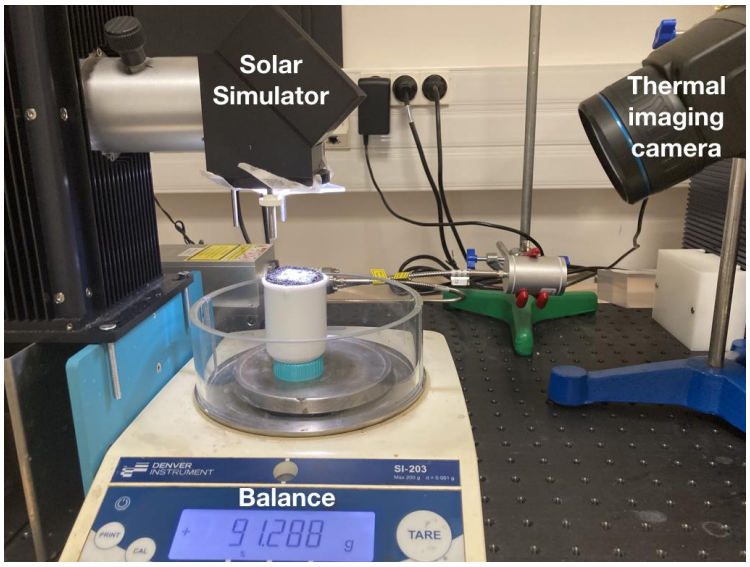

Figure 2.10. Mass and temperature measurement devices.

During irradiation, the surface temperature (the interface temperature) and temperature distribution images were measured and captured with the thermal camera (FLIR A655sc 25°, Teledyne FLIR LLC) (**Figure 2.10**).

2.3.2. Atmospheric temperature and humidity

Weather conditions are important factors. In general, in the laboratory, evaporation is high on a sunny day in winter because of the lower humidity (the temperature inside the building is maintained all year round by heating, so humidity tends to be low in winter). In summer, however, evaporation is low because the humidity is relatively high.

Humidity can be measured with a normal thermometer. The wet bulb temperature (T_w) is the temperature recorded by a thermometer with a water-soaked paper towel on the bulb. The dry temperature (T_d), on the other hand, is the temperature recorded by a conventional bare thermometer.

The saturation vapour pressure of water at a certain temperature (= T_d) can be calculated according to Wagner's law [1] (Eq. 11):

$$P_s = P_c \, exp\left(\frac{Ax+Bx^{1.5}+cx^3+Dx^6}{1-x}\right) \qquad (11)$$

Where $x = 1 - \frac{T_d\,(K)}{647.31}$, $Pc = 221200$ hPa, $A = -7.7760$, $B = 1.4788$, $C = -2.7877$, $D = -1.2492$ [2].

On the other hand, the water vapour pressure P_v (hPa) can be determined by the Sprung's law (Eq. 12):

$$P_v = P_s(T_w) - AP(T_d - T_w) \qquad (12)$$

where A = 0.0006662, P (hPa) is the value of the atmospheric pressure.

Finally, the relative humidity HR (%) can be obtained from the results of Eq. 11 and 12:

$$HR = \frac{P_v}{P_s} \times 100 \qquad (13)$$

Table 2.1 summarises some results of the humidity calculation for dry and humid conditions. Even at abnormally low (970 hPa)/high (1050 hPa) pressures, the deviations of the humidity from the case of 1 atm = 1013.25 hPa are less than 1%. In this work, P = 1013.25 hPa was therefore adopted as the ambient atmospheric pressure for the calculation of relative humidity.

Table 2.1. Examples of relative humidity calculations under various conditions

Dry temperature T_d (°C)	Humid temperature T_w (°C)	Atmospheric pressure P (hPa)	Relative humidity HR (%)
20.0	15.0	970.00	59.5
20.0	15.0	1013.25	58.9
20.0	15.0	1050.00	58.4
20.0	13.0	970.00	45.2
20.0	13.0	1013.25	44.4
20.0	13.0	1050.00	43.7
22.0	15.0	970.00	47.9
22.0	15.0	1013.25	47.1
22.0	15.0	1050.00	46.5

2.4. Seawater distillation and sterilisation of contaminated water

2.4.1. Condensation

The distillation was carried out with a homemade device. A poly(methyl methacrylate) plate (Goodfellow; thickness = 2.0 mm) was used to construct a vapour condensation device (**Figure 2.11**). The beaker equipped with an evaporator is positioned in the middle of this device and this device with the lid is placed under the light source.

Figure 2.11. Condensation device.

After several hours (normally more than 3 h) of irradiation, water droplets can be seen covering the walls of the device (**Figure 2.12**).

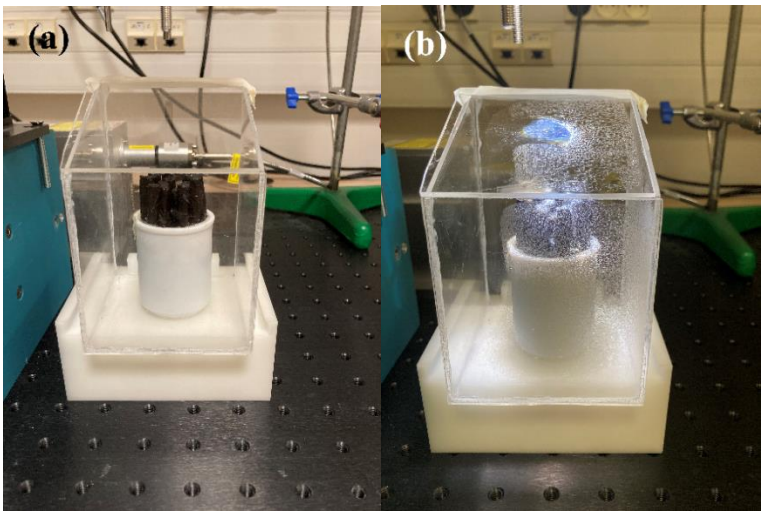

Figure 2.12. Water droplets on the walls of the device (**a**) before irradiation and (**b**) 3 h later

2.4.2. Inductively coupled plasma - optical emission spectrometry (ICP-OES)

The element concentrations in the initial seawater and in the condensed water were measured by ICP-OES (Agilent technologies, ICP-OES 5110).

This technique is used to determine the content of inorganic elements in a liquid. The liquid is placed into an argon plasma as an aerosol to vaporise at extremely high temperatures. This process causes atomisation and ionisation.

In ICP-OES, the focus is on the emission of atomic light. Excited atoms emit photons with an element-specific energy when they return to the initial state. The light is separated depending on wavelength by a spectrometer and the intensity is measured. The element concentration is calculated by comparing the result with data from a known solution (**Figure 2.13**).

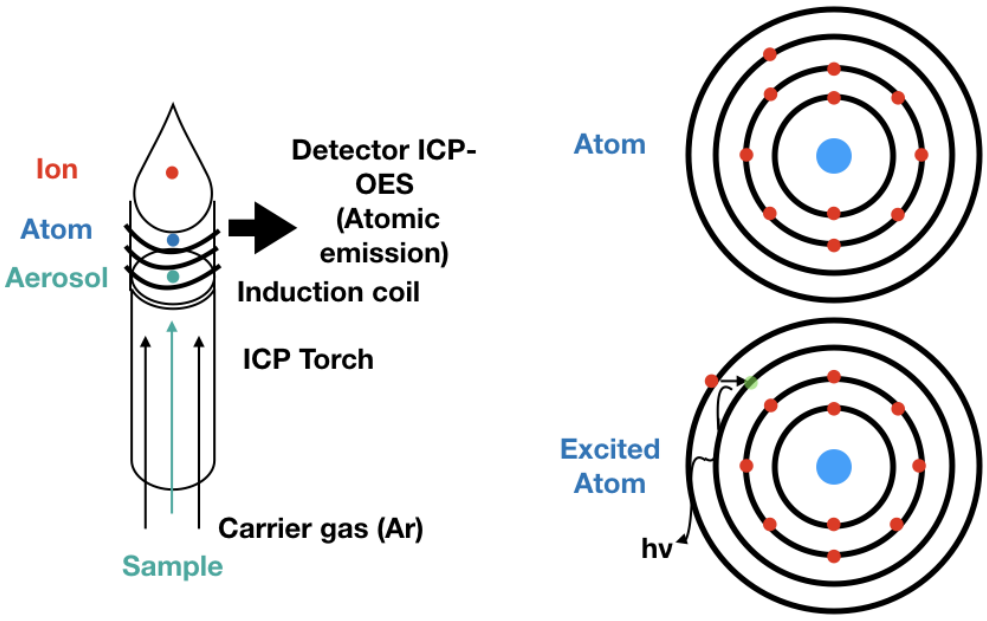

Figure 2.13. Left: Schematic of ICP; right: Atom in ground and excited states.

2.4.3. Bacteria

(a) Culture of bacteria

The bacteria used in this study were derived from an *E. coli* K12 MG 1655 strain (Gram negative). A single colony of *E. coli* from an agar plate (LB agar) was inoculated overnight into LB medium at 35°C with moderate agitation (100-150 rpm). The pre-culture was diluted 10-fold and left under agitation for another 3-4 h until the optical density at 600 nm (OD_{600}) reached 0.6-1. The culture was then centrifuged at 4500 rpm for 5 min and the pellet was diluted to 1 × 10^8 CFU mL^{-1} (OD ~ 0.1) in sterile 0.9% NaCl (100 mL).

(b) Biological titration (Bioassay)

Figure 2.14 describes a biological titration procedure adopted in this work. First, a sample is diluted with a sterile physiological salt water solution (NaCl, 0.9%) by 10^1, 10^2, 10^3...10^8 etc. Since the concentration of a solution is not known, different dilution levels must be tested. For this purpose, a petri dish was separated into several placements to incubate for different dilution levels. 20 µL of solution from each dilution was taken and deposited on the agar (LB agar,

Luria/Miller). As soon as the solutions were impregnated into the agar, the petri dish was incubated at 37 °C for 24 h.

If there are sufficient bacteria in a diluted solution (but not too many to count manually), colonies of bacteria can be seen visually after the incubation period. The assay can be performed with manual counting.

For example, if 22, 24, and 23 colonies of bacteria can be counted in dilution compartment 10^5 on 3 petri dishes, the initial bacterial content can be estimated with a simple calculation, and it will be 1.15×10^8 CFU mL^{-1}.

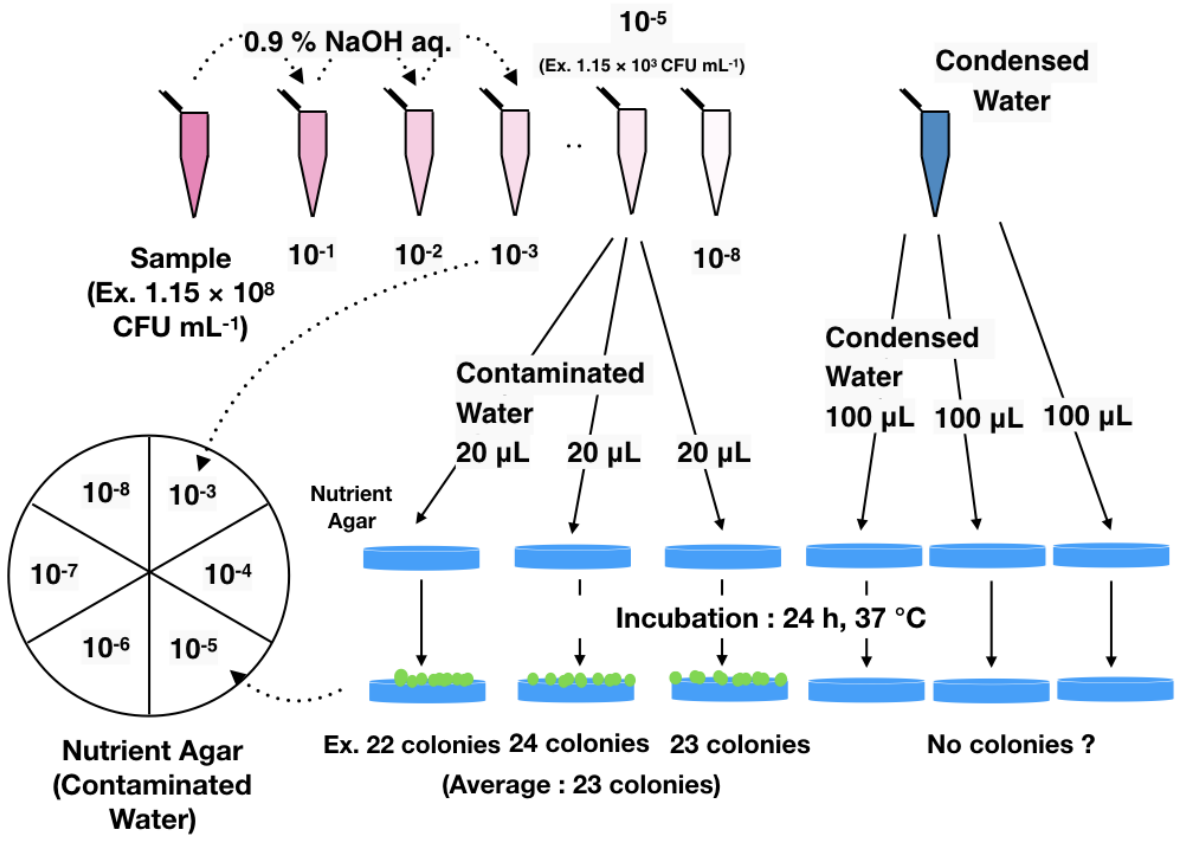

Figure 2.14. Titration of bacteria.

References

[1] W. Wagner, A New Correlation Method for Thermodynamic Data Applied to the Vapor Pressure Curve of Argon, Nitrogen, and Water, J. T. R. Watson (trans. and ed.). IUPAC Thermodynamic Tables Project Centre, London (1977).

[2] Y. Chernyak, Phase Equilibria in Binary Mixtures of Water with Cyclic Alkylene Carbonates, Journal of Chemical & Engineering Data 53 (2008) 603.

Chapter 3: Green moss - poly(*N*-phenylglycine)

3.1. Introduction

There is a growing awareness that water shortage is one of the most preoccupying concerns in the 21st century. Approximately 40% of the world population suffers from water scarcity in terms of quality or quantity, because of the excessive consumption of water and various contaminations [1].

In that context, various desalination technologies, such as reverse osmosis and distillation [2, 3], have been conceived in order to produce freshwater out of seawater, which is omnipresent and represents 96.5% of water resources on the globe [4]. However, these technologies require high energy input, which has a detrimental effect on the environment. In addition, frequent maintenance and large-scale plants are required for the stable operation of those processes. These factors are not favorable for installation in remote regions.

These days, distillation using solar-driven interfacial evaporation has been attracting more and more attention [5]. This technology can exploit solar energy – an inexhaustible energy source – for desalinizing the seawater and sterilizing contaminated water with the assistance of photothermal materials. This technology is compatible with the fact that the countries in the Middle East and Asia, suffering from severe water stress, are mostly located in low latitude regions [6], where they have much potential to use the sun's energy.

Various kinds of photothermal materials have been investigated for accelerating water evaporation, including next to semiconductors [7–9] and plasmonic metals [10–12], carbonized biomass materials [13–15], and polymers [16–18], etc. However, more improvements are required in terms of vapor production efficiency, fabrication cost, or accessibility of the raw materials. Indeed, accessibility of the raw materials is one of the most important factors for the installation of the device in many remote places over the world.

Green moss (GM), an abundant biomass, exhibits all the attributes of a good solar vapour generation material. Indeed, we have lately demonstrated that GM, owing to its hydrophilicity, wide absorption in the solar spectrum, enhanced ability to transform light-to-heat, and low cost represents a highly effective photothermal material for brackish water desalination [19].

Meanwhile, poly(*N*-phenylglycine) (PNPG), an analogue of polyaniline, owns good photothermal properties and has been applied for photothermal eradication of tumors [20] and bacteria [21], but also enhanced properties for energy storage applications [22, 23].

The aim of this chapter is to take advantage of the photothermal properties of both GM and PNPG through the formation of a hybrid GM/PNPG material to increase the absorbance of incident light, the vapor generation efficiency and sterilization property. PNPG was coated on the GM surface through a simple polymerization process of *N*-phenylglycine monomer. The obtained GM/PNPG displayed enhanced solar conversion efficiency of 76.5 ± 3.9% under 1 sun irradiation, as compared to 64.2 ± 3.0% recorded for the pristine GM under otherwise identical conditions. In addition, the hybrid material was applied for effective desalination of sea water and bacteria removal with high efficiency.

3.2. Experimental section

3.2.1. Preparation of green moss (GM)

Once the green moss (GM) was collected, it was washed copiously with water for removing fine sand and mud. Then, it underwent a drying step at 60 °C for overnight. Subsequently, the GM was soaked in ethanol for approximately 7 h in order to dissolve organic components and finally dried at 60 °C for 2 h [19].

3.2.2. Preparation of green moss - poly(*N*-phenylglycine) (GM-PNPG) composite

The synthesis of the GM-PNPG composite was performed according to a precedent work [21]. First, *N*-phenylglycine monomer (NPG, 212 mg) and green moss (800 mg) were placed in 0.1 M H_2SO_4 aqueous solution (100 mL). Separately, ammonium persulfate (APS, 320 mg) was dissolved in 0.1 M H_2SO_4 aqueous solution (100 mL). Then, the APS solution was poured slowly to the NPG solution at 0 °C (ice-water bath) over one hour under magnetic stirring. The resulting solution was left in the ice-water bath for 24 h with magnetic stirring. The modified green moss was collected with centrifugation (4,400 rpm, 5 min) and washed several times with water. Finally, the final product was dried overnight at 60 °C. Henceforth, the obtained samples are denoted as GM-PNPG (**Fig. 3.1**).

Figure 3.1. Photos of pristine GM (left) and GM-PMPG (right).

3.2.3. Structure of the evaporator

Vapour generation tests were performed on a home-made device consisting of a 50 mL beaker, paper towel, and polystyrene foam (used for plastic food trays). The beaker was filled with water or seawater (50 mL) and the green moss (380 mg) was loaded on the polystyrene foam (**Fig. 3.2**). The same configuration was used also in the 4th chapter.

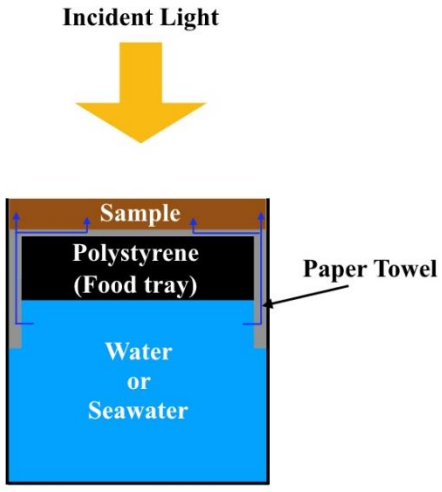

Figure 3.2. Illustration of the home-made device for vapor generation tests.

3.3. Results and discussion

3.3.1. Polymerization of *N*-phenylglycine on the green moss surface (GM-PNPG)

Figure 3.3 shows the SEM micrographs of the surface of green moss (GM) before and after modification with poly(*N*-phenylglycine) (PNPG). The surface of the pristine GM exhibits orderly arranged patterns (**Fig. 3.3 a,b**), which were not obvious after PNPG formation (**Fig. 3.3 c,d**). The disappearance of the initial orderly arranged patterns is a clear indication of PNPG deposition on the GM surface.

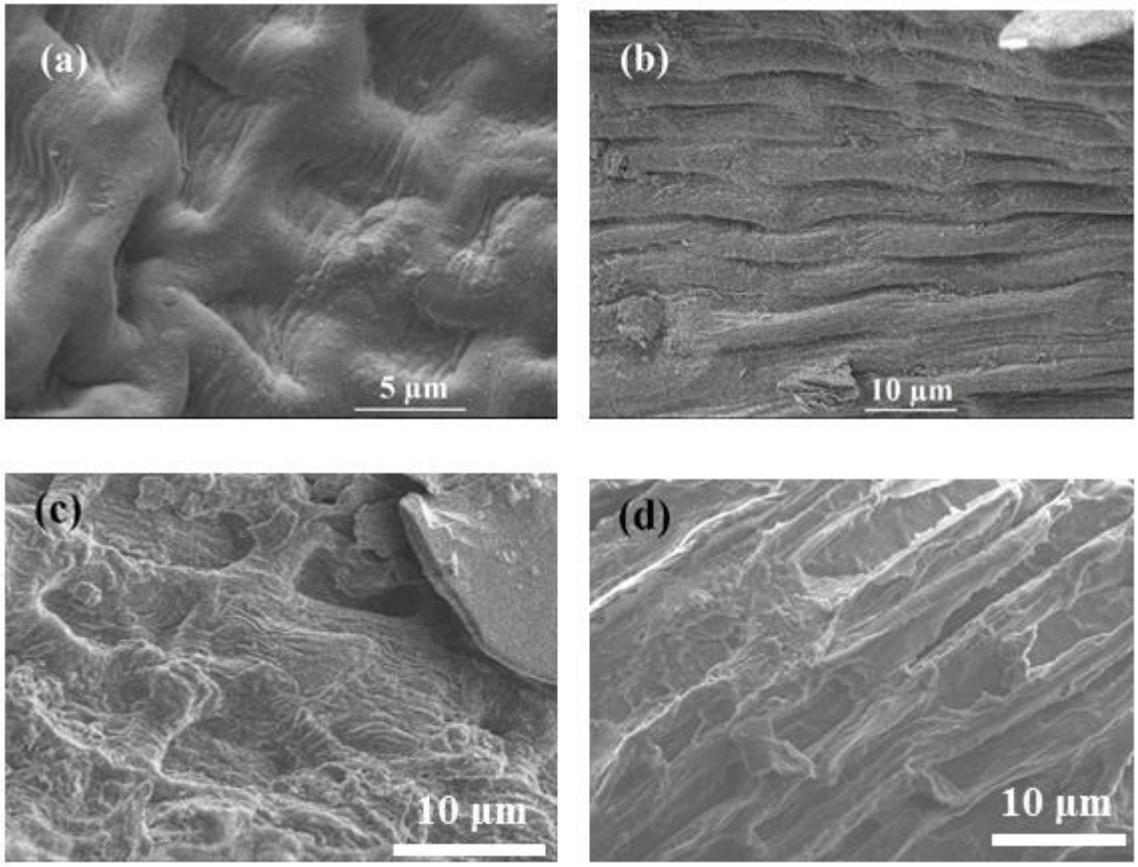

Figure 3.3. SEM images of the GM samples before polymerization (**a, b**), and after coating with PNPG (GM-PNPG) (**c, d**).

Figure 3.4 depicts the reflectance spectra in the ultraviolet/visible/near-infrared range. The pristine GM exhibits good absorption properties throughout the UV to NIR range. This property is beneficial for light harvesting. After the polymerization of PNPG on the surface of the green moss, the reflectance of GM-PNPG decreased, which implies that PNPG layer promotes the absorption of visible and infrared light.

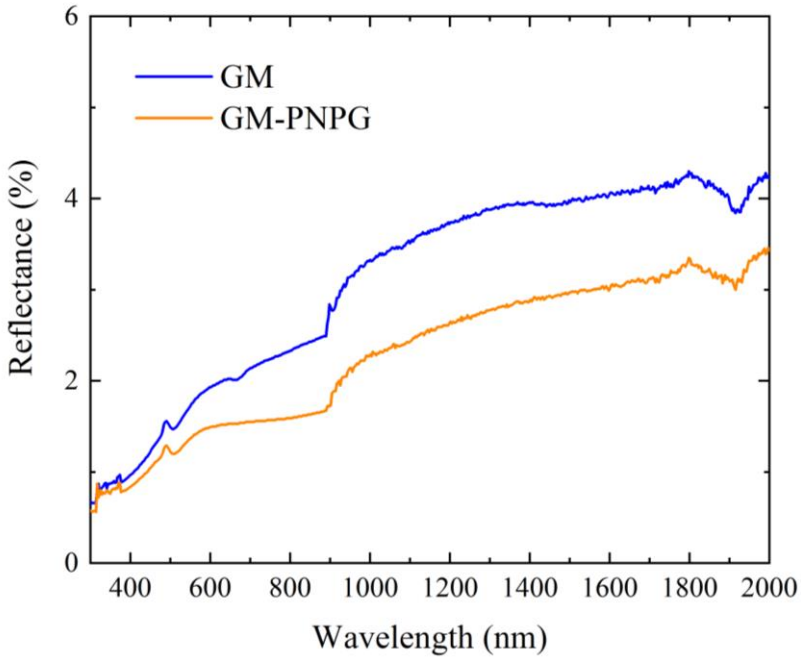

Figure 3.4. Reflectance spectra of pristine GM (blue) and GM-PNPG (gold).

Figure 3.5 highlights the transition of the surface temperature of the pristine GM and GM-PNPG samples in the dried state under the irradiation of 1 sun. The temperature of both samples began to rise rapidly as soon as the irradiation started and attained a plateau after 5 min. The average temperature (600 – 1200 seconds) of the irradiated zone reached equilibrium values of 60.4 °C for the pristine GM and 65.2 °C for GM-PNPG. Yellow/White zone in the infrared images, corresponding to the high temperature area (more than 65 °C), expanded for GM-PNPG compared to the pristine GM. The temperature of the hottest spot on GM-PNPG reached 80.6 °C (indicated by Cursor 1). This difference between the two samples indicates that polymerization of NPG on the GM surface is effective for the absorption of the incident light, which is consistent with the aforementioned reflectance results.

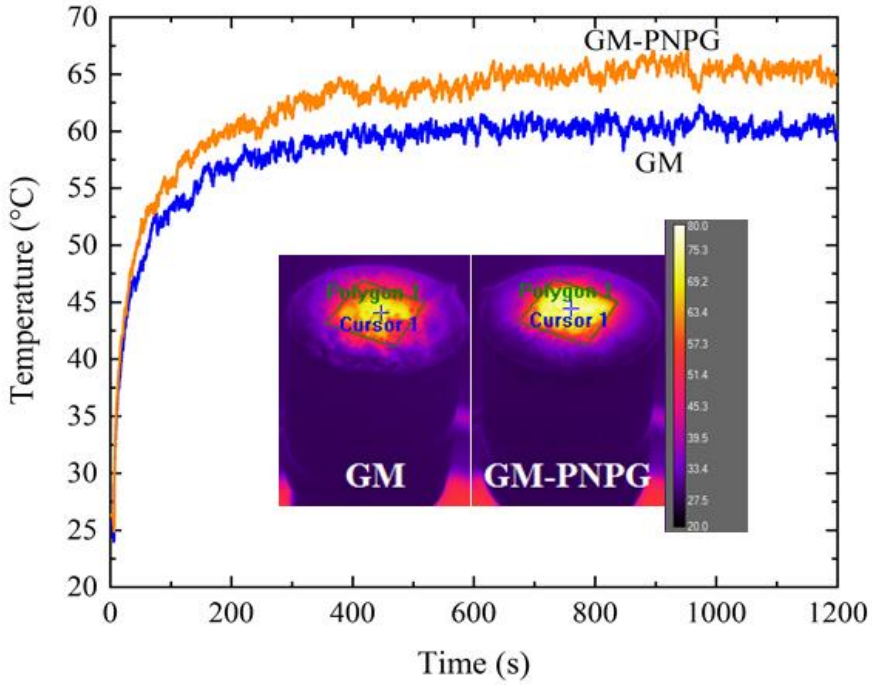

Figure 3.5. Heat profiles of the dried GM and GM-PNPG samples under irradiation of 1 sun.

For the solar-driven interfacial evaporation, the evaporator must be in contact with water. Therefore, the contact angle of a water droplet was examined. **Fig. 3.6** indicates the water droplet behavior on GM and GM-PNPG surfaces over time. For GM, the shape of the droplet could hardly be observed after 30 seconds. On the other hand, the water droplet deposited on the GM-PNPG surface has spread out very quickly, and disappeared after 5 seconds. The same tendency can be confirmed with the contact angle. The contact angle for both samples continued to decrease after the start, and the decrease of water contact angle is accentuated for GM-PNPG. This means that the pristine GM is already hydrophilic and this beneficial feature is well-conserved for GM-PNPG.

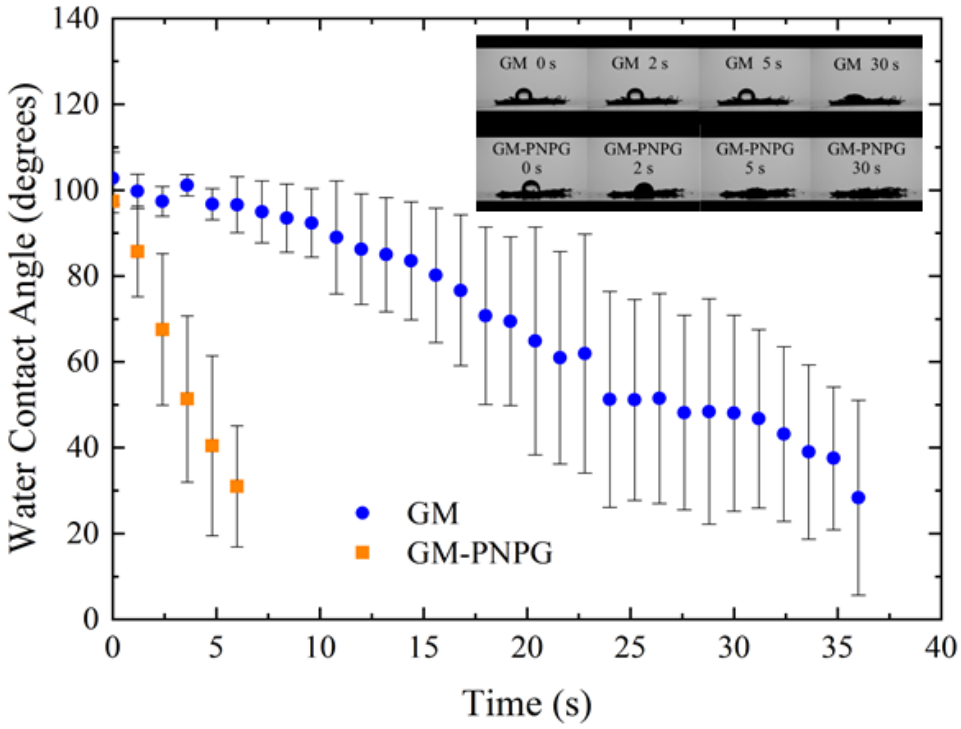

Figure 3.6. Variation of water contact angle over time on GM and GM-PNPG.

Figure 3.7 depicts the FTIR spectra of pristine GM, GM-PNPG, and PNPG. For PNPG, the peak at 3458 cm^{-1} can be attributed to the OH stretching of carboxylic acid. The weak band at 1654 cm^{-1} is due to the stretching of the carbonyl groups. The peak at 1560 cm^{-1} could be assigned to quinone ring deformation [24], while the peak located at 1485 cm^{-1} could be due to the stretching of the benzene ring. The peaks at 1306 and 1244 cm^{-1} are ascribed to C–N and C=N stretchings, respectively. The peak at 1106 cm^{-1} corresponds to the in-plane vibration mode of the quinoid ring [25], whereas the band at 802 cm^{-1} is characteristic of C–H out-of-plane bending vibration mode of the quinoid ring.

For GM, the peak at 3405 cm^{-1} can be attributed to the OH stretching and the C–H stretching peak appeared at 2923 cm^{-1} [26]. Small peaks at 2362 and 2338 cm^{-1} are attributed to the CO_2 in the chamber. Peaks at 1733 cm^{-1} and 1652 cm^{-1} are due to carbonyl groups [27]. Typical aromatic skeletal vibration peak appeared at 1420 cm^{-1}. The peak at 1376 cm^{-1} is due to the phenolic OH and aliphatic C–H. 1316 cm^{-1} can be attributed to the aromatic ring breathing, the peak at 1253 cm^{-1} is caused by C=O stretching, and the peak at 1156 cm^{-1} appeared by aromatic C–H in-plane deformation [28]. C–O deformations of secondary alcohols or esters could be detected at 1059 cm^{-1}. On the other hand, the two samples derived from the green moss (GM and GM-PNPG) exhibit very similar spectra except for the peak at 1507 cm^{-1} of the GM-PNPG,

which could be caused by the C–C stretching in the benzene ring. This is presumably because the PNPG content in the GM-PNPG composite is much smaller compared to the quantity of the GM.

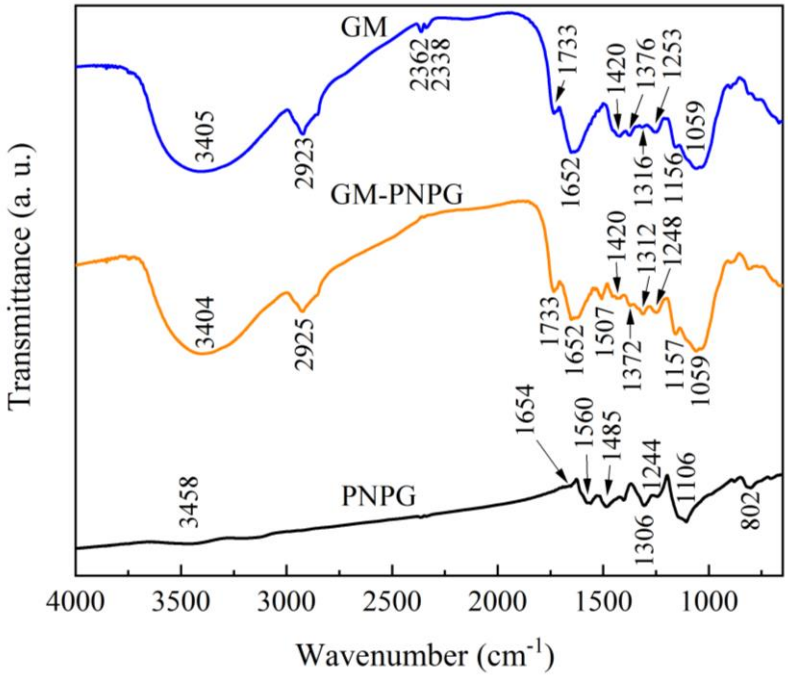

Figure 3.7. FTIR spectra of pristine GM, GM-PNPG and PNPG.

X-ray photoelectron spectroscopy (XPS) was conducted to assess the chemical composition and surface electronic states. **Figure 3.8** displays the low-resolution XPS spectra of pristine GM and GM-PNPG. The XPS plot of GM comprises peaks due to S 2p, C 1s, N 1s and O 1s at respectively 164, 285, 400, 532 eV. For GM-PNPG, peaks can be seen at 170, 285, 400, 533 eV for S 2p, C 1s, N 1s and O 1s, respectively. F 1s peak at 689 eV in GM-PNPG could be due to the contamination brought by the magnetic stirrer.

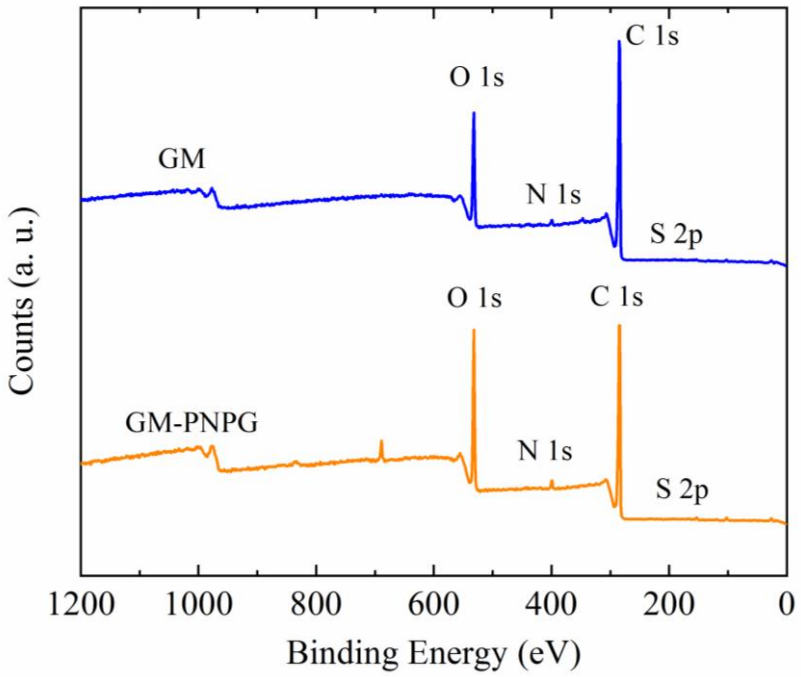

Figure 3.8. Low-resolution XPS spectra of pristine GM and GM-PNPG.

Table 3.1 indicates the atomic composition detected with XPS. The proportion of O depends largely on the moisture quantity in the sample. The ratio C 1s/N 1s slightly decreased in GM-PNPG (C 1s/N 1s = 39.7) compared to that of GM (C 1s/N 1s = 41.7) because of the surface modification with PNPG (C:N:O = 32:4:8) (**Fig. 3.9**).

Table 3.1. Composition of atoms detected with XPS.

	C (at. %)	O (at. %)	N (at. %)	S (at. %)	C/N
GM	67.1	31.0	1.6	0.3	41.7
GM-PNPG	79.2	18.3	2.0	0.4	39.7

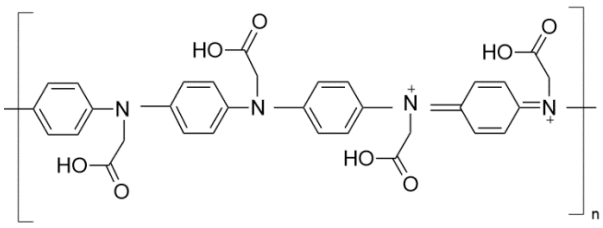

Figure 3.9. Chemical structure of PNPG.

In **Figure 3.10** are displayed the high-resolution spectra of the C 1s peak of GM and GM-PNPG. The curves can be deconvoluted into three distinct components at binding energies of 284.8, 286.3, and 288.7 eV ascribed respectively to C–C, C–O, and COO groups. After PNPG coating on the GM, the intensity of the peak COO increased, which indicates the presence of PNPG, which contains more COO groups than the pristine GM (**Table 3.2**). The increase in the carboxyl groups can be a reason for the aforementioned improvement of hydrophilicity.

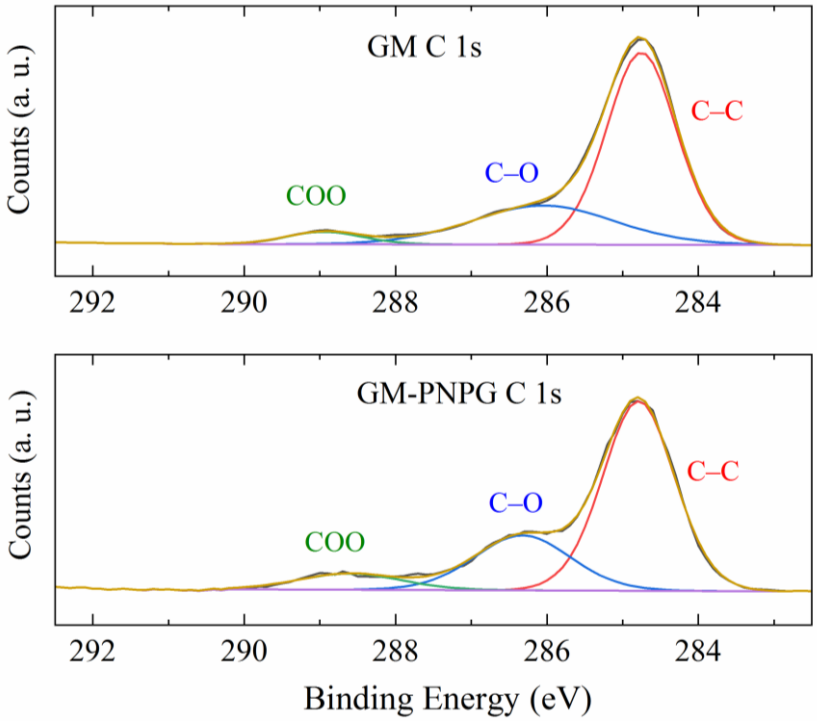

Figure 3.10. High-resolution XPS spectra of the C 1s of the pristine GM and GM-PNPG.

Table 3.2. Proportion of each component in the C 1s peak of GM and GM-PNPG.

	C–C (at. %)	C–O (at. %)	COO (at. %)
GM	67.3	28.0	4.7
GM-PNPG	66.2	25.7	8.1

Figure 3.11 depicts the thermogravimetric (TG) and the first derivative (DTG) curves of pristine PNPG, GM and GM-PNPG. For PNPG, three weight loss stages are evidenced at 125, 280 and 520 °C. These changes could be attributed respectively to water evaporation, the decomposition of the carboxylic groups, and the degradation of PNPG backbones [25]. The thermal behaviors of GM and GM-PNPG are quite similar, and three weight losses could be recognized at 100, 270, and 300 °C. The mass decrease at 100 °C is certainly due to the evaporation of water, while the weight losses at 270 and 300 °C are related to the degradation of organic groups borne by the GM and PNPG. DTG curves for two samples, GM and GM-PNPG are similar except small modifications by PNPG (The degradation of GM-PNPG start at slightly lower temperature compared to the pristine GM) because of overwhelmingly major proportion of green moss.

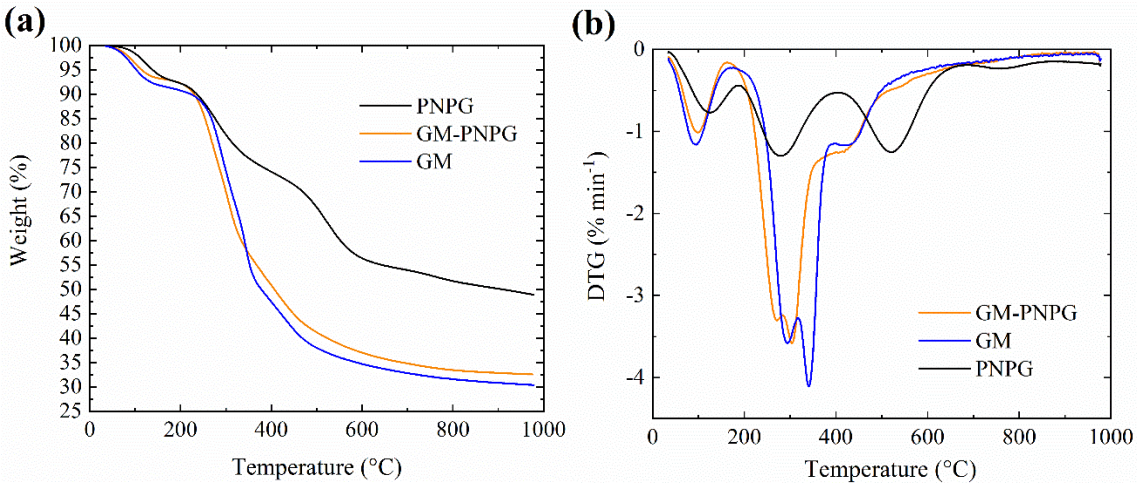

Figure 3.11. TG curves (**a**) and DTG (**b**) curves recorded for PNPG, GM, and GM-PNPG.

3.3.2. Vapor generation performance

Figure 3.12 represents the changes of the water level before and after irradiation with a solar simulator under 1 sun. A glass beaker was used for a better visualization of the inside of the beaker. A decrease of the water level could be noticed after 8 h of irradiation, which means that hydrophilicity of paper towel is capable to pump sufficient water towards the GM-PNPG positioned on the polystyrene foam and that the configuration of this device works properly.

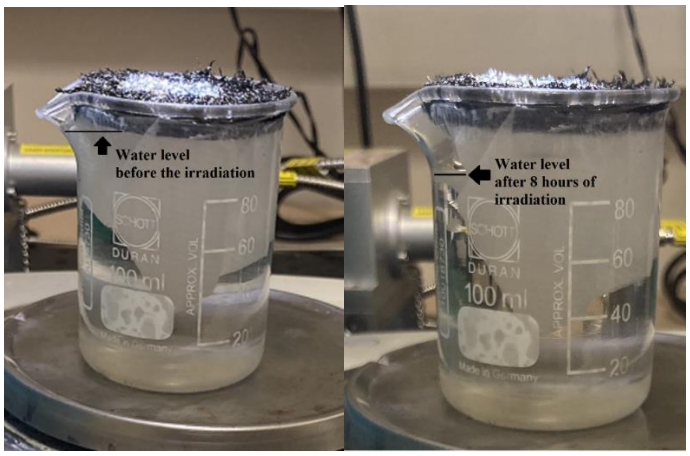

Figure 3.12. Change of water level in the beaker before and after 8 h irradiation (GM-PNPG, 1 sun).

Figure 3.13a exhibits the changes of the mass of the device when using untreated GM, and GM-PNPG. It could be seen that more water was evaporated using the GM-PNPG composite materials than the pristine GM.

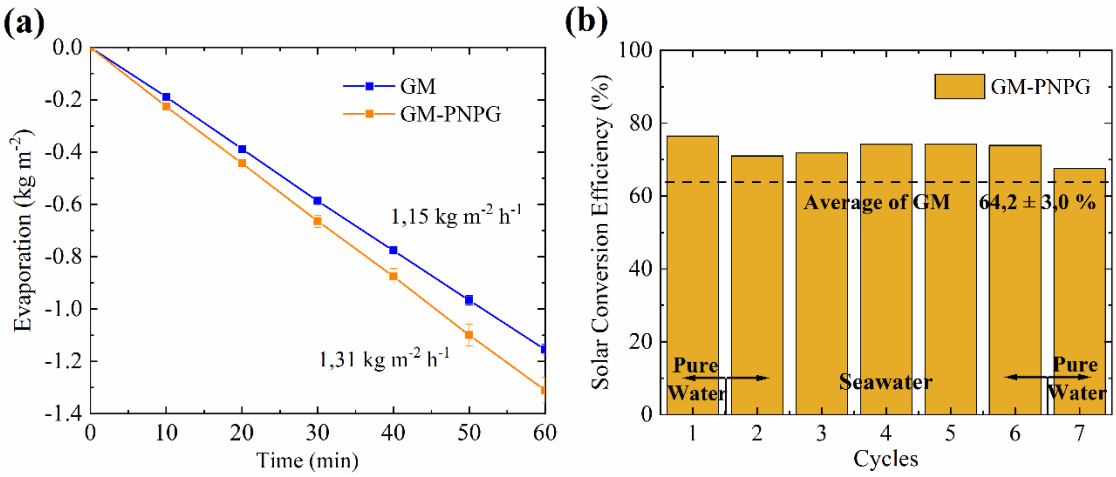

Figure 3.13. (**a**) Evaporation as a function of time under the irradiation of 1 sun. (**b**) Solar conversion efficiency of GM-PNPG samples.

Figure 3.13b summarizes the solar conversion efficiencies through multiple cycles of utilization for the GM-PNPG samples. The solar conversion efficiencies of the GM-PNPG (76.5 ± 3.9%) surpass the level of the untreated GM (64.2 ± 3.0%) even after the sample underwent multiple times of uses for the evaporation of seawater and following repeated drying. This means that the modification of the GM with PNPG represents a good approach to endure the repeated practical uses (**Table 3.3** for comparison with other precedent works).

Table 3.3. Comparison of this work and precedent works (Biomass-based materials)

Material	Evaporation rate (1 sun, kg m^{-2} h^{-1})	Solar Conversion Efficiency (1 sun, %)	Reference
Green moss-poly(*N*-phenylglycine) (GM-PNPG)	1.31 ± 0.05	76.5 ± 3.9	This work
Sweet limes peels-Polyvinyl alcohol sponge	1.386	90.88	29
Lotus leaf-based carbon film	1.30	77.5	13
Polypyrrole-functionalized pomelo peel	1.22	76.61	30
Wood-polypyrrole	1.014	72.5	31
Carbonized Radish-Titanium nitride	1.18	72	32

Evaporation under 0 sun (in absence of light irradiation) varies largely according to the meteorological conditions, such as temperature, and especially humidity, when there is almost no wind like in the laboratory room. For better understanding of the difference among the samples, the evaporation under 0 sun was analyzed. For both samples, there is a strong correlation between the evaporation rate and the humidity of the room (**Figure 3.14**). It is presumably observed that the evaporation is accelerated in a drier meteorological condition. On the other hand, a strong correlation could not be recognized between the evaporation rate and the room temperature within the temperature range of this work (from 19.9 °C to 24.0 °C) (**Fig. 3.15**). This proves that the humidity of the ambient air has a significant effect on the evaporation rate and that the solar conversion efficiency has always to be examined. The evaporation rate for the GM-PNPG composite by 0 sun is the same level compared to that of pristine GM samples. It is inferred from this tendency that PNPG coating on the GM does not affect negatively the hydrophilicity of the sample. This tendency is consistent with the water contact angle measurements.

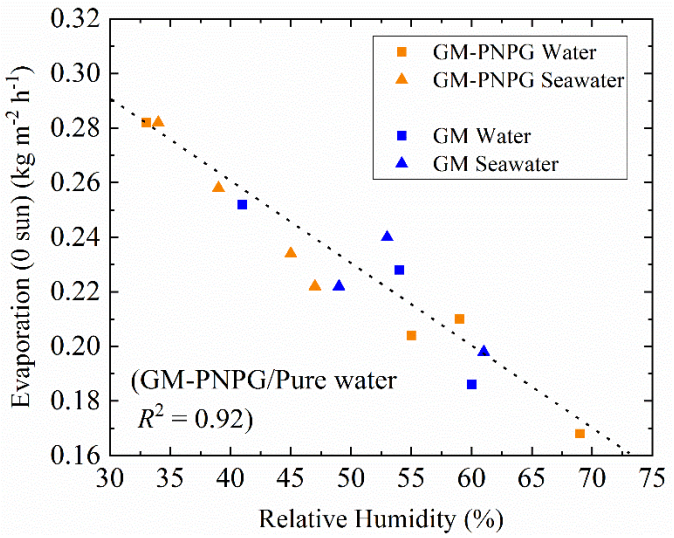

Figure 3.14. Correlation between the atmospheric relative humidity and the evaporation under 0 sun.

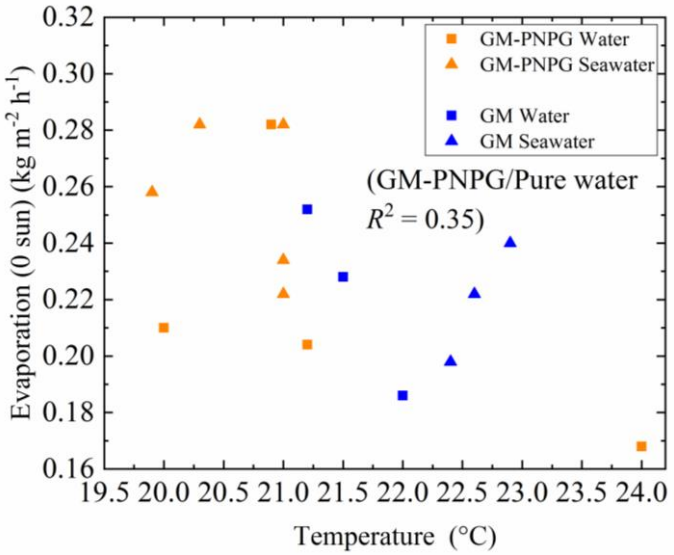

Figure 3.15. Correlation between the evaporation rate (0 sun) and the room temperature.

3.3.3. Purification properties

ICP-OES was employed to determine the concentration of mineral elements of condensed water. **Figure 3.16** presents the concentrations of 5 types of elements (Na, K, Ca, Mg, B) in the initial sea water and in the condensed water collected after 3 h of irradiation under 1 sun. The mineral elements were eliminated by vapor condensation by more than 99%, and the concentrations of those all elements in the condensed water are below the level required or

recommended by the guideline of the World Health Organization (WHO) for drinking water [33].

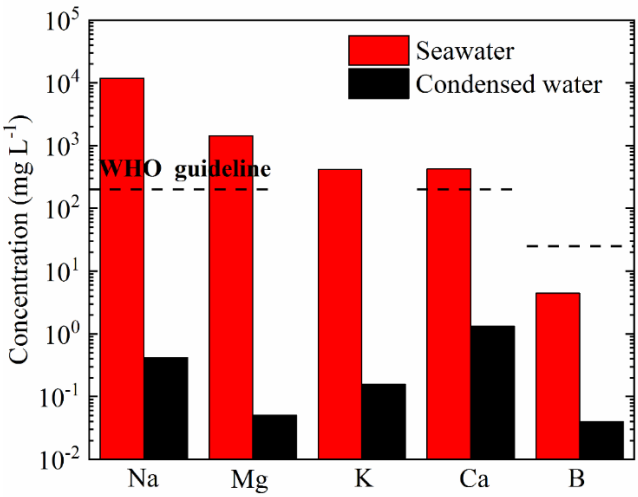

Figure 3.16. Concentration of minerals in the seawater before and after condensation.

The bacterial contamination of drinking water is still a major problem in various countries, because some kinds of bacteria have pathologically harmful effects on human bodies [34-36]. From this perspective, the solar-driven distillation of an *Escherichia coli* (*E. coli*) solution was conducted. After the distillation of the contaminated water (1.3×10^8 CFU *E. coli* / mL), no colonies could be observed on the agar plate which was inoculated by the condensed water (**Figure 3.17**). This means that the condensed water is visibly free from bacterial contamination and that this method is effective under practical conditions for ensuring the security of drinking water.

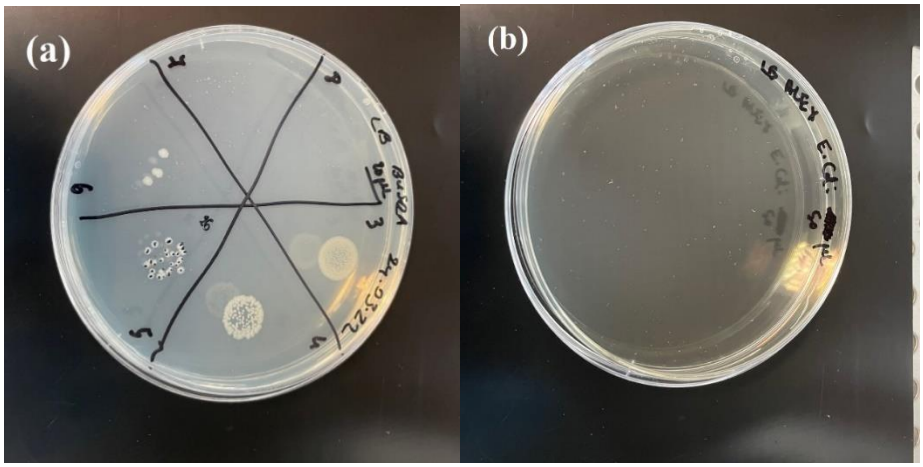

Figure 3.17. Colonies of *E. coli* before (**a**) and after (**b**) the condensation of the contaminated water by *E. coli*.

Taking these results into consideration, it can be concluded that the polymerization of NPG on GM could be an effective method for not only increasing the evaporation rate, but also for producing secured drinking water.

3.4. Conclusion

Polymerization of *N*-phenylglycine (NPG) on the surface of green moss (GM) was investigated with the aim of improving the vapour generation rate for producing safe drinkable freshwater. Thanks to the excellent absorbance and the good adhesion of PNPG on the surface of the GM, the GM-PNPG hybrid material turned out to be a good candidate for solar-driven interfacial evaporation under practical conditions. The GM-PNPG samples showed enhanced evaporation rate by 0.16 kg m^{-2} h^{-1} and the solar conversion efficiency was improved to 76.5% as compared to 64.2% of the pristine GM. Moreover, the excellent accessibility of the GM, the low toxicity of the synthesized material, and the simplicity of fabrication are all beneficial for the design of efficient and low-cost water evaporator systems.

Water desalination using the GM-PNPG allowed to decrease the concentrations of five common elements (Na, K, Ca, Mg, B) in the distilled water to values much lower than those recommended by the WHO for safe drinking water. In addition, the GM-PNPG was effective in bacteria removal from water contaminated with *E. coli*. Taken together, all these attributes are favorable factors for practical prospects in the fields of wastewater treatment and seawater desalination.

References

[1] M.T.H. van Vliet, E.R. Jones, M. Florke, W.H.P. Franssen, N. Hanasaki, Y. Wada, J.R. Yearsley, Global water scarcity including surface water quality and expansions of clean water technologies, Environmental Research Letters 16 (2021) 024020.

[2] R.J. Petersen, Composite reverse osmosis and nanofiltration membranes, Journal of Membrane Science 83 (1993) 81.

[3] J.P. Chen, L.K. Wang, L. Yang, Y.M. Zheng, Desalination of Seawater by Thermal Distillation and Electrodialysis Technologies, Membrane and Desalination Technologies 13 (2010) 525.

[4] Peter H. Gleick, Water in Crisis: A Guide to the World's Fresh Water Resources, Oxford University Press, New York. p13 (1993).

[5] Z. Wang, Y. Liu, P. Tao, Q. Shen, N. Yi, F. Zhang, Q. Liu, C. Song, D. Zhang, W. Shang, T. Deng, Bio-Inspired Evaporation Through Plasmonic Film of Nanoparticles at the Air–Water Interface, Small 10 (2014) 3234.

[6] UN World Water Development Report 2021 (available at : https://www.unwater.org/publications/un-world-water-development-report-2021/)

[7] J. Wang, Y. Li, L. Deng, N. Wei, Y. Weng, S. Dong, D. Qi, J. Qiu, X. Chen, T. Wu, High-Performance Photothermal Conversion of Narrow-Bandgap Ti_2O_3 Nanoparticles, Advanced Materials 29 (2017) 1603730.

[8] I. Zada, W. Zhang, P. Sun, M. Imtiaz, N. Iqbal, U. Ghani, R. Naz, Y. Zhang, Y. Li, J. Gu, Q. Liu, D. Pantelic, B. Jelenkovic, D. Zhang, Superior photothermal black TiO_2 with random size distribution as flexible film for efficient solar steam generation, Applied Materials Today 20 (2020) 100669.

[9] M.Q. Yang, C.F. Tan, W. Lu, K. Zeng, G.W. Ho, Spectrum tailored defective 2D semiconductor nanosheets aerogel for full-spectrum-driven photothermal water evaporation and photochemical degradation, Advanced Functional Materials 30 (2020) 2004460.

[10] L. Zhou, Y. Tan, D. Ji, B. Zhu, P. Zhang, J. Xu, Q. Gan, Z. Yu, J. Zhu, Self-assembly of Highly Efficient, Broadband Plasmonic Absorbers for Solar Steam Generation, Science Advances 2 (2016) e1501227.

[11] M. Gao, C.K. Peh, H.T. Phan, L. Zhu, G.W. Ho, Solar absorber gel: localized macro-nano heat channeling for efficient plasmonic Au nanoflowers photothermic vaporization and triboelectric generation, Advanced Energy Materials 8 (2018) 1800711.

[12] L. Wang, G. Zhu, M. Wang, W. Yu, J. Zeng, X. Yu, H. Xie, Q. Li, Dual plasmonic Au/TiN nanofluids for efficient solar photothermal conversion, Solar Energy 184 (2019) 240.

[13] M.X. Guo, J.B. Wu, F.H. Li, Q.Q. Guo, H.L. Fan, H.M. Zhao, A low-cost lotus leaf-based carbon film for solar-driven steam generation, New Carbon Materials 35 (2020) 436.

[14] J.Y. Li, X. Zhou, J.Y. Zhang, C. Liu, F. Wang, Y.T. Zhao, H.X. Sun, Z.Q. Zhu, W.D. Liang, A. Li, Migration Crystallization Device Based on Biomass Photothermal Materials for Efficient Salt-Rejection Solar Steam Generation, ACS Applied Energy Materials 3 (2020) 3024.

[15] M.X. Guo, J.B. Wu, F.H. Li, Q.Q. Guo, H.L. Fan, H.M. Zhao, A low-cost lotus leaf-based carbon film for solar-driven steam generation, New Carbon Materials 35 (2020) 436.

[16] L.B. Zhang, B. Tang, J.B. Wu, R.Y. Li, P. Wang, Hydrophobic light-to-heat conversion membranes with self-healing ability for interfacial solar heating, Advanced Materials 27 (2015) 4889.

[17] F. Zhao, X.Y. Zhou, Y. Shi, X. Qian, M. Alexander, X.P. Zhao, S. Mendez, R.G. Yang, L.T. Qu, G.H. Yu, Highly efficient solar vapour generation via hierarchically nanostructured gels, Nature Nanotechnology 13 (2018) 489.

[18] X.Y. Zhou, F. Zhao, Y.H. Guo, B. Rosenberger, G.H. Yu, Architecting highly hydratable polymer networks to tune the water state for solar water purification, Science Advances 5 (2019) eaaw5484.

[19] M. Khajevand, S. Azizian, R. Boukherroub, Naturally abundant green moss for highly efficient solar thermal generation of clean water, ACS Applied Materials & Interfaces 13 (2021) 31680.

[20] B.P. Jiang, L. Zhang, X.L. Guo, X.C. Shen, Y. Wang, Y. Zhu, H. Liang, Poly(N-phenylglycine)-Based Nanoparticles as Highly Effective and Targeted Near-Infrared Photothermal Therapy/Photodynamic Therapeutic Agents for Malignant Melanoma, Small 13 (2017) 1602496.

[21] S. Ghayyem, A. Barras, F. Faridbod, S. Szunerits, R. Boukherroub, Effective PDT/PTT dual-modal phototherapeutic killing of bacteria by using poly(N-phenylglycine) nanoparticles, Microchimica Acta 189 (2022) 150.

[22] M. Li, Y.Y. Luo, C. Jia, M.M. Huang, M.Z. Yu, G.X. Luo, L.B. Zhao, R. Boukherroub, Z.D. Jiang, Au-assisted polymerization of conductive poly(N-phenylglycine) as high-performance positive electrodes for asymmetric supercapacitors, Nanotechnology 33 (2022) 045602.

[23] V.K.A. Muniraj, R. Boukherroub, M.V. Shelke, Flexible Energy Storage Device Based on Poly(N-phenylglycine), an Incentive-Energy Pseudocapacitive Conducting Polymer, and

Electrochemically Exfoliated Graphite Sheets, ACS Sustainable Chemistry & Engineering 8 (2020) 6433.

[24] X.P. Lei, Z.X. Su, Novel conducting polyaniline copolymers of aniline and N-phenylglycine, Materials Letters 61 (2007) 1158.

[25] S. Ghayyem, A. Swaidan, A. Barras, M. Dolci, F. Faridbod, S. Szunerits, R. Boukherroub,

Colorimetric detection of chromium (VI) ion using poly(N-phenylglycine) nanoparticles acting as a peroxidase mimetic catalyst, Talanta 226 (2021) 122082.

[26] T. Rashid, C.F. Kait, T. Murugesan, A "Fourier Transformed Infrared" Compound Study of Lignin Recovered from a Formic Acid Process, Procedia Engineering 148 (2016) 1312.

[27] H.M. Wang, Z. Liu, L.F. Hui, L. Ma, X. Zheng, J.Z. Li, Y. Zhang, Understanding the structural changes of lignin in poplar following steam explosion pretreatment, Holzforschung 74 (2020) 275.

[28] S. Gao, J. Zhao, X. Wang, Y.Z. Guo, Y. Han, J.H. Zhou, Lignin Structure and Solvent Effects on the Selective Removal of Condensed Units and Enrichment of S-Type Lignin, Polymers 10 (2018) 967.

[29] H.M. Wilson, D.J. Ahirrao, S.R. Ar, N. Jha, Biomass-derived porous carbon for excellent low intensity solar steam generation and seawater desalination, Solar Energy Materials and Solar Cells 215 (2020) 110604.

[30] C. Zhang, X. Peng, N. Feng, L.K. Yan, Q.Q. Liu, D. Zhang, J.C. Gu, W.Q. Wang, T. Chen, Converting Pomelo Peel into Eco-friendly and Low-Consumption Photothermic Biomass

Sponge toward Multifunctioal Solar-to-Heat Conversion, ACS Sustainable Chemistry & Engineering, 8 (2020) 5328.

[31] Z. Wang, Y.T. Yan, X.P. Shen, C.D. Jin, Q.F. Sun, H.Q. Li, A wood–polypyrrole composite as a photothermal conversion device for solar evaporation enhancement, Journal of Materials Chemistry A, 7 (2019) 20706.

[32] X.Y. Wang, C.C. Sha, W.J. Wang, Y.C. Chen, Y.H. Yu, D.S. Fan, Functionalized biomass-derived composites for solar vapor generation, Materials Research Express 6 (2019) 125613.

[33] Guidelines for Drinking-water Quality, 4th edition, incorporating the 1st addendum, World Health Organization (2011) (available at: https://www.who.int/publications/i/item/9789241549950)

[34] J. Passerat, N.K. Ouattara, J.M. Mouchel, V. Rocher, P. Servais, Impact of an intense combined sewer overflow event on the microbiological water quality of the Seine River, Water Research 45 (2011) 893.

[35] G.J. Wilbers, M. Becker, L.T. Nga, Z. Sebesvari, F.G. Renaud, Spatial and temporal variability of surface water pollution in the Mekong Delta, Vietnam, Science of the Total Environment 485 (2014) 653.

[36] J.P. Nataro, J.B. Kaper, Diarrheagenic Escherichia coli, Clinical Microbiology Reviews 11 (1998) 142.

Chapter 4: Green moss - Petroleum coke

4.1. Introduction

The accessibility of raw materials, the cost and the complexity of the synthesis are major obstacles for spreading the solar-driven interfacial evaporation, because this technique is desirable especially in geographically remote, and infrastructure-poor areas. Therefore, it is necessary to utilize photothermal materials which are very accessible or derived from cheap and available raw materials.

On the one hand, green moss (GM) is a plant found in almost all climatic conditions thanks to its very simple structure, and it has already been reported that GM is a good candidate for solar interfacial evaporation, because of its hydrophilicity and excellent photothermal conversion [1].

On the other hand, petroleum coke is a by-product of the oil refining processes. In petroleum refining processes, crude oil undergoes cracking (decomposition of large hydrocarbons) to extract valuable products composed of short-chain hydrocarbons. As a result, petroleum coke is produced as a by-product and a large amount of petroleum coke is stockpiled [2]. Some researchers suggest that petroleum coke consists mainly of a large number of aromatic rings, just like graphite, as well as some impurities (O, N, S and metals) [3][4]. Therefore, one could expect that the petroleum coke features photothermal properties comparable to that of commercial carbon-based materials such as reduced graphene oxide (rGO) [5-7].

In this chapter, we combined the good hydrophilic and photothermal properties of natural and abundant green moss with good photothermal behavior of petroleum coke to generate a composite material with improved vapor generation. The synthesis technique is straightforward and consists in a simple immersion of washed green moss in the petroleum coke suspension and subsequent drying.

4.2. Experimental section

4.2.1. Processing of the green moss (GM)

Once the green moss (GM) was collected, it was washed with water to remove fine sand, mud, and plastic. Then, it was dried in an oven at 60 °C overnight. Subsequently, the GM was soaked in ethanol for approximately 7 h in order to dissolve organic components and finally dried at 60 °C for 2 h.

4.2.2. Preparation of green moss - petroleum coke (GM-PetCoke) composite

As a first step, the petroleum coke suspension was prepared by adding the petroleum coke (250 mg) into a mixture of 15 mL of water and 6 mL of ethanol. This suspension was placed in an ultrasonic bath for 5 min to homogenize the suspension. Then, the washed green moss (600 mg) was added to this suspension, and this mixture was left on a tube revolver rotator (10 rpm) for 16 h for sufficient impregnation. Finally, the green moss was retrieved for 16 h of drying at 60 °C, and this product is called GM-PetCoke here. **Figure 4.1** shows photos of pristine GM and GM-PetCoke; a color change from dark brown to black was observed after the addition of the petroleum coke.

Figure 4.1. Photos of pristine GM and GM-PetCoke.

4.3. Results and discussion

4.3.1. Characterization of the petroleum coke

Figure 4.2a and **c** are the SEM (lower electron detector (LED), which is a secondary electron detector) images of the petroleum coke powder. In this mode, the secondary electrons were captured, which helps to understand the morphology. **Figure 4.2b** and **d** are the SEM (backscattered electron detector (BED-C)) images of the petroleum coke powder for the same spot as **Figure 4.2a** and **c**, respectively. Using the BED-C mode, back-scattered electrons were observed and heavy elements can be seen as white spots.

The size of the petroleum coke particles ranges from 1 to 20 µm. White spots could be seen randomly, which implies that heavier elements than carbon exist in the petroleum coke sample.

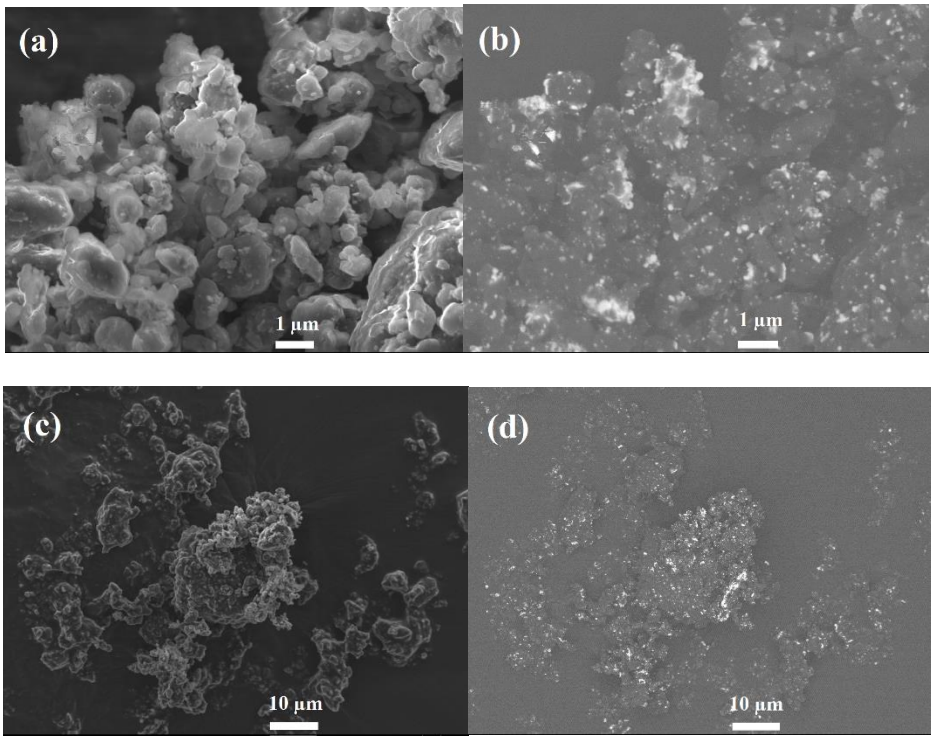

Figure 4.2. SEM images of the petroleum coke powder (**(a)** and **(c)**: LED mode, **(b)** and **(d)**: BED-C mode).

Elemental analysis of the petroleum coke powder by energy dispersive X-ray (EDX) spectroscopy showed that the petroleum coke consists essentially of C along with minor contributions of non-carbon impurities, such as O, Pb and S (**Fig. 4.3**).

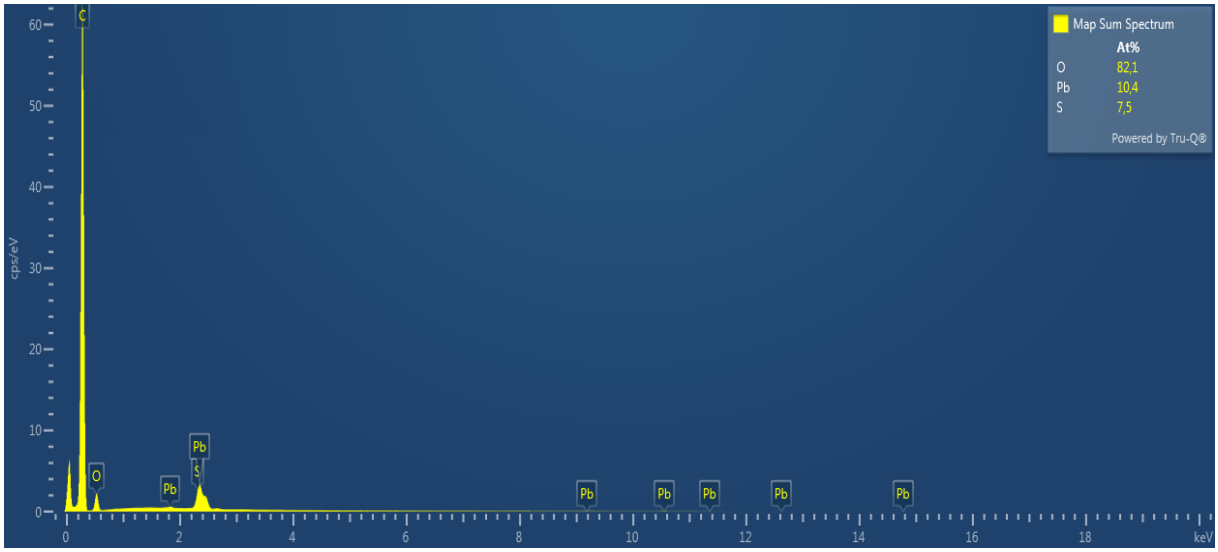

Figure 4.3. EDX spectrum of the petroleum coke powder.

The existence of Pb was confirmed by X-ray diffraction (XRD) analysis: Pb (PDF 65-2873), PbO (PDF 78-1666) and $Pb_3B_3O_8(OH)_3 \bullet H_2O$ (Lead borate hydroxide hydrate, PDF 52-1259) were detected as crystalline phases (**Fig. 4.4**).

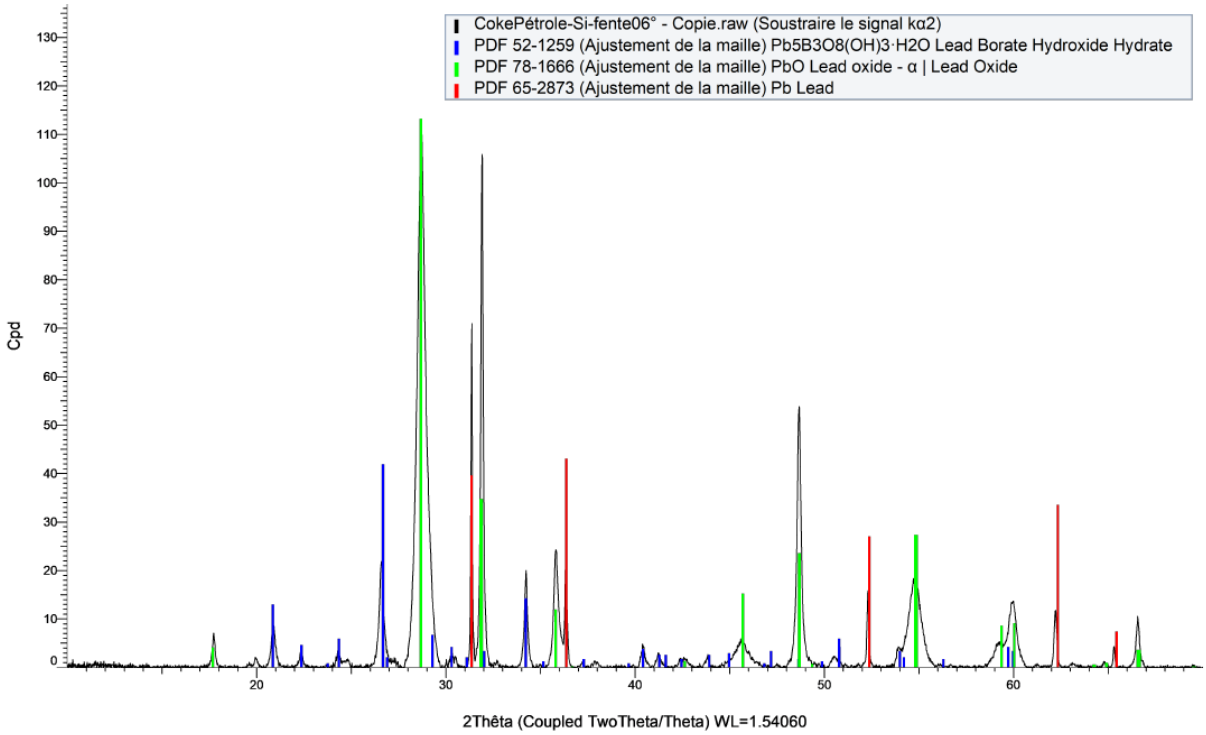

Figure 4.4. XRD pattern of the petroleum coke powder.

Figure 4.5 depicts the X-ray photoelectron spectroscopy (XPS) plots of the petroleum coke. In the XPS large scan in **Fig. 4.5a**, several peaks are evidenced at 138 eV (Pb 4f), 164 eV (S 2p), 284 eV (C 1s), 399 eV (N 1s), and 532 eV (O 1s). Three other lead peaks can be confirmed at 413 eV (Pb $4d_{5/2}$), 435 eV (Pb $4d_{3/2}$) and 645 eV (Pb $4p_{3/2}$). The atomic concentrations of C, O, S, Pb, and N were respectively 90.0, 4.9, 2.6, 1.6 and 0.9 at.% (**Table 4.1**). The results corroborate the EDX data, indicating that C is the major component of the petroleum coke.

Figure 4.5b displays the high-resolution of the C 1s XPS spectrum of the petroleum coke. It can be deconvoluted into three components, C–C/C=C (284.7 eV), C–N/C–S (285.3 eV), C–O (286.1 eV).

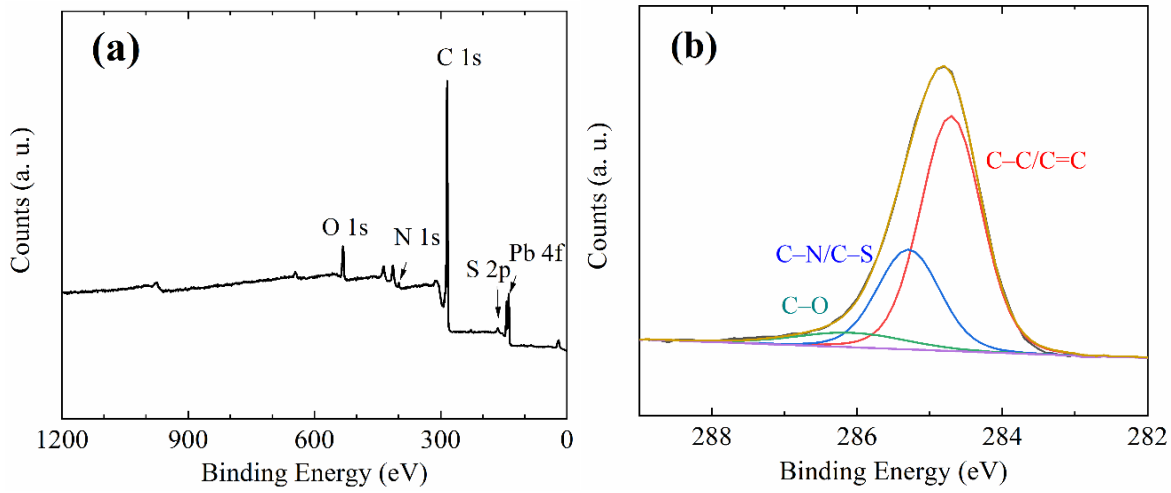

Figure 4.5. **(a)** Low-resolution, and **(b)** C 1s high-resolution XPS spectra of the petroleum coke powder.

Table 4.1. Atomic percentages of the different elements of the petroleum coke.

Element	C	O	S	Pb	N
Atomic %	90.0	4.9	2.6	1.6	0.9

High-resolution XPS spectra of other elements are shown in **Figure 4.6**. O 1s peak can be deconvoluted into C=O (532.1 eV) and C–O (534.1 eV). N 1s peak can be separated according to the two different nitrogen positions, pyridinic (398.5 eV) and graphitic (400.3 eV). S 2p peak can be interpreted as the sum of 6 components (S–Pb (160.2 and 162.5 eV), S–C (164.0 and 165.2 eV), and SO_3^{2-} (166.2 and 168.4 eV)). Pb 4f peak is the sum of 4 components (Pb^0 (137.6 and 142.4 eV) and Pb^{2+} (138.9 and 143.7 eV)).

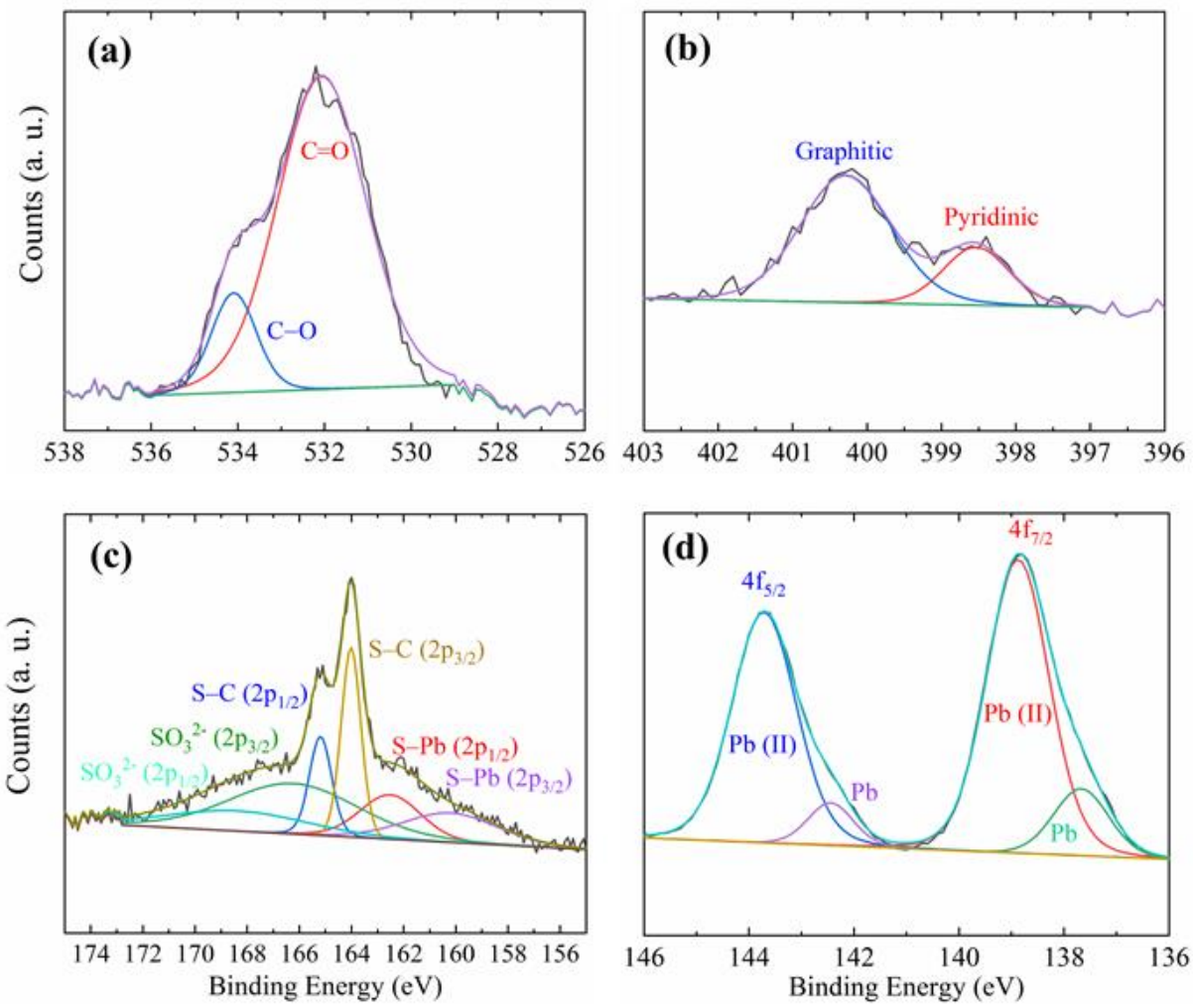

Figure 4.6. High-resolution XPS spectra of the **(a)** O 1s, **(b)** N 1s, **(c)** S 2p, **(d)** Pb 4f of the petroleum coke powder.

Figure 4.7 shows the Raman spectrum of petroleum coke, consisting of two main peaks at 1367 and 1600 cm^{-1} assigned to the D- and G-bands, respectively, typically found in graphitic-based materials. The G-band at 1600 cm^{-1} is commonly ascribed to the C=C stretching peak in graphite-like sp^2 aromatic ring, while the D band at 1367 cm^{-1} is due to defects in the graphite-like structures. From these analyses and the results of the literature [3][4], it could be assumed that petroleum coke is mainly composed of carbon (especially aromatic components) along with S, O heteroatoms, and lead-derived compounds (Pb and PbO, etc.).

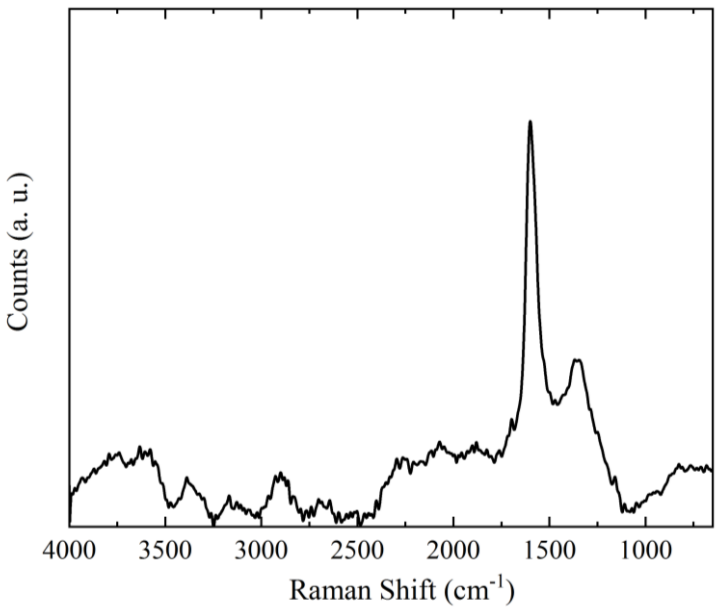

Figure 4.7. Raman spectrum of the petroleum coke powder.

4.3.2. Characterization of the green moss - petroleum coke (GM-PetCoke) composite

Figure 4.8 is the low-resolution XPS spectra of the green moss (GM) and GM-PetCoke samples. In GM, C 1s (285 eV), N 1s (400 eV) and O 1s (532 eV) were evidenced. After the addition of the petroleum coke, Pb 4f (139 and 144 eV) peak could be seen as well as C 1s (285 eV), N 1s (400 eV) and O 1s (533 eV) peaks. **Table 4.2** summarizes the atomic percentages of different elements in GM and GM-PetCoke, as determined from the low-resolution XPS spectra. Pb and S were detected on GM-PetCoke as well as C, O, N, and these elements are derived from the petroleum coke. **Figure 4.9** displays the high-resolution XPS C 1s spectra of GM and GM-PetCoke, and a slight increase of COO peak was observed in GM-PetCoke, whose reason is unknown (**Table 4.3**).

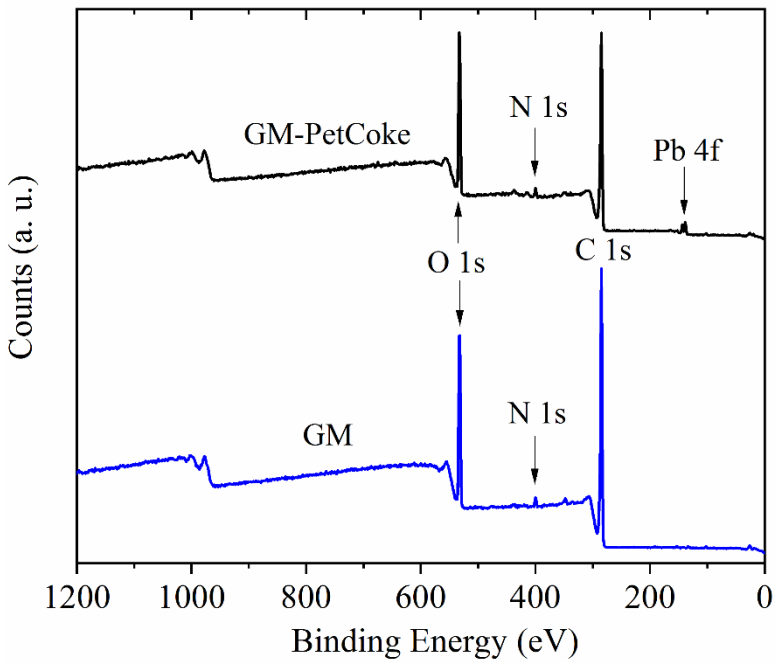

Figure 4.8. Low-resolution XPS spectra of GM and GM-PetCoke.

Table 4.2. Atomic percentages of the different elements of GM and GM-PetCoke.

Element	C	O	S	Pb	N
GM (at. %)	81.6	17.2	-	-	1.2
GM-PetCoke (at. %)	79.1	18.5	0.9	0.3	1.1

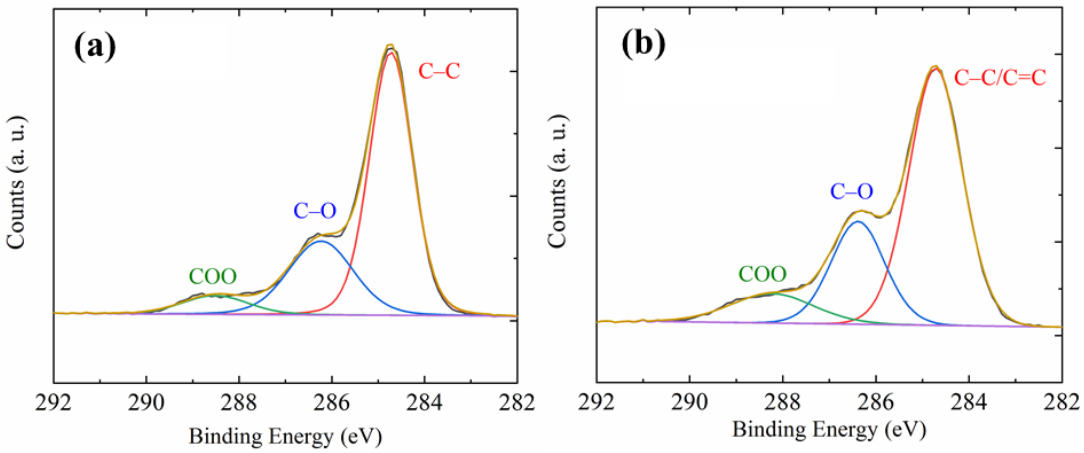

Figure 4.9. High-resolution C 1s XPS spectre of (**a**) GM and (**b**) GM-PetCoke.

Table 4.3. Contribution of different components in C 1s peak of GM and GM-PetCoke.

Element	C–C	C–O	COO
GM (at. %)	65.3	27.5	7.2
GM-PetCoke (at. %)	63.3	25.4	11.3

Figure 4.10a-c are the scanning electron microscopy (SEM) images of GM, petroleum coke powder and GM-PetCoke samples. **Figure 4.10a** is an image of the pristine GM, revealing a smooth surface with an inherent ordered pattern. In **Figure 4.10b,** the morphology of the petroleum coke powder obviously revealed particles with non-uniform size distribution; their particle size ranges from 1 to 10 μm. The SEM image of GM-PetCoke indicates that petroleum coke particles are homogeneously coated and distributed on the GM surface, and the surface pattern was no longer observed (**Fig. 4.10c**).

Figure 4.10d is a back-scattered electron detector SEM image of the GM-PetCoke. With this detector, heavy elements can be seen as white spots. Therefore, this photo implies that heavy elements exist on the surface of GM-PetCoke. **Figure 4.10e** and **f** are chemical mappings of Pb and S on the GM-PetCoke surface, respectively. Pb and S were detected all over the surface, indicating that the petroleum coke coated homogeneously the GM surface, because XPS unveiled that pristine GM contains only C, O and N.

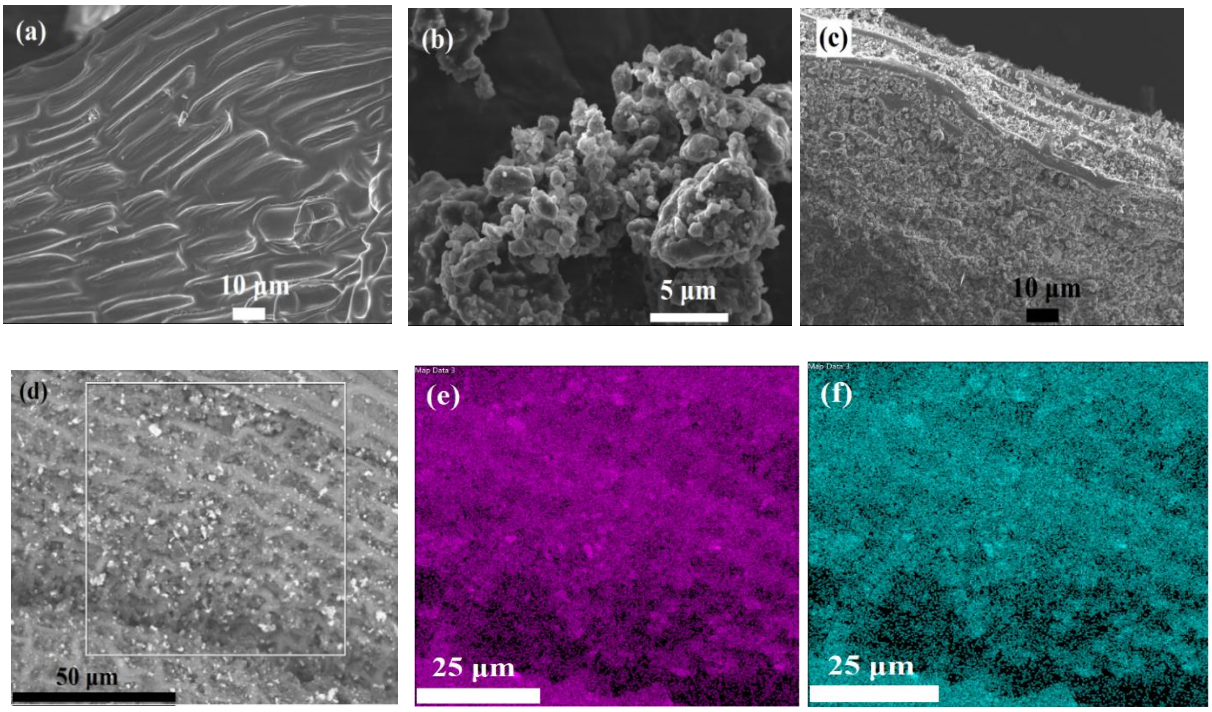

Figure 4.10. SEM images (secondary electron image) of the (**a**) pristine GM, (**b**) petroleum coke and (**c**) GM-PetCoke, (**d**) Area of chemical mapping analysis of (**e**) Pb and (**f**) S distribution of GM-PetCoke.

Figure 4.11 presents the reflectance spectra of the GM and GM-PetCoke samples. The pristine GM exhibits a low reflectance (≤ 4%) throughout the wavelength range (300-2000 nm) investigated. Interestingly, the GM-PetCoke shows slightly lower reflectance than GM for the whole wavelength range studied (300-2000 nm). This demonstrates that the addition of the petroleum coke is effective in absorbing solar radiation.

To assess whether the increased absorption of sunlight causes the sample to generate heat, the dry temperature was measured under an irradiation of 1 sun (**Fig. 4.11b**). Regarding the temperature, the GM-PetCoke composite recorded higher value (average temperature of irradiated area between 600 and 1200 s = 68 °C) while the irradiated area temperature of pristine GM reached only to 60 °C. The temperature of the petroleum coke reached 67 °C, which is nearly the same value of GM-PetCoke. The inset of the **Fig. 4.11b** displays thermal camera images of dried-state GM and GM-PetCoke under 1-sun irradiation. The yellow/white colors correspond to the area where the temperature is above 65 °C, and this area has expanded in GM-PetCoke compared to the pristine GM. This difference proves that the petroleum coke loaded onto the surface of the GM is able to generate heat when irradiated by sunlight.

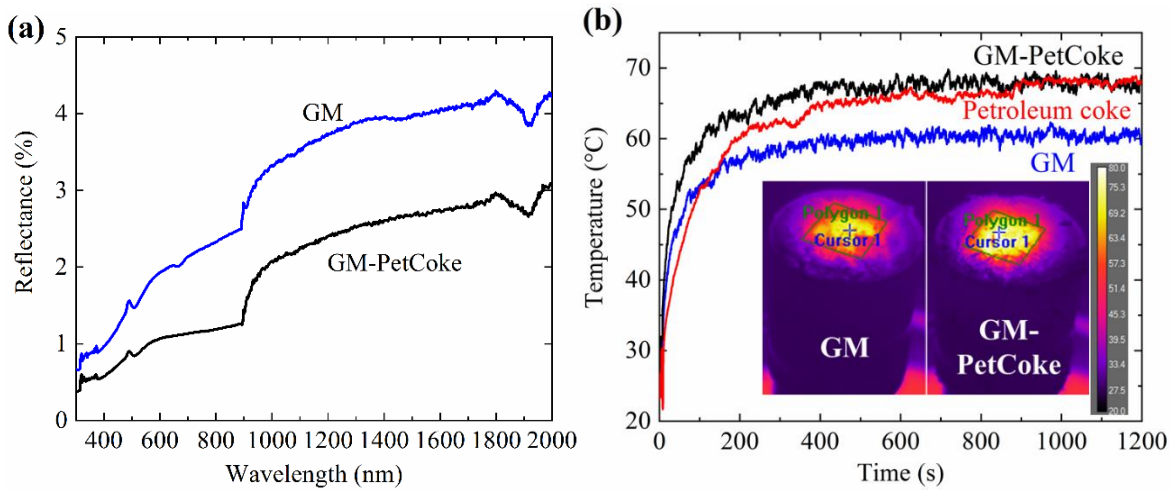

Figure 4.11. **(a)** UV-vis/NIR reflectance spectra of GM and GM-PetCoke, **(b)** Average temperature of 1-sun irradiated area and thermal camera images of dried-state GM and GM-PetCoke.

Figure 4.12 shows the contact angle transitions for GM and GM-PetCoke samples. For GM, the contact angle decreases as a function of time, and reached 30° after 30 s. However, the addition of the petroleum coke had a negative effect on the wetting behavior. Although the contact angle decreases with time, it remains around 70° even after 200 s. This is almost the same value as the petroleum coke (65° after 200 s, **Fig. 4.13**)

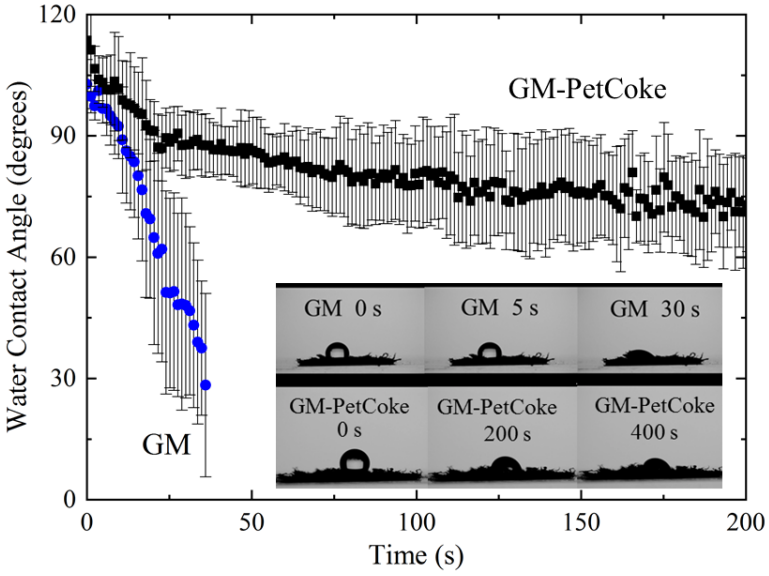

Figure 4.12. Contact angle transition for GM and GM-PetCoke samples.

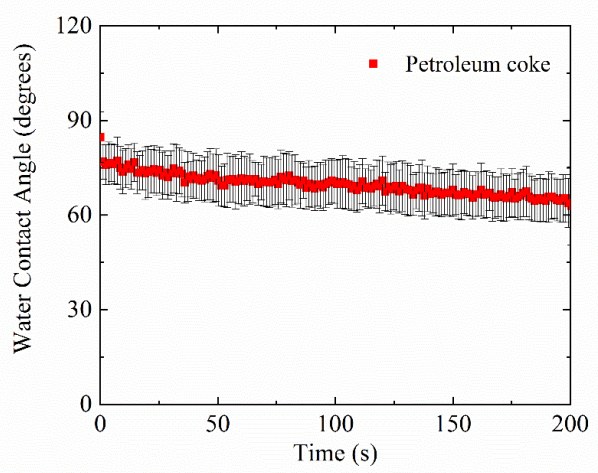

Figure 4.13. Water contact angle of the petroleum coke.

The FTIR spectra of the GM and GM-PetCoke samples are presented in **Figure 4.14**. For the petroleum coke powder, 4 peaks can be observed at 1635, 1437, 876, and 749 cm^{-1}. The band at 1635 cm^{-1} is attributed to the stretching of the C=C bond, while the peak at 1437 cm^{-1} is caused by the shear motion of CH_2 [8]. An out-of-plane C–H vibration in aromatic moieties appears at 876 and 749 cm^{-1} [9]. Lack of hydrophilic functional groups (–COO–, –OH) in the petroleum coke could lead to the decrease of wettability on the GM-PetCoke.

Between GM and GM-PetCoke FTIR spectra, there is not much difference in peak position. This may be due to a small amount of petroleum coke loaded on the GM or to overlapping peaks between the two. And the addition of the petroleum coke does not bring about any chemical change of the GM.

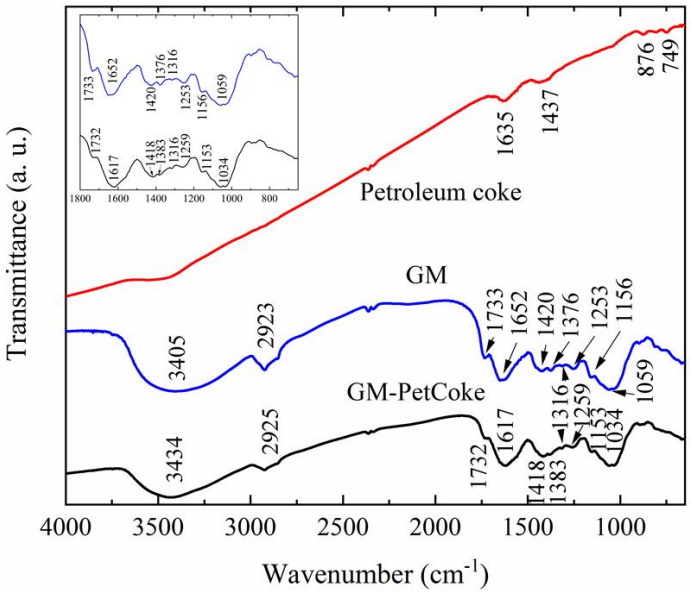

Figure 4.14. Transmission FTIR spectra of GM, petroleum coke and GM-PetCoke.

Figure 4.15 are the thermogravimetric (TG) and derivative thermogravimetric (DTG) curves of the petroleum coke, GM and GM-PetCoke. In **Figure 4.15a**, 87.4% of the mass persisted even at 910 °C for the petroleum coke, indicating its good stability even at high temperatures. This contrasts with the low thermal stability of GM-PetCoke (38.3% at 910 °C) and GM alone (23.1% at 910 °C).

In **Figure 4.15b**, by comparing the DTG plots of GM and GM-PetCoke, there is not much difference in the position (temperature) of the peaks before and after the addition of petroleum coke. For the petroleum coke powder, three peaks are obvious at 320, 490 and 620 °C in the DTG curve. The first peak at 320 °C is due to volatile substances, while the second peak at 490 °C and the third peak at 620 °C are ascribed to carbon and hydrogen losses during pyrolysis [10].

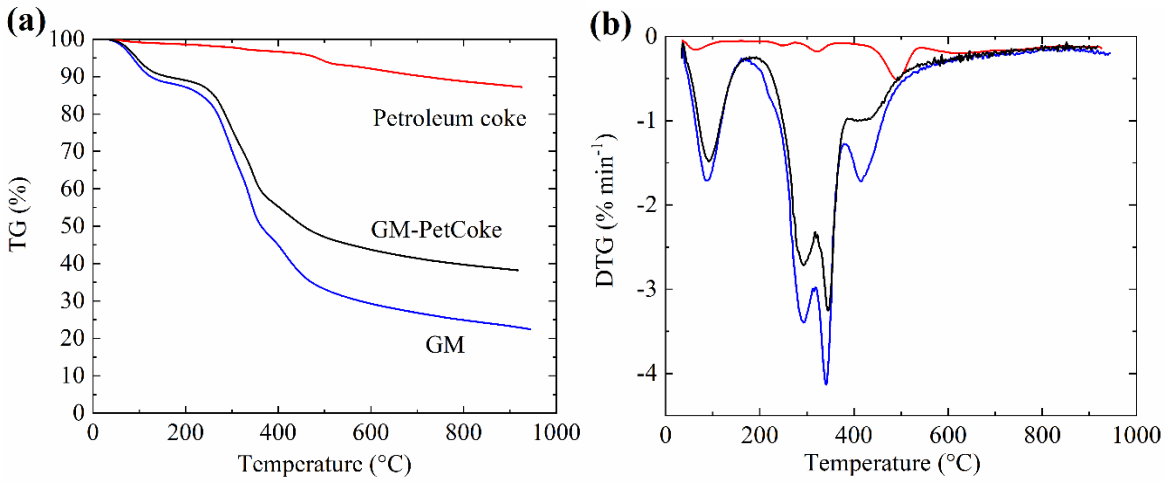

Figure 4.15. **(a)** TG and **(b)** DTG curves of the petroleum coke, GM and GM-PetCoke.

4.3.3. Vapor generation performance

Figure 4.16a depicts the evaporation under 1 sun of the GM and GM-PetCoke composite. When the average values of 3 measurements (pure water) are compared between these two samples, we can see the tendency that the evaporation is higher for the GM-PetCoke composite than the pristine GM. To reinforce this conclusion, the conversion efficiency was calculated. The conversion efficiency of the GM-PetCoke composite was 77.7 ± 1.2%, while that of the GM was 64.2 ± 3.0%. This difference in conversion efficiency reflects the importance of the addition of the petroleum coke in improving evaporation.

In order to ensure the durability of the sample, the evaporation process was carried out several times (**Fig. 4.16b**). Even after repeated use of the sample in contact with seawater and drying, no strong decrease in evaporation was observed. Furthermore, the evaporation of the GM-PetCoke composite exceeded that of the GM for all seven measurements.

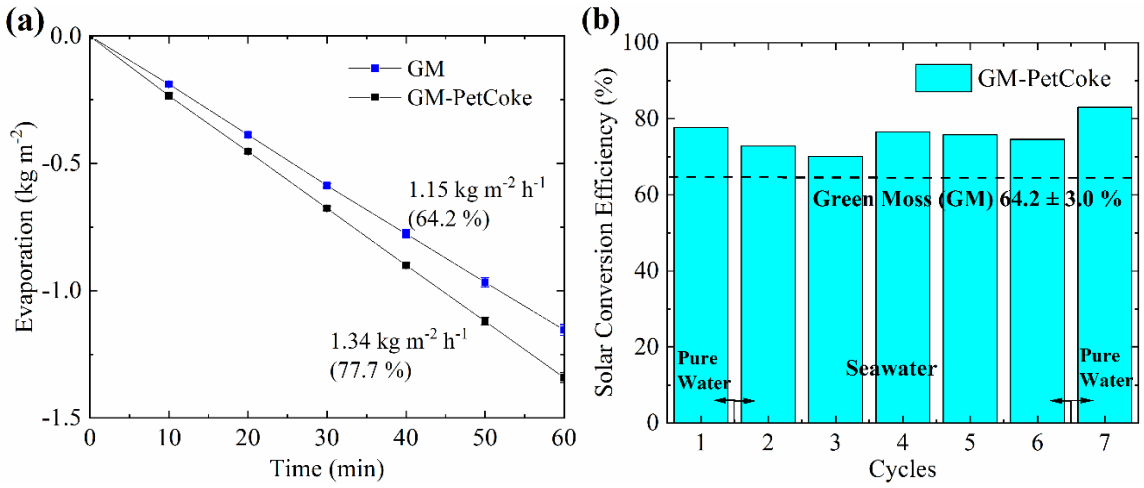

Figure 4.16. (a) Evaporation under 1 sun irradiation of GM and GM-PetCoke. **(b)** Solar conversion efficiency of GM-PetCoke sample.

For evaporation without irradiation (under 0 sun), there is a relatively strong correlation between atmospheric relative humidity and evaporation under 0 sun (GM-PetCoke/Pure water: R^2 = 0.93, GM-PetCoke/Seawater: R^2 = 0.72) (**Fig. 4.17a**). In contrast, there is no correlation between room temperature and evaporation under 0 sun (**Fig. 4.17b**).

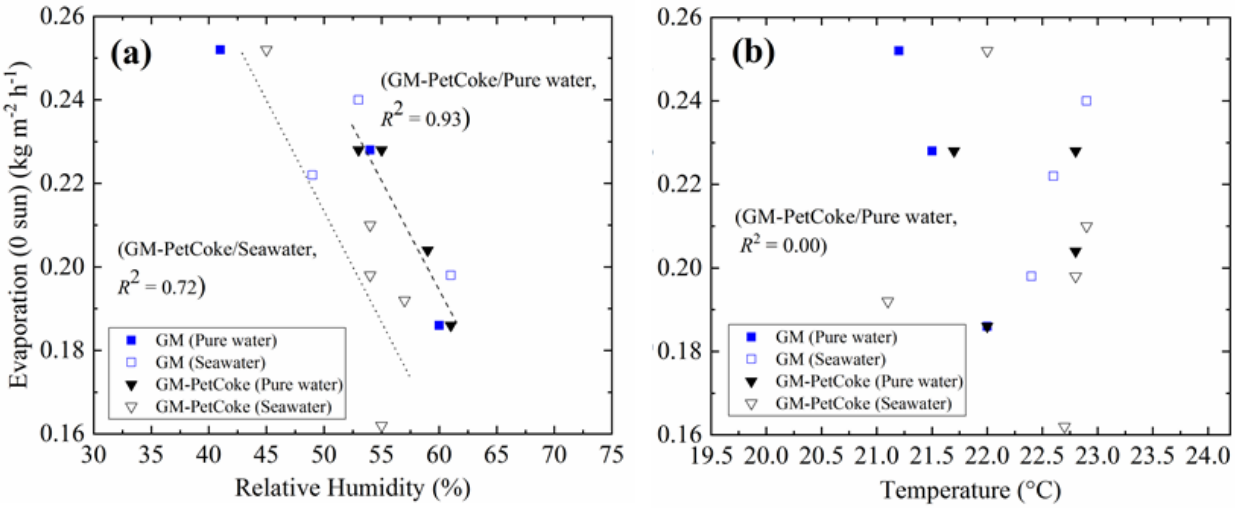

Figure 4.17. **(a)** Correlation between the atmospheric relative humidity and the evaporation under 0 sun, **(b)** Correlation between the room temperature and the 0 sun evaporation rate.

4.3.4. Purification properties

Figure 4.18 shows the concentrations of elements (Na, Mg, K, Ca, B) found in seawater and in condensed water. After condensation, more than 99% of these elements have been removed and, moreover, these concentrations are well below the thresholds advised by the world health organization (WHO) guideline for drinking water criteria [11]. This means that the GM-PetCoke composite can provide high quality drinking water.

Images of agar plates inoculated with bacteria-contaminated water and condensed water are displayed in **Figure 4.18b** and **Figure 4.18c**, respectively. The concentration of *E. coli* in the contaminated water was $1.03 \pm 0.13 \times 10^8$ CFU/mL, and *E. coli* colonies can be confirmed in **Figure 4.18b**. In contrast, no colonies were visible on the plate in **Figure 4.18c**, which proves that the condensed water is free of bacterial contamination.

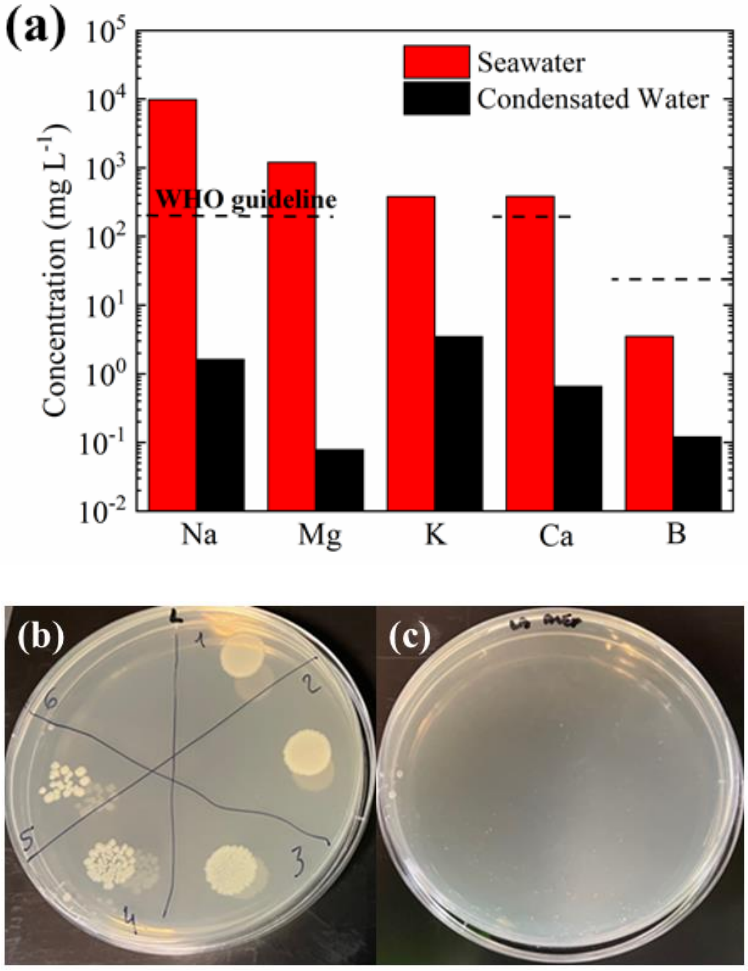

Figure 4.18. **(a)** Concentrations of five elements in the seawater and condensed water, **(b)** Agar plate inoculated with bacteria contaminated water, **(c)** Agar plate inoculated with condensed water.

4.4. Conclusion

In this chapter, the addition of petroleum coke to green moss (GM) was demonstrated by using an extremely facile process in order to examine the improvement of vapor generation by GM. GM is a highly accessible biomass and possesses a good hydrophilicity. Petroleum coke is a by-product of petroleum refining processes and rich in graphitic carbon. Both GM and petroleum coke were able to absorb sunlight and generate heat. With regard to evaporation, the conversion efficiency of the GM-PetCoke composite was 77.7% (evaporation rate: 1.34 kg $m^{-2} h^{-1}$). This value is better than that achieved by the pristine GM (64.2%). This evaporation can be attributed to the excellent photothermal property of petroleum coke. The composite GM-PetCoke is resistant to repeated evaporation and drying cycles.

In addition, this composite is capable of desalting seawater and disinfecting water contaminated with *E. coli* bacteria to produce safe drinking water. Given the facility of preparation of the composite, the accessibility of the raw materials and the excellent heat generation, petroleum coke is a promising additive for the preparation of photothermal materials for solar interfacial evaporation. In addition, the hybrid GM-PetCoke material could be used as a good photothermal evaporator for solar interfacial evaporation.

References

[1] M. Khajevand, S. Azizian, R. Boukherroub, Naturally abundant green moss for highly efficient solar thermal generation of clean water, ACS Applied Materials & Interfaces 13 (2021) 31680.

[2] I.J. Okeke, T.A. Adams, Life Cycle Assessment of Petroleum Coke Gasification to Fischer-Tropsch Diesel, 29th European Symposium on Computer Aided Process Engineering 46 (2019) 1495.

[3] J. Xiao, Q.F. Zhong, F.C. Li, J.D. Huang, Y.B. Zhang, B.J. Wang, Modeling the Change of Green Coke to Calcined Coke Using Qingdao High-Sulfur Petroleum Coke, Energy & Fuels 29 (2015) 3345.

[4] J.G. Speight, The chemistry and physics of coking, Korean Journal of Chemical Engineering 15 (1998) 1.

[5] C.N. Li, Q. Pagneux, A. Voronova, A. Barras, A. Abderrahmani, V. Plaisance, V. Pawlowski, N. Hennuyer, B. Staels, L. Rosselle, N. Skandrani, M.S. Li, R. Boukherroub, S. Szunerits, Near-infrared light activatable hydrogels for metformin delivery, Near-infrared light activatable hydrogels for metformin delivery, Nanoscale 11 (2019) 15810.

[6] M. Budimir, R. Jijie, R. Ye, A. Barras, S. Melinte, A. Silhanek, Z. Markovic, S. Szunerits, R. Boukherroub, Efficient capture and photothermal ablation of planktonic bacteria and biofilms using reduced graphene oxide–polyethyleneimine flexible nanoheaters, Journal of Materials Chemistry B 7 (2019) 2771.

[7] F. Teodorescu, G. Queniat, C. Foulon, M. Lecoeur, A. Barras, S. Boulahneche, M.S. Medjram, T. Hubert, A. Abderrahmani, R. Boukherroub, S. Szunerits, Transdermal skin patch based on reduced graphene oxide: A new approach for photothermal triggered permeation of ondansetron across porcine skin, Journal of Controlled Release 245 (2017) 137.

[8] J. Hoffmann, C.U. Jensen, L.A. Rosendahl, Co-processing potential of HTL bio-crude at petroleum refineries – Part 1: Fractional distillation and characterization, Fuel 165 (2016) 526.

[9] A.D. Manasrah, N.N. Nassar, L.C. Ortega, Conversion of petroleum coke into valuable products using oxy-cracking technique, Fuel 215 (2018) 865.

[10] Q.F. Zhong, Q.Y. Mao, J. Xiao, A. van Duin, J.P. Mathews, Sulfur removal from petroleum coke during high-temperature pyrolysis. Analysis from TG-MS data and ReaxFF simulations, Journal of Analytical and Applied Pyrolysis 132 (2018) 134.

[11] Guidelines for Drinking-water Quality, 4th edition, incorporating the 1st addendum, World Health Organization (2011) (available at: https://www.who.int/publications/i/item/9789241549950).

Chapter 5: Cigarette filter - Petroleum coke

5.1. Introduction

A cigarette filter, made of cellulose acetate, owing to its excellent hydrophilicity could fulfil some of the requirements of a base material for an evaporator. On the other hand, a great amount of cigarette butts is discharged into the environment, which constitutes an environmental hazard. Indeed, cigarette butts cause significant harm to the natural environment by being carried, as runoff, to drains and from there to rivers, beaches and oceans. The filters of cigarettes are mostly not bio-degradable, and contain toxic compounds [1], so it would be necessary to collect them and revaluate this waste. The use of cigarette filters for solar-driven interfacial evaporation has been already reported in a few examples. For instance, Sun et al. [2] elaborated a 2D evaporator of cigarette filters embedded with reduced graphene oxide (rGO), reaching a water evaporation rate of 1.62 kg m^{-2} h^{-1} and a conversion efficiency of 94%. Yu et al. [3] prepared a 3D evaporator with cigarette filters combined with rGO, exhibiting a water evaporation rate of 2.81 kg m^{-2} h^{-1} and an energy conversion efficiency of 130.2%. Li et al. [4] reported a 3D evaporator of cigarette filters decorated with MXene sheets, whose water evaporation rate was 3.38 kg m^{-2} h^{-1} and a conversion efficiency of 132.9%. However, several problems remain. First, the shape of the evaporators in some of these researches is different from that intended for real operation. For practical operation, the presence of a great number of 3D channels juxtaposed with each other is of high importance. In this case, the lateral side of most of the protrusions is surrounded by other humid protrusions. Therefore, there will be an increase of humidity between the protrusions, which can be a great factor for a decrease of evaporation. Moreover, the conversion efficiency must be evaluated precisely, because the evaporation under 0 sun changes significantly depending on the meteorological conditions.

Petroleum coke is a residual by-product of crude oil refining processes. This product is partially recycled in the field of metallurgy and cement industry. However, it is discarded in large quantities [5]. Major element of the petroleum coke is carbon consisting of multiple aromatic rings [6]. In spite of a relatively high concentration of impurities (O, S, N, metal elements), because of the structural similarity with other carbon-based materials, such as graphene oxide (GO) and rGO, a good photothermal property could be expected for the petroleum coke even though this has not been assessed nor reported.

In this chapter, we combined petroleum coke with cigarette butts to prepare an evaporator to absorb efficiently the sunlight using an extremely simple method. Cigarette filters were immersed in the petroleum coke suspension and subsequently dried. By controlling the

evaporator architecture, it was possible to reach a high evaporation rate and solar conversion efficiency.

5.2. Experimental section

5.2.1. Preparation of cigarette filter/petroleum coke (Filter-PetCoke) evaporators

The evaporators were prepared from used filters from cigarette butts. Firstly, the filters were extracted from the cigarette butts. Then, 40 filters were put in ethanol (500 mL) under magnetic stirring to extract the toxic compounds. Ethanol was repeatedly replaced by a new one every 45 min until the colour of the ethanol was no longer brown [2]. Afterwards, the washed filters were dried in an oven at 60 °C overnight.

The petroleum coke (500 mg) was dispersed in a mixture of ethanol (12 mL) and water (30 mL) by ultrasonication for 5 min. Then, 13 filters were added to this suspension placed in a centrifugation tube, and the tube was put in a tube revolver rotator at a speed of 10 rpm for 18 h. After retrieving the filters from the suspension, the filters were dried in the oven at 60 °C overnight. This product is henceforward called as Filter-PetCoke.

For the characterisation experiments except the evaporation test (SEM-EDX, ultraviolet/visible/near-infrared spectrometry, heat profile in dried state, water contact angle, FTIR, XPS and TGA), the Filter-PetCoke was prepared from the pristine filter (**New Filter**) in the same way without preliminary washing by ethanol. **Figure 5.1** shows photographs of the New Filter (white) and Filter-PetCoke (black).

Figure 5.1. Photographs of the New Filter (upper) and the Filter-PetCoke composite (lower).

5.2.2. Preparation of 2D and 3D evaporators

For the vapor generation (Sub-chapter **5.3.2.**) and the purification (Sub-chapter **5.3.3.**) tests, the evaporator was made by assembling multiple filters derived from used cigarette butts. The diameter of each filter is approximately 7 mm, and the length is at maximum 24 mm. **Figure 5.2a** is a scheme of the 3D evaporator, which is composed of 41 filters. The height difference between the upper and the lower filter was set to 2.1 cm. On the other hand, for the 2D structure, the evaporator is composed of 28 filters, i.e. without the 13 upper filters A2, A5, A8, A11, A14, A17, A20, A23, B1, B4, B7, B10, and B13, and with no height difference.

Figure 5.2b depicts a photo of the 3D evaporator consisting of Filter-PetCoke composite. For the evaporation, the aforementioned evaporator was directly put on a 50 mL PTFE beaker filled with either pure water or seawater. In that way, the bottom of the evaporator was in contact with the water, and thanks to the hydrophilicity of the cigarette filter, the water was lifted up by capillarity to the interface between the evaporator and the outer atmosphere (**Fig. 5.2c**).

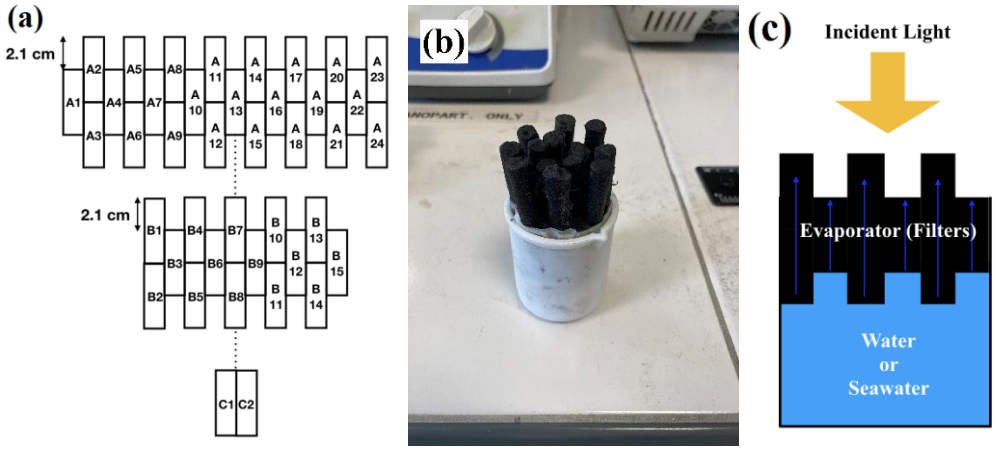

Figure 5.2. **(a)** Scheme of the evaporator composed of the cigarette filters (A is the most outside layer, and C is the most inside layer), **(b)** Photo of the 3D evaporator, **(c)** Scheme of the whole device.

5.3. Results and discussion

5.3.1. Characterization of the filter - petroleum coke composite

Figure 5.3 shows the EDX spectra of the New Filter and Filter-PetCoke composite. Before addition of the petroleum coke, the filter consists only of C and O (and H, which cannot be detected by EDX). The presence of S and Pb elements, which originated from the petroleum coke, in addition to C and O, obviously indicated the successful loading of the petroleum coke powder into the cigarette filter.

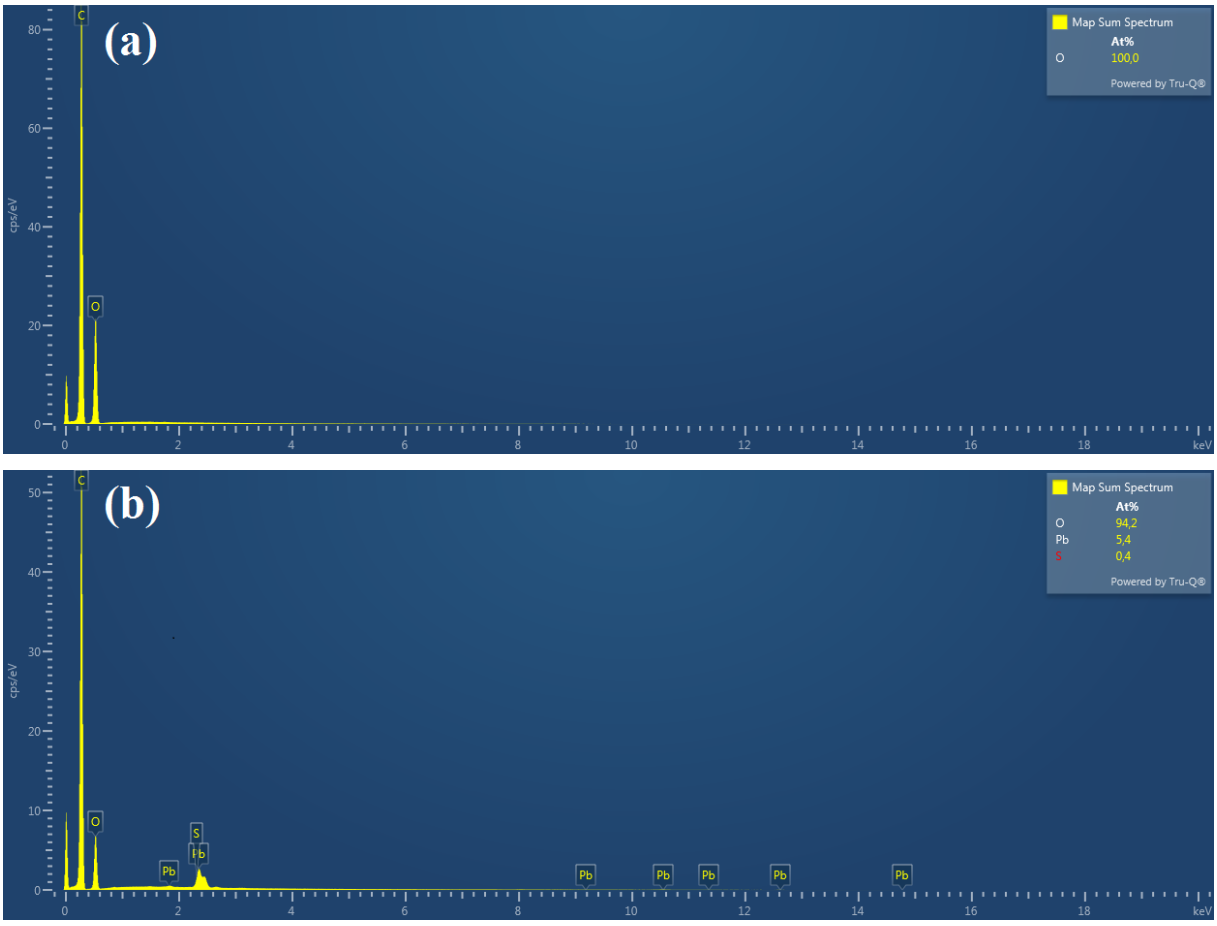

Figure 5.3. EDX spectra of **(a)** New Filter and (**b**) Filter-PetCoke.

Figure 5.4 displays the FTIR spectra of the cigarette filter before and after loading with petroleum coke and that of the initial petroleum coke powder. In the FTIR plot of the petroleum coke, four pics could be observed at 1635, 1437, 876, and 749 cm^{-1}. The peak at 1635 cm^{-1} is

due to the stretching of the C=C bond. The peak at 1437 cm^{-1} is likely to be caused by methylene H–C–H scissoring motion [7]. The latter two features are ascribed to C–H bonds out-of-plane vibrations in aromatic moieties [8].

The FTIR spectrum of the New Filter comprises several bands. The broad band at 3489 cm^{-1} could be unambiguously assigned to the stretching of OH groups [9]. The peak at 2960 cm^{-1} corresponds to the stretching of C–H [10]. The 1760 cm^{-1} band is due to the carbonyl C=O stretching, while the 1636 cm^{-1} peak can be assigned to H–O–H bending of the water. The peaks at 1382, 1237, 1160, 1033 and 901 cm^{-1} are ascribed respectively to C–H stretching in –O(C=O)–CH_3, C–O–C antisymmetric stretching of ester group, antisymmetric C–O stretching, C–O–C pyranose ring vibration [11], and C–O stretching in the glycosidic bond. The peaks appeared in the New Filter can be found in the cellulose acetate [9][10], therefore we could confirm that the New Filter is composed of the cellulose acetate.

The FTIR plot of the composite Filter-PetCoke showed a very similar spectral pattern as that of the New Filter. This implies that the loading of petroleum coke into the cigarette filter did not bring any chemical changes to the cigarette filter.

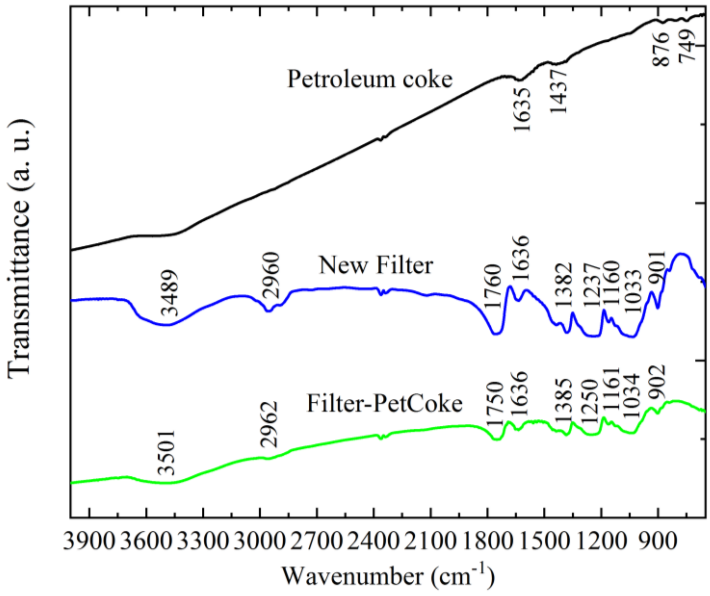

Figure 5.4. FTIR spectra of the petroleum coke powder, New Filter and Filter-PetCoke materials.

The chemical composition and electronic state of different elements in the parent cigarette filter before and after loading with petroleum coke powder are displayed in **Figure 5.5**. The full XPS spectrum of the New Filter (**Fig. 5.5a**) consists only of O 1s (532 eV) and C 1s (285 eV), in full

accordance with a sample devoid of any contamination. After loading of petroleum coke powder onto the New Filter, additional peaks due to S 2p (163 eV), and Pb 4f (144 and 139 eV) were clearly observed, inferring the successful integration of the petroleum coke powder within the cigarette filter. **Figure 5.5b** is the high-resolution plots of the C 1s of these samples. Before the addition of the petroleum coke, fours peaks derived from the acetate cellulose, O=C–O (288.7 eV), O–C–O (287.7 eV), C–O (286.0 eV), and C–C (284.5 eV), were clearly evidenced. After the addition of the petroleum coke, the intensity of the C–C peak increased significantly (**Table 5.1**), in accordance with the insertion of graphite-like carbon brought by the petroleum coke.

Table 5.1. Atomic percentage of each component of the C 1s peak (at.%).

	O=C–O	O–C–O	C–O	C=C/C–C
New Filter	8.2	25.7	32.0	34.1
Filter-PetCoke	14.5	5.6	18.2	61.3

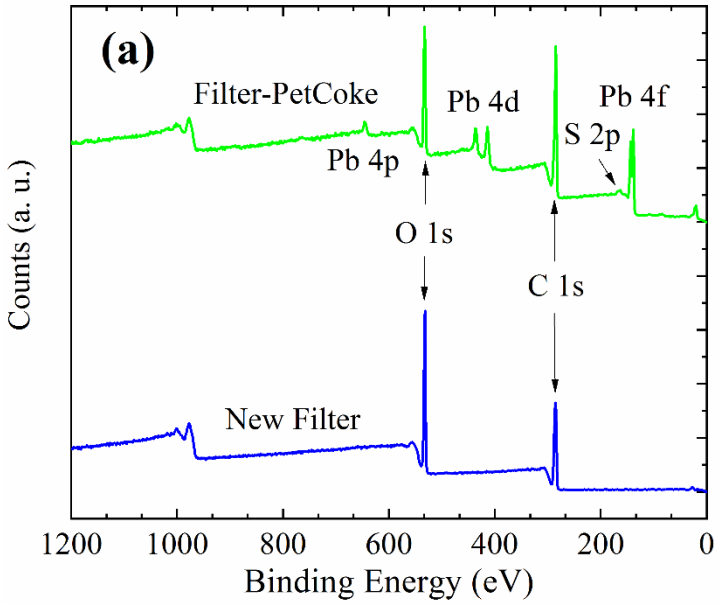

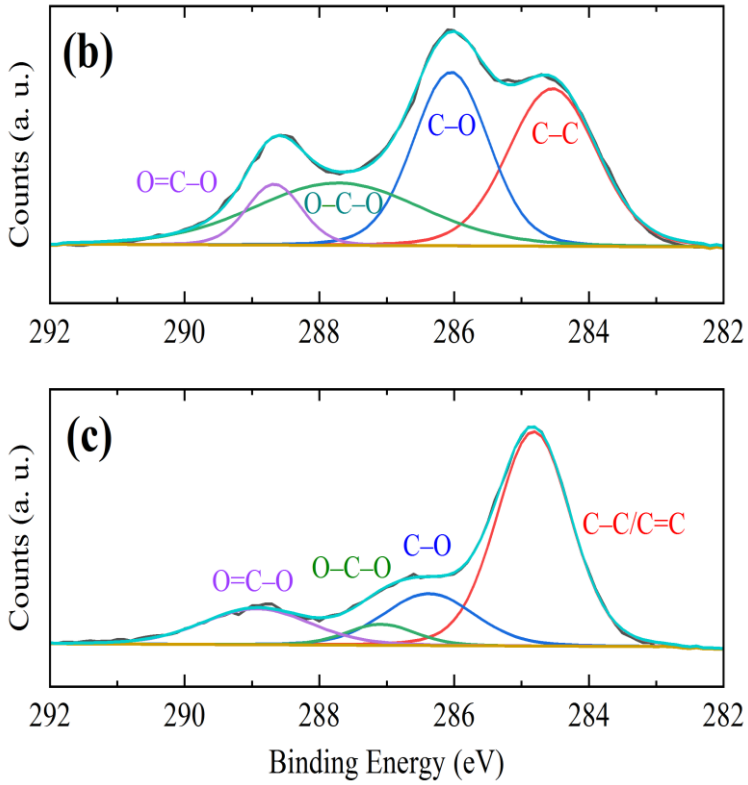

Figure 5.5. **(a)** Low- and high-resolution XPS spectra of the C 1s of **(b)** New Filter and **(c)** Filter-Petcoke samples.

The thermal behaviour of the different samples investigated in this study were probed by thermal gravimetric analyses (TGA). **Figure 5.6** presents the thermogravimetry (TG) and derivative thermogravimetry (DTG) curves of the petroleum coke and the filter samples. From the graph in **Figure 5.6a**, it could be inferred that the petroleum coke was thermally stable with a total weight loss of about 13% over the whole temperature range (room temperature to 920 °C). This contrasts with the thermal behaviour of the New Filter which experienced almost a full degradation under otherwise identical operating conditions (about 94% weight loss at 920 °C). The Filter-PetCoke composite exhibited a thermal decomposition pattern comprised between those of the initial petroleum coke powder and the New Filter with a total weight loss of 77% at 920 °C.

Figure 5.6b depicts the DTG curves. The DTG curve of the petroleum coke powder comprised three peaks at 320, 490 and 620 °C. The first peak at 320 °C is due to volatile substances. The second peak at 490 °C and the third peak at 620 °C are due to carbon and hydrogen losses during pyrolysis [12]. The sharp peaks at 365 and 350 °C, recorded respectively for the New Filter and Filter-PetCoke, were assigned to the cellulose acetate chain degradation because of the breakdown of glycosidic bonds [13]. This result also implies that the New Filter is made of the cellulose acetate.

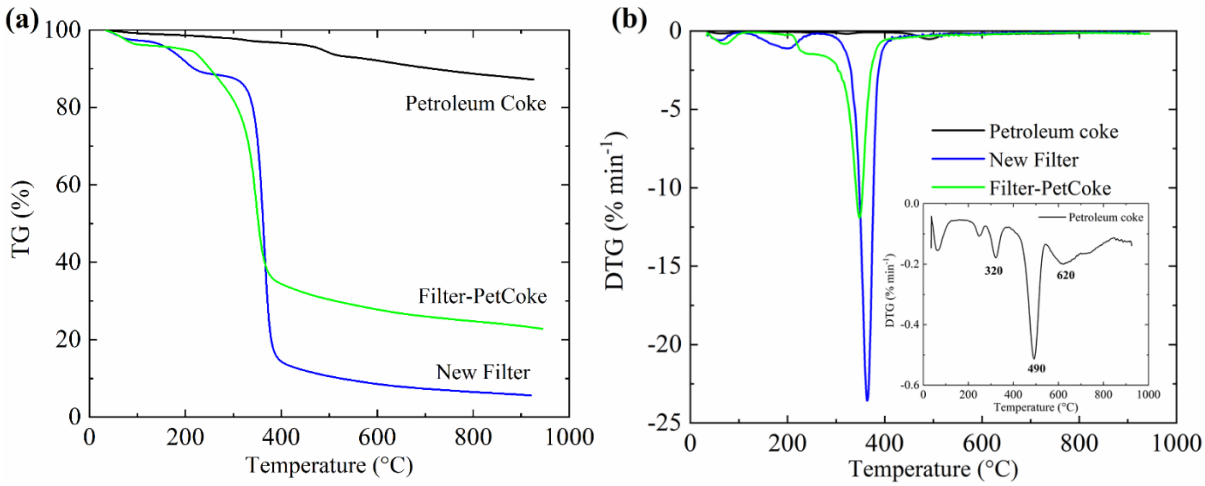

Figure 5.6. **(a)** TG and **(b)** DTG curves of the different samples. The inset is the enlarged DTG curve of the petroleum coke.

Figure 5.7 displays the scanning electron microscopy (SEM) images of the New Filter and Filter-PetCoke composite. **Figure 5.7a** indicates that the New Filter owns a smooth surface and is composed of cellulose acetate fibres whose diameter is about 30-40 µm. From the BED-C mode image (**Fig. 5.7b**), no white spots were evidenced. However, the surface of the composite sample becomes rough (**Fig. 5.7c**), and from the BED-C image (**Fig. 5.7d**), one clearly sees that the fibre surface is homogeneously covered by white spots, suggesting that the petroleum coke is distributed evenly on the surface.

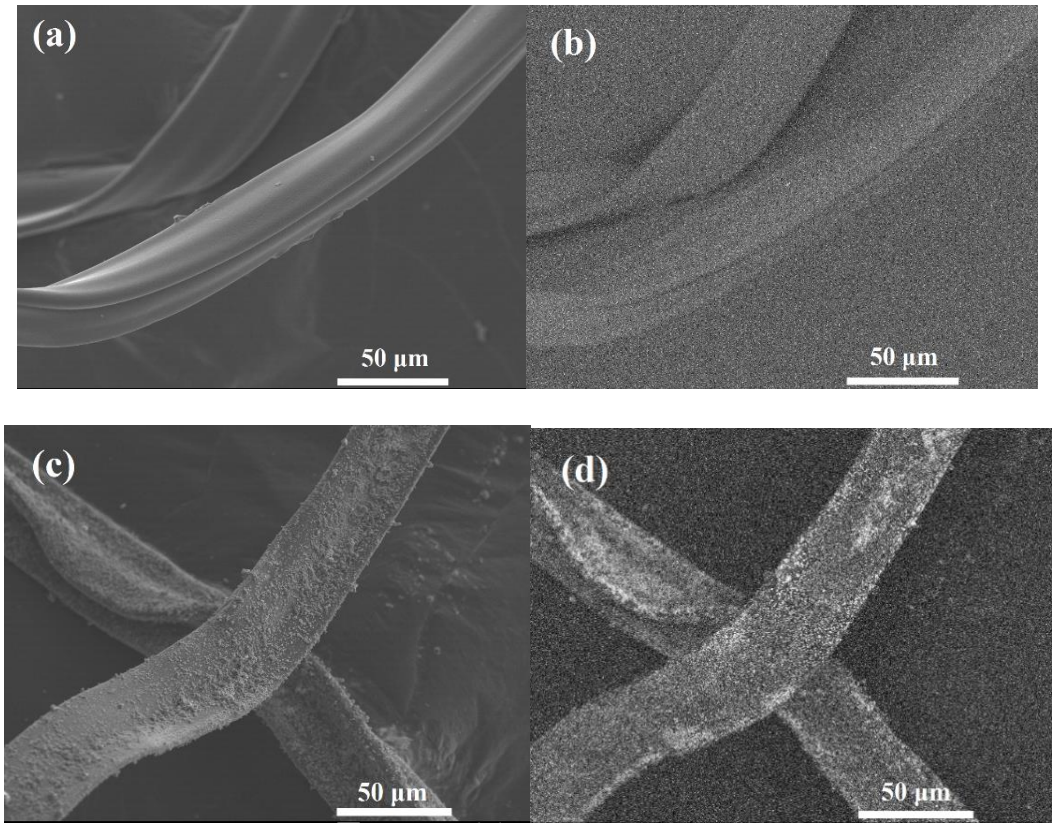

Figure 5.7. SEM images **(a)** LED and **(b)** BED-C modes of the New Filter, and **(c)** LED and **(d)** BED-C modes of Filter-PetCoke composite.

Figure 5.8a exhibits the reflectance spectra of the New Filter and Filter-PetCoke samples. Interestingly, the New Filter exhibits low reflectance (<1.5%) all over the wavelength surveyed (300-2000 nm), and the reflectance decreased to <1% upon loading the filter with petroleum coke powder. It implies that the petroleum coke on the prepared Filter-PetCoke is capable of absorbing the incident visible/NIR light.

Figure 5.8b shows the change of the surface temperature of the three samples, New Filter, Filter-PetCoke and filter derived from a real cigarette butt under the irradiation of 1 sun. While the New Filter could absorb efficiently the incident visible/NIR light, it failed to generate heat; its surface temperature remained at about 25 °C throughout the irradiation period (900 s). This contrasts with the surface temperature of the Filter-PetCoke composite which reached about 62 °C (average value between 300 and 900 s) under otherwise identical irradiation conditions. This difference can be also verified in the thermal imaging picture (**Fig. 5.8b** inset). For the New Filter, the colour by the thermal imaging is purple (the same colour as other objects without the irradiation), while the composite Filter-PetCoke is shown in yellow/white. This difference

means that the petroleum coke is helpful for the improvement of the absorption of the incident light and heat generation.

The temperature of the filter from the real cigarette butt reached 34 °C. The difference between the New Filter and the filter from the real cigarette butt can be ascribed to impurities existing in the used filter. The efficient light to heat conversion of the Filter-PetCoke holds great promise for its application as an evaporator in interfacial water evaporation processes.

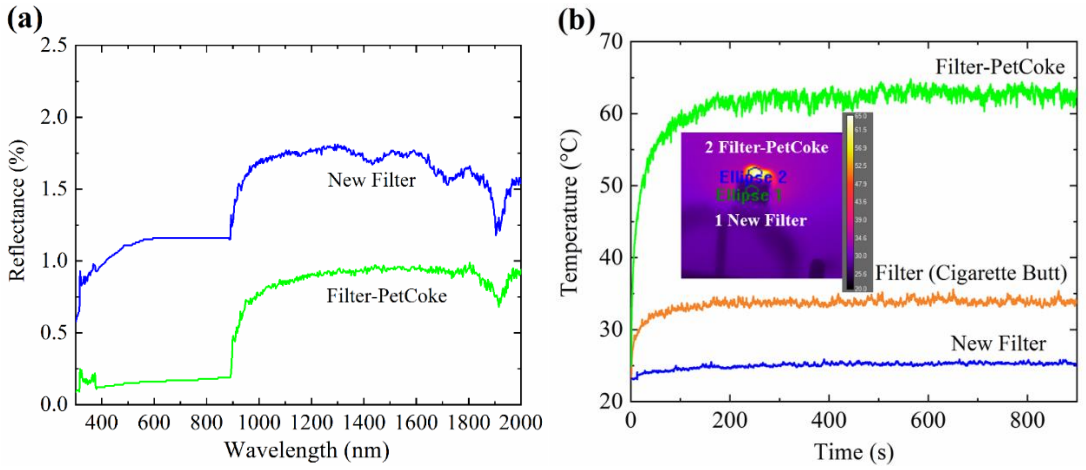

Figure 5.8. **(a)** Reflectance spectra and **(b)** heat profiles in dry state under irradiation of 1 sun of cigarette filter-derived samples.

For an effective evaporation process, the water in the reserve should be lifted up to the interface by the material through capillarity. This requires the entire surface (internal and external) of the filters to be hydrophilic. Therefore, the wetting behaviour of the filters was assessed through water contact angle measurements (**Fig. 5.9**). The New Filter exhibited an excellent hydrophilicity with full adsorption of a water droplet within 1 s, while after incorporation of the petroleum coke within the filter, the water droplet was fully adsorbed within 5 s. We can thus conclude that the composite, despite a lower hydrophilicity compared to the non-treated state in the same way as the GM-PetCoke in the previous chapter, remained hydrophilic, which is a prerequisite for an effective evaporation under light irradiation.

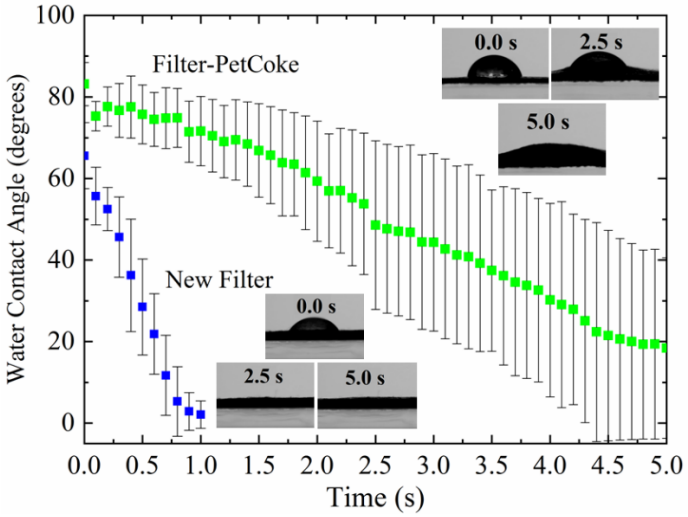

Figure 5.9. Wetting properties of New Filter and Filter-PetCoke samples.

5.3.2. Vapor Generation

Figure 5.10a shows the evolution of the evaporation rate of four different Filter-Petcoke evaporators with various configurations under 1 sun irradiation. The evaporation rate of the 3D Filter-Petcoke device reached 1.97 ± 0.08 kg m^{-2} h^{-1}. This value is much higher than other evaporators i.e. cigarette filter evaporators without the petroleum coke (3D: 1.62 ± 0.07 kg m^{-2} h^{-1}, 2D: 0.84 ± 0.07 kg m^{-2} h^{-1}), and 2D device structure counterpart of the Filter-Petcoke (1.14 ± 0.02 kg m^{-2} h^{-1}). However, the evaporation rate is highly dependent upon the meteorological condition. Moreover, though a high value of 0 sun evaporation has a significance between the start and the humidity saturation in the chamber, it is the conversion efficiency that is important for the operation after the humidity saturation, because the 0 sun evaporation will vanish under 100% humidity.

In addition, the 3D Filter-PetCoke evaporator was by far the most effective sample with a conversion efficiency of 93.2 ± 5.4% among the 4 evaporators (3D Filter: 73.3 ± 7.9%, 2D Filter-PetCoke: 64.0 ± 3.1%, 2D Filter: 41.9 ± 3.8%). This result means that both the enhanced photothermal properties of the petroleum coke and the 3D structure of the evaporator improved the efficient capture and conversion of the incident light for vapour generation. These values of the conversion efficiency and evaporation rate are the highest ones among the recent scientific data (**Table 5.2**). However, it is slightly lower than the rate of previous research [3][4] using the cigarette filters because this research takes into account the increase in the humidity between the juxtaposed wet filters. The relatively high evaporation scores by Filter (without PetCoke) evaporators could be due to the impurities contained in the used cigarette butts (**Fig. 5.8b**).

The durability of an evaporator is also an important requirement for a practical operation. **Figure 5.10b** shows the solar conversion efficiencies when the 3D Filter-PetCoke evaporator underwent 4 times of evaporation of pure water, followed by 4 subsequent evaporation cycles of real seawater. Even after 8 utilisations, the solar conversion efficiency remained much better than that recorded for the other evaporators, which means this evaporator is well-resistant to repetitive uses.

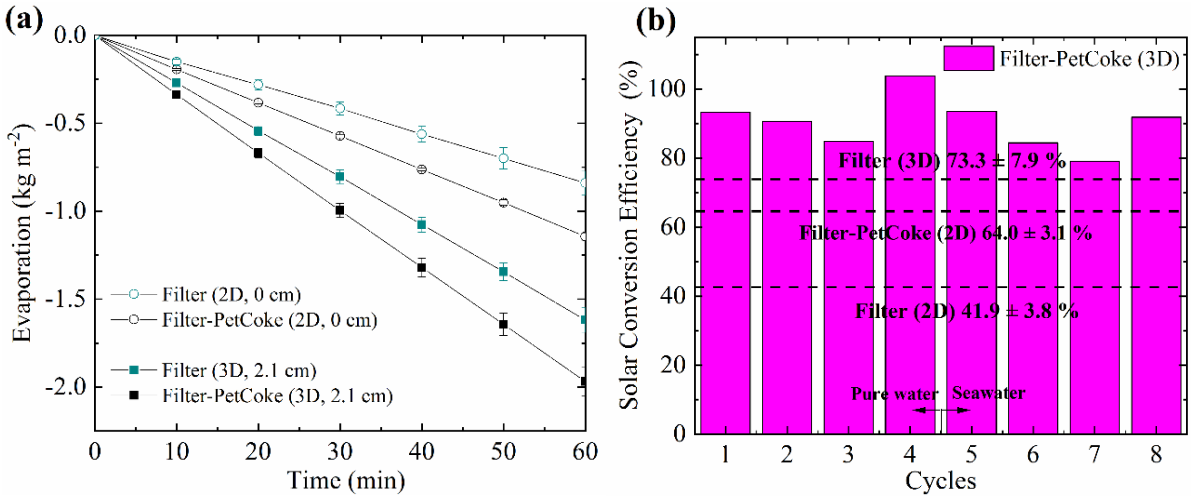

Figure 5.10. **(a)** Evaporation under 1 sun, **(b)** Conversion efficiency of the 3D Filter-PetCoke evaporator.

Table 5.2. Comparison of the performance of the 3D filter-petroleum coke with literature data.

	Evaporation rate ($kg\ m^{-2}\ h^{-1}$)	**Conversion efficiency (%)**	**Reference**
Filter-PetCoke (3D)	**1.97 ± 0.08**	**93.2 ± 5.4**	**This work**
Filter-rGO	1.623	94	2
Polyester-PPy-PFDTS	1.49	91.68	14
PDMS sponge-carbon nanoparticles	1.36	77.8	15
Hydrophobic and porous carbon nanofiber	1.43	87.5	16

Figure 5.11 presents the 0 sun evaporation of the four previously tested evaporators. Firstly, the 0-sun evaporation is greatly dependent on the humidity. Especially for the 3D structure

(Filter-PetCoke, Pure water), the 0-sun evaporation varies from 0.74 kg m^{-2} h^{-1} at 46% humidity to 0.38 kg m^{-2} h^{-1} at 71% humidity, which is a strong evidence that one should consider the conversion efficiency rather than the crude value of the evaporation. The 0-sun evaporation of the 3D structure is about 2.5 times greater than that of the 2D structure under the same humidity. On the other hand, the surface area of the 3D structure (approximately 71 cm^2) is about 6- to 7-times greater than that of the 2D structure (11.34 cm^2). This implies that the evaporation on the lower and lateral sides of the evaporator can be hindered due to the local increase of the humidity between the wet filters. On the other hand, there was no evident correlation between the atmospheric temperature and the 0-sun evaporation rate in the analysed temperature range.

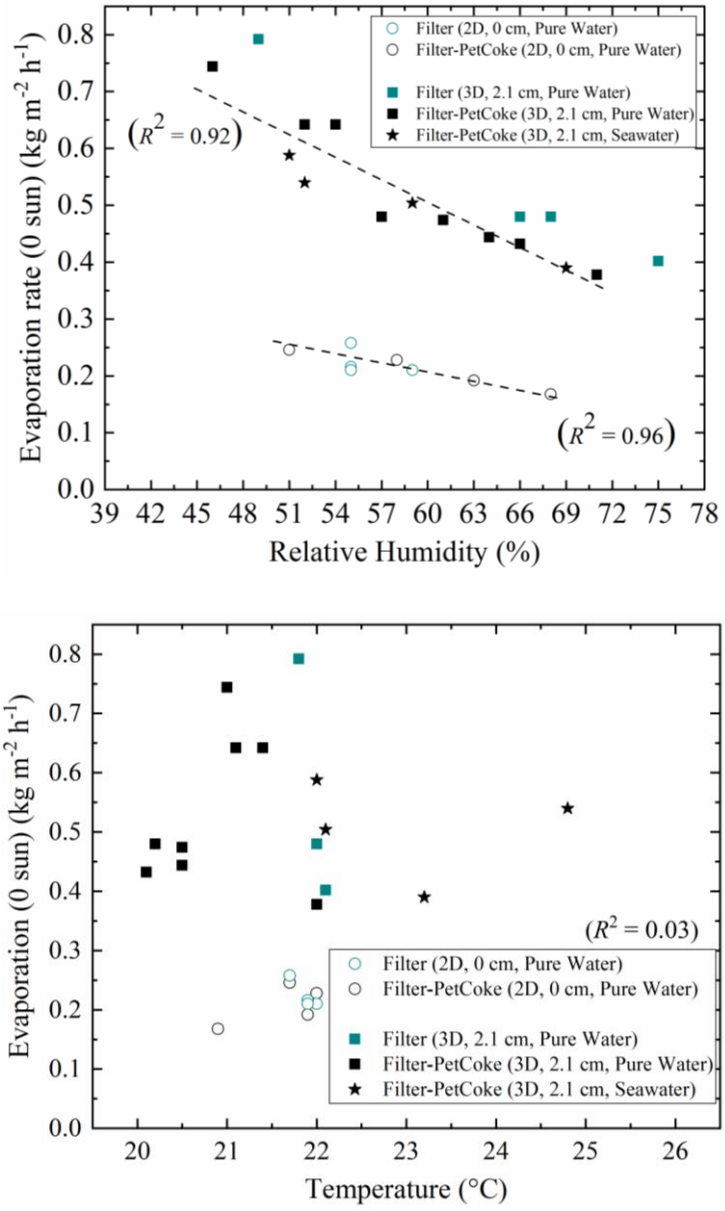

Figure 5.11. Upper; Correlation between the atmospheric relative humidity and the 0 sun evaporation rate, Lower; between the atmospheric temperature and the 0 sun evaporation rate.

In absence of incident light (**Figure 5.12a,c**), the temperature of the bottom of the evaporator is higher than that of the top part. This means that the top part undergoes more evaporation, while there is less evaporation from the bottom part because of the locally increased humidity between the wet filters. If the atmospheric humidity is relatively low (**Figure 5.12b**), this tendency is maintained under 1 sun irradiation. This is likely to be due to the great evaporation from the top part of the evaporator. On the contrary, under 1 sun irradiation, if the atmospheric humidity is high (**Figure 5.12d**), the top part of the evaporator is warmer than the bottom. This can be ascribed to heat accumulation, due to weaker evaporation. Indeed, the bottom part is closer to the bulk water and the lower part of the adjacent filters, so the bottom part has more chance to be cooled down.

This tendency can be confirmed when the difference between the surface temperature and the ambient temperature is plotted against the relative humidity (**Fig. 5.13**). There is less heat loss for the top part of the 3D structure, which could be the reason for the excellent conversion efficiency.

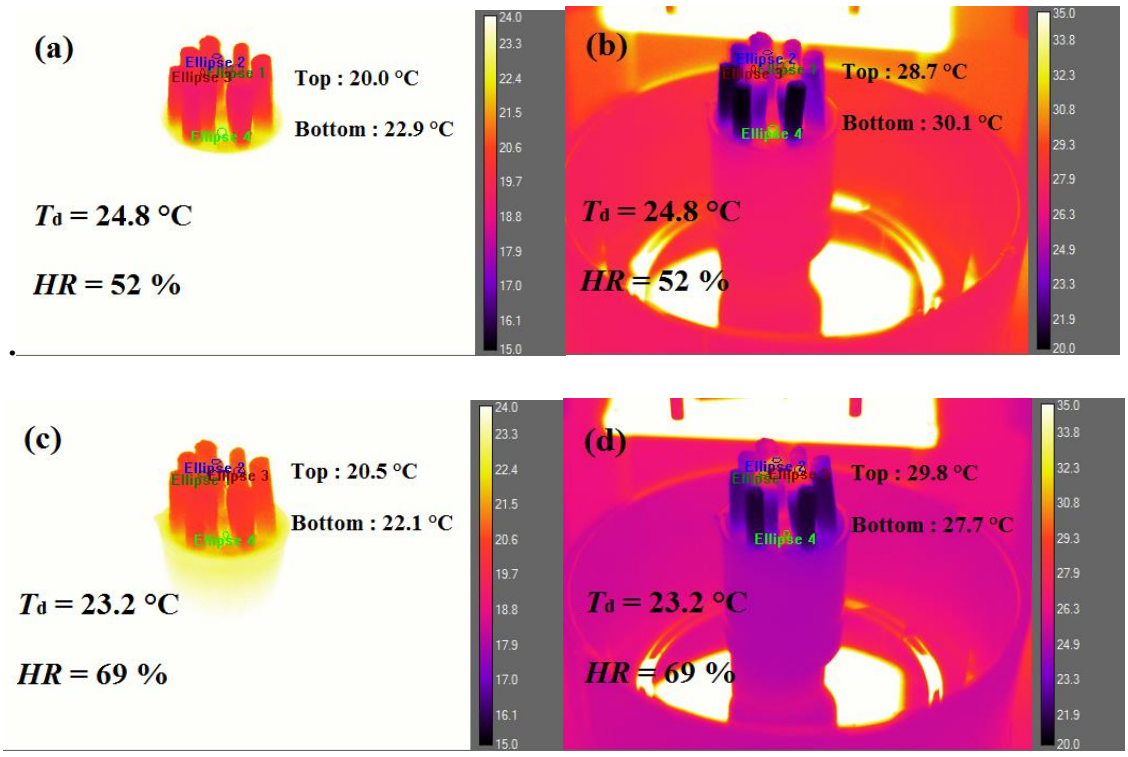

Figure 5.12. Infrared camera images for the wet state of the 3D Filter-PetCoke evaporator: **(a, c)**: 0-sun, **(b, d)**: 1-sun.

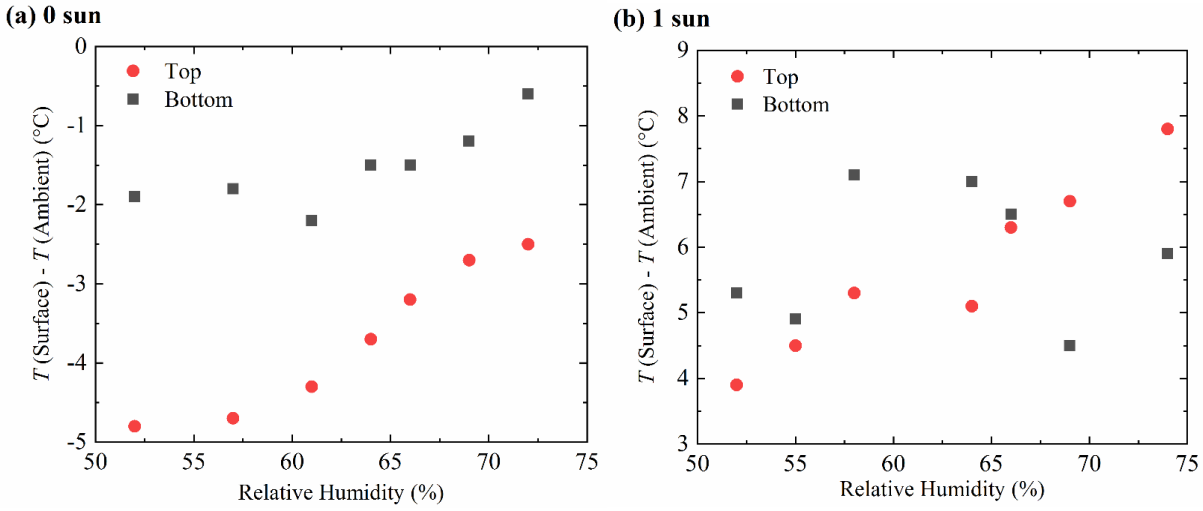

Figure 5.13. Difference between the surface temperature and the ambient temperature (**(a)**: 0 sun, **(b)**: 1 sun)

5.3.3. Purification properties

There are two major risks for water intake: chemical [17] and bacterial [18] risks. Therefore, the concentrations of six selected elements (Na, Mg, K, Ca, B, Pb) in the seawater and condensed water were estimated using ICP-OES. After the condensation process, more than 99% of these elements were eliminated and the concentrations of all these elements can satisfy the recommended/required value by the World Health Organisation (WHO) (**Figure 5.14**) [19]. This means that the device is capable to produce safe drinking water and there would be no concerns about the contamination of Pb in the condensed water. This result also supports the absence of Pb leaching from the petroleum coke during the evaporation process.

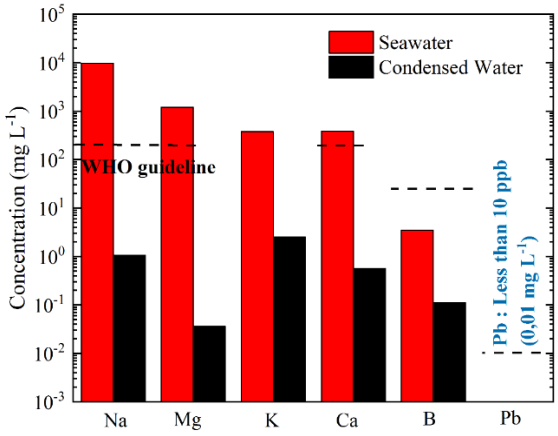

Figure 5.14. Concentration of selected elements in the seawater and the condensed water.

Another risk to the human being is an intake of bacteria-contaminated water. The simulated contaminated water (*E. coli*, $0.7 \pm 0.05 \times 10^8$ CFU mL^{-1}) was used for the water supply to verify the effectiveness of the device for bacteria elimination. In contrast to the agar plate inoculated with bacteria-contaminated water, no colony of bacteria was observed in the agar plate inoculated with the condensed water, which means that the condensed water is free of bacterial contamination (**Figure 5.15**). The findings of these two experiences infer that this device is able to produce drinking water free of metal and bacterial contamination.

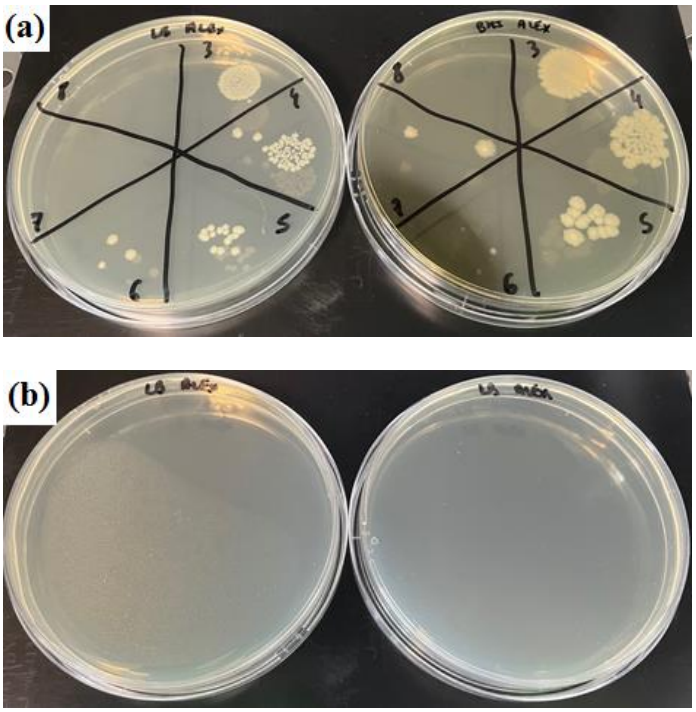

Figure 5.15. Bacteria inoculated onto the agar plates **(a)** bacteria contaminated water (serial dilution from 10^{-3} to 10^{-8}), and **(b)** condensed water.

5.4. Conclusion

In this chapter, we have demonstrated that the easily accessible petroleum coke and cigarette butt wastes could be used for the development of an efficient evaporator for the solar-driven interfacial evaporation using an extremely facile process. Beside its simplicity, the strength of this approach is the ability to construct 2D and 3D structures to assess the influence of the evaporator architecture on the evaporation efficiency.

Thanks to the synergy between the enhanced photothermal properties of the petroleum coke, heat management and hydrophilicity of the 3D structure, the 3D evaporator consisting of Filter-PetCoke achieved excellent evaporation performance (evaporation rate: 1.97 ± 0.08 kg m^{-2} h^{-1}, solar conversion efficiency: 93.2 ± 5.4%). This value takes into consideration the condition of real operation, such as the increased humidity between the filters or the patterned geometry. Moreover, this easy evaporation device is capable to remove metal ions from seawater and eliminate *E. coli* bacteria from contaminated water, which are essential requirements for reliable freshwater production device.

References

[1] H. Kurmus, A. Mohajerani, The toxicity and valorization options of cigarette butts, Waste Management, 104 (2020) 104.

[2] H.X. Sun, Y.Z. Li, Z.Q. Zhu, P. Mu, F. Wang, W.D. Liang, C.H. Ma, A. Li, Photothermal Conversion Material Derived from Used Cigarette Filters for Solar Steam Generation, ChemSusChem, 12 (2019) 4257.

[3] M.Y. Yu, C. Li, W. Li, P. Min, Reduced Graphene Oxide Decorated Cellulose Acetate Filter Evaporators for Highly Efficient Water Evaporation and Purification Driven by Solar Energy and Environmental Energy, Adv. Sustain. Syst., (2022) 2200023.

[4] W. Li, X.H. Tian, X.F. Li, J. Liu, C.J. Li, X.Y. Feng, C. Shu, Z.Z. Yu, An environmental energy-enhanced solar steam evaporator derived from MXene-decorated cellulose acetate cigarette filter with ultrahigh solar steam generation efficiency, J. Colloid Interface Sci., 606 (2022) 748.

[5] J.M. Hill, A. Karimi, M. Malekshahian, Characterization, gasification, activation, and potential uses for the millions of tonnes of petroleum coke produced in Canada each year, Can. J. Chem. Eng., 92 (2014) 1618.

[6] Y. Xiao, J.M. Hill, Solid acid catalysts produced by sulfonation of petroleum coke: Dominant role of aromatic hydrogen, Chemosphere, 248 (2020) 125981.

[7] J. Hoffmann, C.U. Jensen, L.A. Rosendahl, Co-processing potential of HTL bio-crude at petroleum refineries - Part 1: Fractional distillation and characterization, Fuel, 165 (2016) 526.

[8] A.D. Manasrah, N.N. Nassar, L.C. Ortega, Conversion of petroleum coke into valuable products using oxy-cracking technique, Fuel, 215 (2018) 865.

[9] M. Namjoufar, A. Farzi, A. Karimi, Removal of Acid Brown 354 from wastewater by aminized cellulose acetate nanofibers: experimental and theoretical study of the effect of different parameters on adsorption efficiency, Water Sci. Technol., 83 (2021) 1649.

[10] T. Sudiarti, D. Wahyuningrum, B. Bundjali, I.M. Arcana, Mechanical strength and ionic conductivity of polymer electrolyte membranes prepared from cellulose acetate-lithium perchlorate, Innov. Polym. Sci. Technol., 223 (2017) 012052.

[11] J. Li, L.P. Zhang, F. Peng, J. Bian, T.Q. Yuan, F. Xu, R.C. Sun, Microwave-Assisted Solvent-Free Acetylation of Cellulose with Acetic Anhydride in the Presence of Iodine as a Catalyst, Molecules, 14 (2009) 3551.

[12] Q.F. Zhong, Q.Y. Mao, J. Xiao, A. van Duin, J.P. Mathews, Sulfur removal from petroleum coke during high-temperature pyrolysis. Analysis from TG-MS data and ReaxFF simulations, J. Anal. Appl. Pyr., 132 (2018) 134.

[13] M.D.E. Pinto, D.D. de Silva, A.L.A. Gomes, V.D.A. Leite, A.R.F.E. Moraes, R.F. de Novais, J. Tronto, F.G. Pinto, Film based on magnesium impregnated biochar/cellulose acetate for phosphorus adsorption from aqueous solution, RSC Adv., 9 (2019) 5620.

[14] C. Zhang, P. Xiao, F. Ni, J.C. Gu, J.H. Chen, Y.J. Nie, S.W. Kuo, T. Chen, Breathable and superhydrophobic photothermic fabric enables efficient interface energy management via confined heating strategy for sustainable seawater evaporation, Chem. Eng. J., 428 (2022) 131142.

[15] X.S. Li, S.Y. Tanyan, S.J. Xie, R. Chen, Q. Liao, X. Zhu, X.F. He, A 3D porous PDMS sponge embedded with carbon nanoparticles for solar driven interfacial evaporation, Sep. Purif. Technol., 292 (2022) 120985.

[16] W.M. Zhang, J. Yan, Q. Su, J. Han, J.F. Gao, Hydrophobic and porous carbon nanofiber membrane for high performance solar-driven interfacial evaporation with excellent salt resistance, J. Colloid Interface Sci., 612 (2022) 66.

[17] T.L. Dowd, L. Li, C.M. Gundberg, The H-1 NMR structure of bovine Pb^{2+}-osteocalcin and implications for lead toxicity, Biochim. Biophys. Acta, 1784 (2008) 1534.

[18] J.P. Nataro, J.B. Kaper, Diarrheagenic *Escherichia coli*, Clin. Microbiol. Rev., 11 (1998) 142.

[19] Guidelines for Drinking-water Quality, 4th edition, incorporating the 1st addendum, World Health Organization (available at: https://www.who.int/publications/i/item/9789241549950), in, 2011.

Conclusion and Perspectives

Conclusion

In this work, the evaporation of water on three different photothermal materials, namely green moss-poly(N-phenylglycine) (GM-PNPG), green moss-petroleum coke (GM-PetCoke) and cigarette filter-petroleum coke (Cigratte Filter-PetCoke) was examined.

In Chapters 3 and 4, materials from green moss were prepared. Compared to the raw green moss, which displayed a conversion efficiency of 64.2%, its hybridization with poly(N-phenylglycine) and petroleum coke resulted in improved evaporation (Conversion efficiency: 76.5% and 77.7%, respectively). This is a consequence of the excellent photothermal properties of PNPG and petroleum coke.

In Chapter 5, the preparation of a 3D evaporator consisting of cigarette filters combined with petroleum coke was discussed. This evaporator exhibited excellent performance (Conversion efficiency: 93.2%) due to a synergistic effect of the heat confinement in the 3D structure and the excellent photothermal property of petroleum coke. In addition, this device holds great promise for real operation, owing to its scalable geometry. This evaporator featured better performance than that reported in many published researches in 2022 (**Table 6.1**).

With regard to the quality of the water produced by these evaporators, all three evaporators were found to be capable of producing drinking water safe enough for the human body from seawater taken from the North Sea using a simple Plexiglas device. In addition, the device equipped with these evaporators was able to remove bacteria from the water by means of condensation.

In summary, in this work, photothermal materials for interfacial solar evaporators were prepared using very accessible and inexpensive raw materials through very simple and environmentally-friendly processes. PNPG and petroleum coke are very promising photothermal materials. These approaches are effective in improving evaporation of a naturally abundant green moss raw material.

Table 6.1. Comparison with other recent scientific publications

Material	Conversion Efficiency (%)	Evaporation rate (kg m^{-2} h^{-1})	Reference
Cigarette filter - petroleum coke (3D)	**93.2 ± 5.4**	**1.97 ± 0.07**	**Chapter 5**
Polyester-PPy-PFDTS	91.68	1.49	1 (2022)
Cellulose/carbon nanotube membrane	89	1.6	2 (2022)
Hydrophobic and porous carbon nanofibre	87.5	1.43	3 (2022)
Ni_3S_2@Ni, 3D	84.7	1.53	4 (2022)
Polypropylene / polyacrylonitrile nanofibres	83.5	1.633	5 (2022)
Corncob-Carbon black	-	1.425	6 (2022)
Carbonised walnut shells	81.4	1.22	7 (2022)
PDMS sponge / carbon nanoparticle	77.8	1.36	8 (2022)
Green moss - petroleum coke	**77.7 ± 1.2**	**1.34 ± 0.02**	**Chapter 4**
Green moss - PNPG	**76.5 ± 3.9**	**1.31 ± 0.05**	**Chapter 3**
Cigarette filter (3D)	73.3 ± 7.9	1.62 ± 0.07	Chapter 5
Green moss	64.2 ± 3.0	1.15 ± 0.02	Chapters 3, 4
Cigarette filter - petroleum coke (2D)	64.0 ± 3.1	1.14 ± 0.02	Chapter 5
Cigarette filter (2D)	41.9 ± 3.8	0.84 ± 0.07	Chapter 5

Perspectives

From my point of view, the current problems of solar interfacial evaporation concern mainly two points: (I) Lack of consistency in the evaluation method, and (II) absence of research on performance under more real conditions.

Regarding point (I), it seems to me that too much importance is given to the "crude" evaporation rate under 1 sun in this field. As mentioned several times in this work, evaporation changes enormously depending on the weather conditions, because the evaporation rate depends on the difference between the vapour pressure at the evaporator and that of the atmosphere. From this point of view, weather conditions cannot be neglected.

In reality, however, a considerable amount of research assumes a "fixed" value of evaporation under 0 sun by making either a single measurement or no measurement at all. For example, in Chapter 3, evaporation under 0 sun was reduced from 0.28 (kg m^{-2} h^{-1}) to 0.18 (kg m^{-2} h^{-1}) between 35% and 65% relative humidity. This shows that an error of 0.1-0.15 (kg m^{-2} h^{-1}) is possible for the same device and material in the case of a 2D structure. The worst case is that a fixed value of evaporation under 0 sun is likely to be used for the calculation of the conversion efficiency. If the 0 sun evaporation measurement has been carried out at a higher humidity than the other irradiation measurements, the evaporation will easily be overestimated.

Problem (II) is more complex than problem (I). Until now, much research has focused on the material only. But in order to apply this technology for real world use, evaporation must be examined under real conditions.

For vapour condensation, the evaporator is supposed to be placed in a closed chamber. As soon as irradiation starts, the relative humidity will increase from the initial value to saturation (100%). Before saturation, the contribution of evaporation under 0 sun is effective. But as time passes, this component becomes negligible. In other words, the 3D structure with normally better evaporation under 0 sun would be favourable for shortening the time to reach saturation, but it is the conversion efficiency that would be important after saturation. From this point of view, the 3D structure with good efficiency is more desirable.

An increase in temperature in the chamber undergoing irradiation could easily be anticipated. Moreover, this technology would be more in demand in low latitude areas. In this work, the temperature examined was always below 25 °C. However, the practical operating temperature

(in the chamber) will easily exceed 40 °C. It would therefore be very useful to examine operation at higher temperatures.

With the help of computer tools and modelling of the water flow and heat distribution/thermal conduction, new horizons would be opened for the optimisation of the device and the shape of the evaporator.

I would like to conclude by hoping that this research has provided other researchers with tips on the preparation of a solar evaporator and the appropriate evaluation method.

References

[1] C. Zhang, P. Xiao, F. Ni, J.C. Gu, J.H. Chen, Y.J. Nie, S.W. Kuo, T. Chen, Breathable and superhydrophobic photothermic fabric enables efficient interface energy management via confined heating strategy for sustainable seawater evaporation, Chemical Engineering Journal 428 (2022) 131142.

[2] Z.Y. Yang, L.L. Zang, T.W. Dou, Y.J. Xin, Y.H. Zhang, D.Y. Zhao, L.G. Sun, Asymmetric Cellulose/Carbon Nanotubes Membrane with Interconnected Pores Fabricated by Droplet Method for Solar-Driven Interfacial Evaporation and Desalination, Membranes 12 (2022) 369.

[3] W.M. Zhang, J. Yan, Q. Su, J. Han, J.F. Gao, Hydrophobic and porous carbon nanofiber membrane for high performance solar-driven interfacial evaporation with excellent salt resistance, Journal of Colloid and Interface Science 612 (2022) 66.

[4] Z.P. Yao, K.L. Yu, M.Y. Pan, H.B. Xu, T.Q. Zhao, Z.H. Jiang, A mechanically durable, excellent recyclable 3D hierarchical Ni_3S_2@Ni foam photothermal membrane, Green Energy & Environment 7 (2022) 492.

[5] X.H. Ren, S.S. Cui, J. Guan, H.F. Jin, H.D. Yuan, S.X. An, PAN@PPy nanofibrous membrane with core-sheath structure for solar water evaporation, Materials Letters 313 (2022) 131807.

[6] H.L. Duan, T. Ling, Y.J. Yan, Y.D. Wang, Corncob-based evaporator for high-efficiency solar vapor generation, Journal of Photonics for Energy 12 (2022) 018001.

[7] Y.Z. Wang, X.Y. Luo, X.Y. Song, W. Guo, K. Yu, C.Y. Yang, F.Y. Qu, Turning waste into treasure: Carbonized walnut shell for solar-driven water evaporation, Materials Letters 307 (2022) 131057.

[8] X.S. Li, S.Y. Tanyan, S.J. Xie, R. Chen, Q. Liao, X. Zhu, X.F. He, A 3D porous PDMS sponge embedded with carbon nanoparticles for solar driven interfacial evaporation, Separation and Purification Technology 292 (2022) 120985.

Annexes

Annex 1. Evaporation rates and conversion efficiencies of GM-PNPG and GM-PetCoke (Pure Water) under different conditions.

GM-PNPG	Temperature (°C)	Humidity (%)	Evaporation 0 sun ($kg\ m^{-2}\ h^{-1}$)	Temperature of the interface (°C)	Evaporation 1 sun ($kg\ m^{-2}\ h^{-1}$)	Conversion Efficiency (%)
1	20.0	59	0.210	33.2	1.24	70.7
2	21.2	55	0.204	32.9	1.32	76.6
3	24.0	69	0.168	34.5	1.37	82.1
1-3	**	**	**	**	1.31 ± 0.05	76.5 ± 3.9
GM-PetCoke	Temperature (°C)	Humidity (%)	Evaporation 0 sun ($kg\ m^{-2}\ h^{-1}$)	Temperature of the interface (°C)	Evaporation 1 sun ($kg\ m^{-2}\ h^{-1}$)	Conversion Efficiency (%)
1	22.8	59	0.204	33.9	1.36	79.4
2	21.7	53	0.228	33.0	1.33	75.9
3	22.0	61	0.186	32.6	1.32	77.8
1-3	**	**	**	**	1.34 ± 0.02	77.7 ± 1.2
GM	Temperature (°C)	Humidity (%)	Evaporation 0 sun ($kg\ m^{-2}\ h^{-1}$)	Temperature of the interface (°C)	Evaporation 1 sun ($kg\ m^{-2}\ h^{-1}$)	Conversion Efficiency (%)
1	21.5	54	0.228	30.4	1.14	62.5
2	21.2	41	0.252	29.8	1.15	61.3
3	22.0	60	0.186	31.5	1.19	68.7
1-3	**	**	**	**	1.15 ± 0.02	64.2 ± 3.0

Annex 2. Peak positions and assignments of the XPS spectra of each element (PetCoke)

Element	Peak 1	Peak 2	Peak 3	Peak 4	Peak 5	Peak 6
C 1s (90.0 % atomique)	C–C/C=C (64.7 %) (284.7 eV)	C–N/C–S (28.1 %) (285.3 eV)	C–O (7.2 %) (286.1 eV)			
O 1s (4.9 %)	C=O (86.1 %) (532.1 eV)	C–O (13.9 %) (534.1 eV)				
N 1s (0.9 %)	Pyridinique (24.8 %) (398.5 eV)	Graphitique (75.2 %) (400.3 eV)				
S 2p (2.6 %)	S–Pb $2p_{3/2}$ (17.0 %) (160.2 eV)	S–Pb $2p_{1/2}$ (10.1 %) (162.5 eV)	S–C $2p_{3/2}$ (22.8 %) (164.0 eV)	S–C $2p_{1/2}$ (8.3 %) (165.2 eV)	SO_3^{2-} $2p_{3/2}$ (24.4 %) (166.2 eV)	SO_3^{2-} $2p_{1/2}$ (17.4 %) (168.4 eV)
Pb 4f (1.6 %)	Pb (0) $4f_{7/2}$ (8.7 %) (137.6 eV)	Pb (II) $4f_{7/2}$ (47.9 %) (138.9 eV)	Pb (0) $4f_{5/2}$ (5.1 %) (142.4 eV)	Pb (II) $4f_{5/2}$ (38.3 %) (143.7 eV)		

Annex 3. Evaporation rates and conversion efficiencies of Filter-PetCoke and Filter (Pure Water) under different conditions.

Filtre-PetCoke (3D)	Temperature (°C)	Humidity (%)	Evaporation 0 sun ($kg\ m^{-2}\ h^{-1}$)	Temperature of the interface (°C)	Evaporation 1 sun ($kg\ m^{-2}\ h^{-1}$)	Conversion Efficiency (%)
1	21.0	46	0.74	25.5	2.11	93.3
2	21.1	52	0.64	27.4	1.97	90.6
3	21.4	54	0.64	27.5	1.89	84.9
4	22.0	71	0.38	29.1	1.90	103.8
1-4	**	**	**	**	1.97 ± 0.07	93.2 ± 5.4
Filtre-PetCoke (2D)	Temperature (°C)	Humidity (%)	Evaporation 0 sun ($kg\ m^{-2}\ h^{-1}$)	Temperature of the interface (°C)	Evaporation 1 sun ($kg\ m^{-2}\ h^{-1}$)	Conversion Efficiency (%)
1	20.9	68	0.17	33.2	1.15	67.6
2	21.9	63	0.19	32.2	1.16	66.7
3	21.7	51	0.25	31.7	1.10	58.9
4	22.0	58	0.23	32.3	1.15	63.0
1-4	**	**	**	**	1.14 ± 0.02	64.0 ± 3.1
Filtre (3D)	Temperature (°C)	Humidity (%)	Evaporation 0 sun ($kg\ m^{-2}\ h^{-1}$)	Temperature of the interface (°C)	Evaporation 1 sun ($kg\ m^{-2}\ h^{-1}$)	Conversion Efficiency (%)
1	21.8	49	0.79	22.4	1.64	57.5
2	22.0	66	0.48	24.5	1.58	74.7
3	22.0	68	0.48	23.9	1.72	84.6
4	22.1	75	0.40	24.8	1.52	76.4
1-4	**	**	**	**	1.62 ± 0.07	73.3 ± 7.9
Filtre (2D)	Temperature (°C)	Humidity (%)	Evaporation 0 sun ($kg\ m^{-2}\ h^{-1}$)	Temperature of the interface (°C)	Evaporation 1 sun ($kg\ m^{-2}\ h^{-1}$)	Conversion Efficiency (%)
1	21.7	55	0.26	27.8	0.95	47.2

2	22.0	59	0.21	28.5	0.86	44.3
3	21.9	55	0.22	28.1	0.77	38.1
4	21.9	55	0.21	27.8	0.77	38.1
1-4	**	**	**	**	0.84 ± 0.07	41.9 ± 3.8

Annex 4. Variation of the mass of the whole device under an irradiation of 1 sun and 0 sun

Filter-PetCoke (3D)	1 sun (120-180 min) (mg / 10 min)	0 sun (300-360 min) (mg / 10 min)	1 sun – 0 sun (mg / 10 min)
1	-233.1	-140.4	-92.7
2	-212.7	-122.1	-90.6
3	-205.0	-121.3	-83.7
4	-174.3	-71.5	-102.8
1-4	**	**	-92.5 ± 5.3
Filter-PetCoke (2D)	1 sun (120-180 min) (mg/10 min)	0 sun (300-360 min) (mg/10 min)	1 sun – 0 sun (mg / 10 min)
1	-99.2	-32.4	-66.8
2	-103.0	-36.3	-66.7
3	-104.3	-46.7	-57.6
4	-106.7	-43.2	-63.5
1-4	**	**	-63.7 ± 3.1
Filter (3D)	1 sun (120-180 min) (mg / 10 min)	0 sun (300-360 min) (mg / 10 min)	1 sun – 0 sun (mg / 10 min)
1	-207.7	-149.7	-58.0
2	-165.3	-90.8	-74.5
3	-175.7	-91.3	-84.4
4	-152.0	-75.3	-76.7
1-4	**	**	-73.4 ± 7.7
Filter (2D)	1 sun (120-180 min) (mg/10 min)	0 sun (300-360 min) (mg/10 min)	1 sun – 0 sun (mg / 10 min)
1	-95.8	-48.3	-47.5
2	-84.0	-40.3	-43.7
3	-79.0	-41.3	-37.7
4	-77.7	-39.8	-37.9
1-4	**	**	-41.7 ± 3.9